Statistical Correlation and Modelling of Carbonate Heterogeneity

David P. Price

Thesis Submitted for the Degree of

Doctor of Philosophy

The University of Edinburgh

Declaration

I declare that this thesis has been composed by myself and has not been submitted for any other degree or qualification. The work presented is entirely my own, except where otherwise acknowledged.

David P. Price

Abstract

In many carbonate reservoirs, much of the porosity is in the form of micropores (with diameter 1-10μm). This porosity lies far below the resolution of any conventional wireline logging tools and can only be observed through the analysis of extracted core. To investigate the spatial distribution of the microporosity over a large range of length scales requires accurate depth matching of extracted core to wireline data. With such a correlation up- and down-scaling relationships can be developed between porosity relationships observed at different length scales. The scaling relationships can then be used to infer the distribution of microporosity in regions of the borehole without extracted core.

This thesis presents a new, general method for the accurate correlation of extracted core to wireline logs using their statistical properties. The method was developed using an X-ray computed tomography (CT) scan of a section of extracted carbonate core and well log data from the so-called Fullbore MicroImager (FMI) resistivity tool. Using geological marker features the extracted core was constrained to correspond to a 2ft (609mm) section of FMI data. Using a combination of statistics (mean, variance and the range from variograms of porosity), combined in a likelihood function, the correlation was reduced to an uncertainty of 0.72" (18.29mm). When applied to a second section of core, the technique reduced the uncertainty from 2ft (609mm) down to 0.3ft (91mm).

With accurate correlation between core and wireline logs, the scaling relationships required to transfer porosity information between scales could be investigated. Using variogram scaling relationships, developed for the mining industry, variograms from the CT scan were up-scaled and compared with those calculated from associated FMI data.

To simulate core samples in regions of the borehole without extracted core, two statistical simulation techniques were developed. The techniques both capture two-point spatial statistics from binarised, horizontal slices of FMI data. These statistics

are combined to obtain multi-point statistics, using either neighbourhood averaging or least squares estimation weighted by variance. The multi-point statistics were then used to simulate 2-D slices of 'virtual' core. Comparisons between the two techniques, using a variety of features, revealed that the neighbourhood averaging produced the most reliable results.

This thesis thus enables, for the first time, core-to-log depth matching to the resolution of the logging tools employed. Spatial statistics extracted from the core and up-scaled can then be compared with similar statistics from the precisely-located log data sampling the volume of rock around the borehole wall. Finally simulations of 'virtual' core can be created using the statistical properties of the logs in regions where no core is available.

Acknowledgements

I would like to thank my supervisors Andrew Curtis and Rachel Wood for their help in guiding me through the PhD process.

I would also like to thank Jenny, and my family, for being there to provide support and words of encouragement throughout the project.

The project was supported by Schlumberger Cambridge Research (SCR), Schlumberger Doll Research (SDR) and the National Environmental Research Council (NERC).

Contents

Chapter 1 - Introduction

1.1 Introduction

Carbonates rocks form some of the most important sedimentary formations on Earth, comprising 19-22% of the global record. They are composed mainly of $CaCO_3$ or $CaMg(CO_3)_2$ derived from either, biological and skeletal material, or by direct precipitation from water. Carbonate formations are found throughout the world and are known from 3.6Gyr to the present day. They are economically important as they are estimated to contain 50% of the world oil reserves (Ramakrishnan et al., 1998). They also contain significant ground water aquifers (Maupin and Barber, 2005) and host substantial metal sulphide ore deposits (Evans, 1993). The rocks themselves are also used to produce construction materials, such as cement and concrete, and are a key ingredient in the chemical industry.

For all the importance of carbonate rocks they remain, however, poorly understood, particularly in terms of their fluid flow properties compared to siliciclastic rocks. Siliciclastic rocks, such as sandstone and silts, tend to be composed of regular, near spherical grains and almost all of their porosity is found between these grains. This allows the creation of relationships between porosity, permeability and the grain distribution within the rock. However in carbonate rocks the grains are often irregular in shape and are themselves porous. Therefore there is no simple relationship between grain size and porosity (Choquette and Pray, 1970).

The different distribution of porosity in carbonate rocks can be attributed to the complex nature of the processes that control both their formation and subsequent diagenesis. Most carbonates are formed in a marine environment and therefore production is sensitive to changes in water chemistry, the biology of the system, and temperature. The percentage of CO_2, and the Ca/Mg ratio of sea water, is thought to determine the type of limestone formed: high-Mg calcite, low-Mg calcite or aragonite. High-Mg calcite and aragonite are both metastable and will be converted into low-Mg calcite over time. This conversion can lead to the creation of pore space

within the grains as the minerals recrystallise. Fluids flowing through the rocks during burial can also dissolve carbonate which can either create voids or precipitate carbonate cements infilling pores. The result of these processes is that the original depositional structure of the rock can be heavily overprinted (Wright and Tucker, 1991). The resulting carbonate rock contains a highly complex, heterogeneous pore network, which ranges from micron sized pores between crystals up to metre-wide cave systems.

1.2 Previous Work

Carbonates have been traditionally described using classification systems based on depositional textures, using either the major constituents of the rock (Folk, 1959) or a combination of components and the amount of mud/cement within the rock (Dunham, 1962). However, when looking for trapped fluids, particularly hydrocarbons, the porosity and permeability of the rocks are the most important features. This lead to a number of classification schemes based on the types of pores observed (Choquette and Pray, 1970; Lonoy, 2006). Then (Lucia, 1983, 1995, 1999), developed a modified Dunham classification system which linked observed rock textures to peterophysical (porosity and permeability) estimates. Though pore size is a major control on porosity/permeability relationships (Lucia, 1983), Lucia's classification scheme is based on the size of particles within the rock. This lead (Lonoy, 2006), to create a new classification scheme based on pore type following Choquette and Pray (1970), but including a development of Lucia's textural analysis to include permeability estimates.

The traditional classification schemes work on two dimensional images, but to understand how fluids flow within a complex formation, such as a carbonate, requires full 3-D information of the pore network. 3D images of the pore network can be obtained using X-ray Computed Tomography (CT) (Duliu, 1999; Mees et al., 2003). The availability of 3-D images has allowed real 3-D pore networks to be extracted and used to calculate petrophysical properties which agree well with those obtained by laboratory measurements (Lindquist et al., 2000; Arns et al., 2001; Arns et al., 2002; Arns et al., 2003; Knackstedt et al., 2004). The size of pore which can

be imaged using a CT scan is proportional to the sample size, with a 1μm diameter pore requiring a sample no larger than $1mm^3$. Using a range of different sized core samples, a library of images can be constructed each with a known porosity distribution (Arns et al., 2005a). However as with all the classification schemes discussed, the use of the CT technique can only be used to describe physical rock samples.

1.3 Heterogeneity

The term heterogeneity is used to describe the quality of being made of many different elements, forms, kinds or individuals. This is true of carbonates which are composed of biological remains (e.g. shell fragments), mud, cement and reworked rock fragments. These constituents have irregular shapes and sizes, which leads to the pore space between them being highly irregular and multiscaled. Pores found between crystals (intercrystal porosity) can often be very small, less than 1μm in diameter, but yet form the bulk of a rocks storage capacity (Budd, 1989; Moshier, 1989). The pore space can also be found within individual particles, in the moulds of dissolved particles and in the form of shelter porosity, where a particle such as a shell has protected a void from being filled during burial (Choquette and Pray, 1970). These different types of pore space combine to create a highly heterogeneous pore network. An example of a section of carbonate, with different rock elements highlighted, is shown in Figure 1.1.

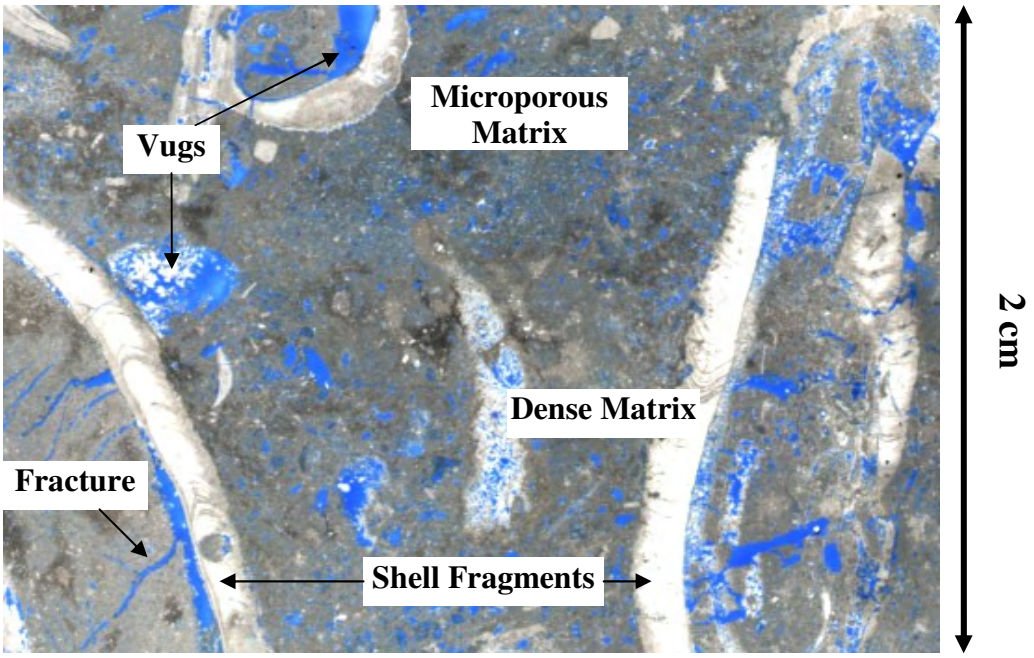

Figure 1.1. Thin section of carbonate, with different rock elements and pore types highlighted. Pores are coloured blue due to the injection of resin into the sample.

Figure 1.1 shows a 2-D thin section containing some of the different rock elements that make up carbonates, each of which have different degrees of porosity. There are two different regions of matrix observed. One is densely packed, but may contain porosity below the resolution of the image (Dense Matrix). The other is more open with clearly distinguishable pores (Microporous Matrix). Other components are calcitic shell fragments which have very little porosity and vugs which are large pores. This heterogeneity of rock elements is observed at all measurement scales making clear why it is difficult to predict how fluids will flow through carbonate formations.

2-D thin sections can be used in pore characterisation studies (Anselmetti et al., 1998). However, 2-D data cannot provide information about how pores change shape, or how different regions of the rock are connected out with the plane of the thin section. Such information is vital if we are to understand fluid flow and requires 3-D images.

1.4 Motivation

When studying formations at depth the amount of physical core samples available is severely limited due to the great expense of their collection. Instead, the bulk of the available information comes from comparatively inexpensive geophysical borehole measurements. These geophysical instruments do not measure porosity directly, but rather measures another physical property (e.g. nuclear magnetic resonance (NMR), resistivity, etc,) which can be converted to, or used as a proxy for, porosity and permeability (Rider, 2002; Russel et al., 2002). While geophysical data provides comprehensive coverage it is often at low resolution (in that it samples a relatively large volume) and is therefore unable to image individual pores.

If the high resolution core samples and low resolution geophysical measurements are available from the same region of a borehole then statistical up- and down-scaling relationships can be developed to predict the detailed statistics of the porosity distribution. These relationships can then be applied to regions of the borehole that have geophysical data but lack core samples (Delhomme et al., 1996; Tilke et al., 2006).

However even the highest resolution borehole data (e.g. Fullbore MicroImager, Photographic logs) is only two dimensional, as this method takes measurements from the borehole wall. To understand the distribution of porosity and permeability within a heterogeneous formation requires three dimensional information of the formation, such as that provided by X-ray CT scans.

1.5 Modelling

The creation of models of porous media has been carried out using templates to capture the spatial statistics from a training image, which can then be used to create models of soils (Li et al., 2004), or rock samples (Okabe and Blunt, 2004; Wu et al., 2004). These simulations utilise the concept of a Markov Chain process. A Markov Chain process is a discrete stochastic process in which the future behaviour of a system is dependent solely on the current state of the system; it has no dependence on its previous states (Fisz, 1963). In a simulation the assumption of a Markov

Chain means that only small scale transitions are required to simulate large scale features (Philippe et al., 1992).

Existing modelling work has used training images arranged orthogonally to gather spatial statistics. However in a borehole the data is gathered from a highly curved wall. Therefore a new method is required to capture the relevant spatial statistics and then produce realisations which honour those statistics.

1.6 Aims

To greatly improve our understanding of the complex heterogeneous pore networks within carbonate rocks requires an integrated approach (Figure 1.2). The different sources of porosity data, measured over a large range of length scales, have to be accurately correlated. This allows the development of up- and down-scaling relationships between the different data types. The development of an efficient modelling algorithm would allow realisations of any missing material to be created. It would also allow a range of realisations to be created with the same spatial statistics. These realisations could be populated using the up- and down-scaling porosity relationships. The resulting 3D porosity information, over a range of scales, could be used to provide valuable fluid flow information using fluid flow simulations (Chen et al., 1992; Blunt et al., 2002).

Therefore the aims of this thesis are:

1. Develop a method for the accurate correlation between core and log data.
2. Use variogram scaling laws to relate variograms calculated from core data to those from borehole log data.
3. Develop a method for simulating a 3-D volume from 2-D log measurements.
4. Integrate aims 2 and 3 to create simulations of 3-D rock at small (core) scale from data at log scale.

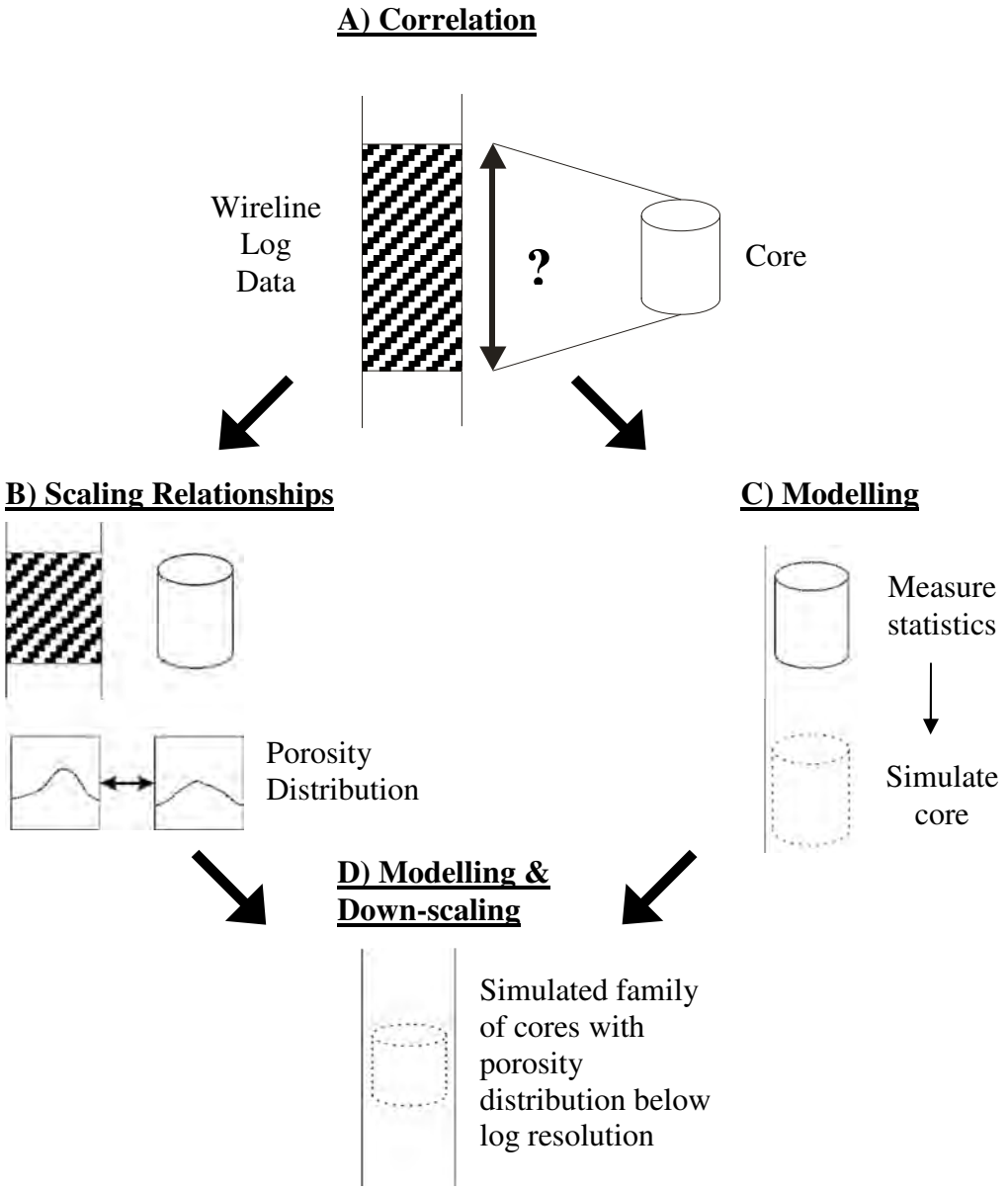

Figure 1.2. Outline of the proposed methodology for the integration of porosity information across a range of scales, from individual pores observed in core samples up to wireline log measurements. A) Core and wireline data sets require to be accurately correlated. Correlation then allows B) the development of porosity scaling relationships and C) the development of modelling techniques. These can then be combined to D) simulate core sections and populate them with down-scaled porosity information.

1.7 Data

The carbonate data used throughout this thesis came from the Middle Eastern, Lower Cretaceous Shu' aiba Formation, within the Thamama 'Group' (Figure 1.3). The

carbonate formations of the Middle East are of particular importance as they contain a substantial proportion of the Earth's remaining hydrocarbon reserves. The Shu' aiba Formation contains many of the regions most prolific hydrocarbon reservoirs (Buchem et al., 2002). The Shu' aiba was laid down on a stable platform at the edge of the Tethys ocean (Konert et al., 2001). It shallows-upwards from packstones and wackestones into inter-mixed rudist grainstones and algal boundstones (Alsharhan, 1987; Pittet et al., 2002). During diagenesis much of the mud within the Formation has been recrystallised as microrhombic calcite crystals (1-10μm). A considerable proportion of the Shu' aiba's porosity lies between these crystals with typical pore diameters of less than 2μm (Budd, 1989; Moshier, 1989).

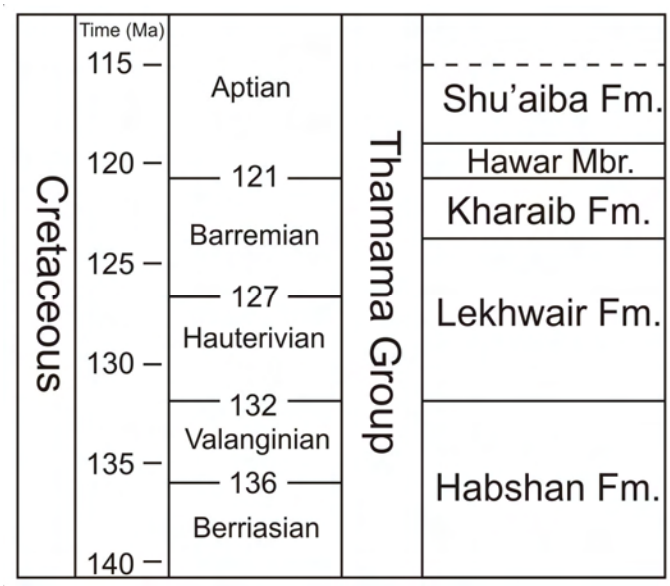

Figure 1.3. Cretaceous stratigraphy in the Thamama 'Group' in the Arabian Gulf region.

1.8 Thesis Outline

The next chapter I will present a review of the existing literature. Firstly, I look at the processes which lead to the creation of the heterogeneous structures within carbonate formations. Then I look at the range of methods available for capturing information about carbonate formations at a range of different scales. Finally, I discuss the available methods for integrating data from different scales, before highlighting some of the problems still to be tackled.

In chapter 3 I have described the source of the data which was provided to the project. I have also described the processing which was applied to the data sets prior to it being provided.

In this thesis I have focused on the key aspects of the methodology set out in Figure 1.2. Firstly, the problem of accurate correlation between different data types is investigated. A method was developed using the example of correlating extracted core to resistivity measurements of the borehole wall. Both of these data sets were converted to porosity estimates. Given the lack of distinctive geological features within the formation which would enable a direct correlation to be made between the two data types I have developed a statistical approach (Chapter 4). Once scaled to the same resolution, a cascade of statistics, calculated individually for each data set, was then compared using a utility function. The resulting correlation greatly improved on the initial correlation estimates down from 2ft to 0.06ft.

The correlation method was validated by applying it to a second section of core and corresponding resistivity data (Chapter 5). Again the lack of large scale features prevented direct correlation between the two data sets. Using the statistical correlation method the correlation region was narrowed from 2ft down to two separate regions, both in the order of 0.2ft.

With the development of a technique for the accurate correlation of core and wireline data sets, I then went on to investigate scaling relationships between the two data sets (Chapter 6). Using the variogram scaling laws set out by Matheron (1963), variograms calculated from the original CT data were compared with those calculated from averaged CT data. The poor results, however, suggest that the use of a single variogram model is not suitable for capturing the spatial variability within the CT data.

The creation of models from borehole data was next examined (Chapter 7). Taking the pattern of measurements obtained by the high resolution borehole resistivity tool,

the Fullbore MicroImager (FMI), I have developed a 2D modelling code. Using a variety of synthetic formations allowed the null space of the technique to be explored. While the FMI arrangement of measurements is shown to capture sufficient spatial information from an image, a simple two point template is insufficient to honour that information in a reconstruction. This suggests that modelling is possible but by utilising a larger template and larger section of data.

Chapter 2 - Literature Review

2.1. Introduction

Compared to reservoirs found in siliciclastic formations those found in carbonate formations are highly heterogeneous. The physicochemical processes that control their formation combined with their biological origins create formations which vary greatly over a range of length scales. The heterogeneous nature of the formations structure leads to a complex distribution of porosity in the formation. Therefore in order to understand and exploit reservoirs within carbonate formations requires the integration of information from a range of techniques which focus on different length scales.

2.2 Why makes carbonate reservoirs different?

2.2.1 Siliciclastic Reservoirs

Much of the work carried out on understanding reservoir heterogeneity, in terms of predicting porosity and permeability distributions, has focused on siliciclastic formations as these are relatively simple to understand. Silci-clastic formations are formed by the transport and deposition of eroded pre-existing detritus. This sediment is carried from its origin in high energy systems such as rivers and is then deposited when as the energy of the system decreases such as when the river enters the sea. The main controls on siliciclastic deposition are climate, tectonics and sea level change, which combine to determine the accommodation space available to be filled (Posamentier and Allen, 1999). Packages of siliciclastic beds, with unique structures, are laid down during different phases of relative sea level change can be identified and described using a sequence stratigraphic framework (Emery, 1996b). The petrophysical properties of individual beds are controlled by the energy of the depositional system which sorts the grain sizes deposited (Leeder, 1999). After burial the dominant processes are compaction and cementation as the majority of the material is silica based and unreactive, limiting chemical diagenesis (Worden and Burley, 2003).

The resulting siliciclastic formations preserve many of their depositional structures. Therefore to modern day siliciclastic depositional settings can be used as analogues to understand their structure or as they are controlled by a limited number of physical processes computer models can be used to create simulations (Tetzlaff and Harbaugh, 1989).

2.2.2 Carbonate Reservoirs

Carbonate formations are fundamentally different from siliciclastic formations as the bulk of carbonate sediment is formed in situ. Instead of material being transported carbonate sediment is instead precipitated from sea water by organisms. The biological origins of carbonate sediment mean that there are a wide range of factors which influence both types of sediment grains produced and the locations, i.e. ecological demands, in which it is deposited. Carbonate formations are also highly susceptible to digenesis after burial, which can result in over printing of the original depositional structures. These processes combine to create carbonate deposits which vary widely both in space and time.

2.2.2.1 Controls

The biological origin of carbonate sediment means that its production is influenced by a wide range of parameters. Water depth is a key parameter as it governs the amount of light available for photosynthesis and it is also a factor in determining the kinetic energy of the water through the position of the mean wave base. Photosynthesis is the process by which organisms convert light energy to chemical energy for their growth. Without enough sunlight the organisms cannot grow and precipitate carbonate (Bathurst, 1975). The energy of the water, which is also governed by currents, affects the production of carbonate sediment differently from in a siliciclastic formation as high energy areas tend to correspond to increased productivity compared to lower energy areas (Wilson, 1975). Temperature is another factor as carbonate producing organisms will only survive within a relatively warm temperature range (Glynn and d'Croz, 1989). Salinity variations due to circulation patterns or freshwater influx will also create variations in the distribution of

organisms (Squires, 1962; Kinsman, 1964). Even the type of carbonate precipitated, aragonite, high-Mg or low-Mg calcite, varies according to changes in sea water chemistry. This affect is particularly noticeable when investigating carbonates from different periods in geological past (Sandberg, 1975, 1983; Stanley and Hardie, 1998). Other factors include the underlying topography which can dictate both water depth and energy (through its position relative to prevailing winds), evolutionary change which alters the organisms present, and the level of terrigenous sediment input which can smoother carbonate producing organisms (Wilson, 1975). The effect of these controls concentrates the production of carbonate into shallow, warm marine waters known as the 'carbonate factory' (Figure 2.1.) (James, 1984).

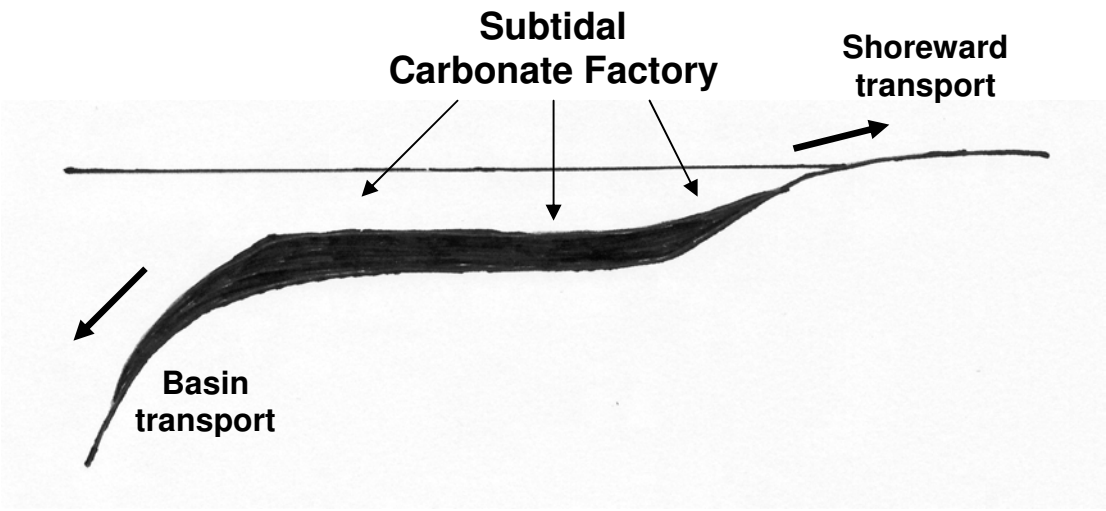

Figure 2.1. An illustration of the main carbonate producing area known as the 'Carbonate Factory'. The region lies in shallow (<15m), warm marine water. Carbonate material is transported from this region shoreward or out into the basin. After James, (1984).

2.2.2.2 Structure

The controls on carbonate production interact to create an abundance of different environmental niches each with its own biological assemblages. These different assemblages then create different lithofacies after burial (Wilson, 1974, 1975; Scoffin, 1987). The range of different assemblages has been divided into a number of generalised areas as shown in Figure 2.2.

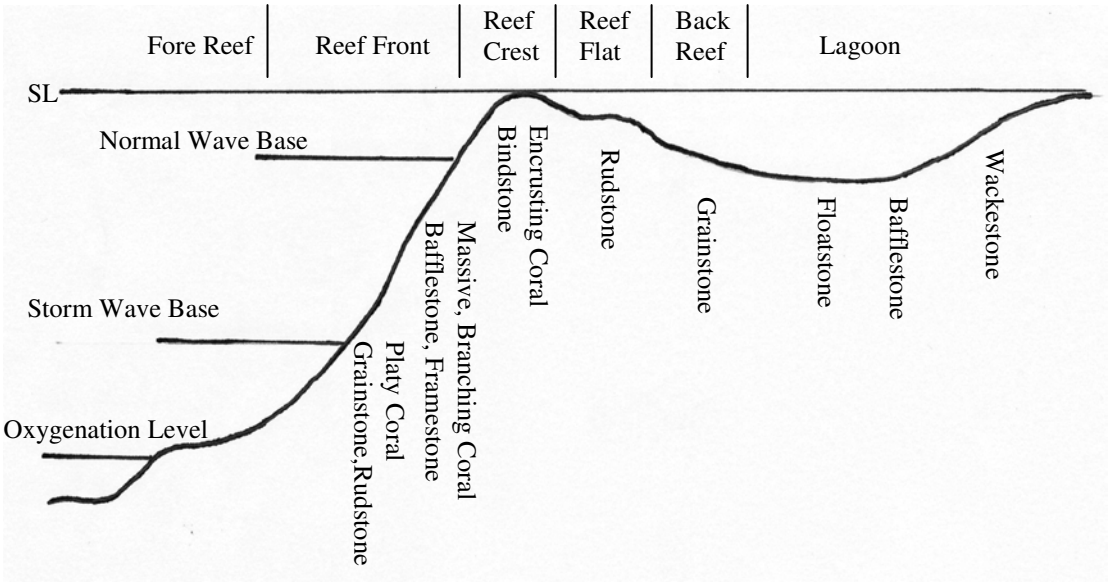

Figure 2.2. An idealised cross-section of carbonate reef facies, showing environment and facies type. After Wilson (1974) and Scoffin (1987)

In the deepest areas of the basin there is not enough light to allow in situ carbonate production. Instead carbonate sediment is built up from the decaying remains of pelagic plankton which grows near the sea surface and then sinks after death forming layers of fine mudstones. As the water depth decreases on the tidal shelf, more light can reach the sea floor and so allows the growth of in situ carbonate forming fossiliferous mudstones.

Towards the edge of the basin the depth decreases rapidly in the area known as the reef slope. In this region there is increased carbonate production with the appearance of platy corals but there is also debris flows from further up the slope. This leads to a range of deposits from reef boundstones to breccias of reworked material. At the top of the slope on the reef crest, there is the peak in carbonate production due to the shallow depth and high water energy. This leads to massive branching corals which trap carbonate mud forming bafflestones and framestones.

The reef crest stops sediment produced in the lagoon from flowing down the slope. This leads to a build up of carbonate material behind the reef creating rudtones and

grainstones. Behind the reef the energy of the water decreases in the lagoon but is still shallow enough to encourage carbonate production. In areas with good water circulation, described as 'open', this leads to an abundance of fauna and creating a range of facies from grainstones to mudstones. Patch reefs can also be found within the open lagoon areas. In areas of restricted water circulation there is less fauna and the area tends to produce mudstones from material transported into the area. At the very edge of the basin the sea floor can periodically become exposed creating an extreme environment in which little fauna can survive. Again this leads to the creation of very fine grain mudstones from sediment brought into the area but the periodic exposure of the sea floor also leads to the creation of evaporite deposits (e.g. anhydrite,gypsum etc.).

The different facies described above are for an idealised carbonate margin. In real examples not all of the facies will be present and those which are may not be laterally continuous due local effects (Wilson, 1975). The effects described so far outline how the general depositional structure of a carbonate reef is heterogeneous. Over time the large scale controls of tectonics and sea level alter the regions in which carbonate is produced creating large scale heterogeneity.

2.2.2.3 Sequence Stratigraphy

Sequence stratigraphy is the division of a sedimentary sequence into packages, each of which is composed of a series of sedimentary beds, deposited during a specific phase of sea-level change (Emery, 1996b; Posamentier and Allen, 1999). The changes in sea level are either eustatic changes in global sea level or a tectonic change in the basement which moves the depositional setting relative to sea level. There are three main phases which each have there own unique features and are shown in Figure 2.3.

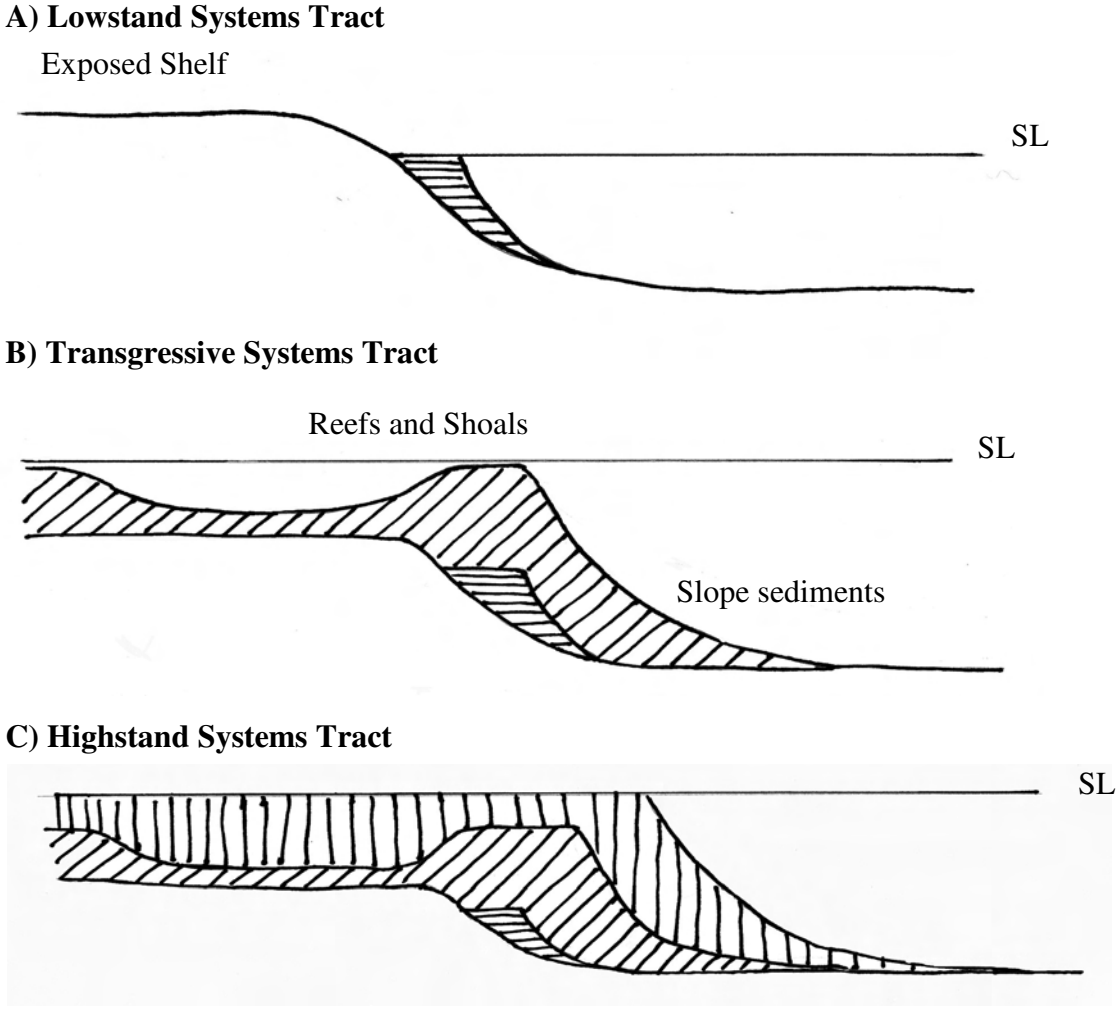

Figure 2.3. Examples of the 3 main systems tracts for carbonate sequence stratigraphy. A) Lowstand Systems Tract (LST). During this phase sea level has dropped exposing the shelf and carbonate production is limited to a small fringing reef. B) Transgressive Systems Tract (TST). During this phase sea levels are rising creating accomodation space for carbonate production to fill. C) Highstand Sytems Tract (HST). During this phase sea-level rise has reached a maximum and the carbonate production fills in the remaining accomodation space. When the shelf accomodation space is filled production slows and progrades into the basin.

During times of relatively low sea level, or a lowstand systems tract (LST) (Figure 2.3a), the shelf can become exposed. This then limits the available shallow water either completely shutting down the carbonate factory or restricting it to a small fringing reef. This therefore limits the amount of carbonate material produced. As

relative sea level rises, known as a transgressive systems tract (TST) (Figure 2.3b), the shelf is covered creating a large shallow area. During this period the carbonate factory works most efficiently and large amounts of carbonate can be built up. The rising sea level creates accommodation space above the shelf into which the carbonate can grow. The rate of sea level change is an important factor as if it rises faster than the carbonate precipitating organisms can grow then the system will be drowned and production will cease. When sea-level stops rising, known as a highstand systems tract (HST) (Figure 2.3c), new accommodation space is no longer created above the shelf. The carbonate factory will keep working until the accommodation space is filled but then it is restricted to a fringing reef which progrades the formation laterally (Tucker and Wright, 1990; James and Kendall, 1992; Emery, 1996a).

The three packages outlined above are the extreme end members of the sea level change scale. In reality there will be small scale changes in relative sea level which will be superimposed on the large scale changes creating a range of intermediate tracts. The resulting formation is composed of vertical cycles of carbonate facies, from metres to 100's of metres in length, which record deposition in progressively shallower environments (Wilson, 1975; Kendall and Schlager, 1981; Algeo and Wilkinson, 1988).

2.2.2.4 Diagenesis

Diagenesis is the term used to describe all the processes which affect sediments after burial but before the onset of metamorphism. These processes alter the original depositional fabrics of the sediments and in turn their petrophysical properties. Carbonate sediments are particularly susceptible to diagenetic change due to their chemical composition. Initially carbonate sediment consists of a mixture of aragonite, high-Mg calcite and low-Mg calcite mixture of aragonite, high-Mg calcite and low-Mg calcite. Both aragonite and high-Mg calcite are metastable and will eventually convert to the more stable form of low-Mg calcite. The principle diagenetic processes are cementation, compaction and dissolution and these processes are controlled by the sediment composition, the pore fluid chemistry and

flow rates and the burial history of the formation. . There are many detailed reviews on diagenetic processes (Bathurst, 1975; Longman, 1980; James and Choquette, 1983, 1984; Schneidermann and Harris, 1985) and so I will concentrate on the petrophysical effects of diagenesis.

The process of cementation precipitates carbonate cements from pore fluids onto the walls of the pore space. Over time these cements reduce the volume of pore space and restrict the permeability of the formation. Cementation starts soon after burial due to the high fluxes of sea water through the shallow sediment (Shinn, 1969). These early cements can therefore be linked to specific depositional textures with high permeability. However, later stage cements are formed from carbonate rich fluids flowing through the deposit or from the enrichment of fluids already present through dissolution elsewhere in the formation. These processes cannot be linked to specific depositional textures (Lucia, 1999).

Compaction, physical and chemical, also reduces the volume of pore space and restricts permeability and is caused by increases in pressure as the sediment is buried. In the early stages of burial physical compaction is dominant and can dramatically reduce the porosity of soft carbonate mud from 70% down to 40% (Shinn and Robbin, 1983; Goldhammer, 1997). As the burial depth increases then chemical compaction, or pressure dissolution, becomes more common. Chemical dissolution is influence by a range of factors including temperature, fluid composition and mineral composition. Chemical compaction features include stylolites, thin horizons containing insoluble material, and the interpenetration of grains. These features are not specific to depositional fabrics (Scholle and Halley, 1985; Choquette and James, 1986).

The other main diagenetic process is the dissolution of carbonate. As outlined above this can be caused by compaction during burial, but it can also be caused by changes in the pore fluids particularly if the sediment is uplifted into a region where the pore fluid is of meteoric origin opposed to marine. This results in the decomposition of carbonate minerals, particularly the metastable aragonite and high-Mg calcite (James

and Choquette, 1984). Another cause of dissolution is the flow of water through the formation. This will have a different chemical composition and possibly and different pH increasing the likelihood of dissolution. This process can lead to particularly large scale features such as cave systems (Longman, 1980; Tucker and Wright, 1990).

Other diagenetic processes include neomorphism, micritization and dolomitization (Tucker and Wright, 1990). All these diagenetic processes rework and overprint the original diagenetic textures. In the early stages of burial some aspects of compaction and cementation can be linked to specific depositional features. However, during deep burial the diagenetic processes become less fabric specific. The processes can also overlap with a section of the rock formation being subjected to a number of different diagenetic processes over time (Lucia, 1999). The resulting formation is highly heterogeneous and its internal structures may bear little resemblance to those initially created.

2.2.2.5 Summary

The carbonate formation resulting from the processes outlined above is highly heterogeneous over a large range of length scales. The biological origins of the sediment control the initial locations and types of sediment deposited, but this is also influenced by evolutionary changes in the organisms through time. Then changes in relative sea level control how the formation develops creating cycles of sediment. Finally, after burial, phases of diagenesis overprint the original depositional textures and alter their petrophysical properties. To understand carbonate formations, and hence carbonate reservoirs, requires information from across a range of length scales, from how diagenesis has altered micron sized pores right up to the kilometre sized reef structure.

2.3 How can we quantify this information?

The previous section explained why carbonate reservoirs are highly heterogeneous over a range of length scales. This next section will set out a variety of methods which can be used to capture and parameterise information about this heterogeneity.

Such information can be used to understand the layout and composition of these reservoirs. This is of particular interest when trying to exploit their economic potential particularly through the production of hydrocarbons.

This section discusses the range of methods for capturing heterogeneity information according to the length scale at which they are applied. Firstly reservoir analogues are discussed followed by inter-borehole methods and those applicable to individual boreholes. Finally I discuss methods which can be applied to extracted core samples and thin sections cut from them. I then discuss various strategies that can be used to integrate the results from methods applied at different length scales, before outlining the areas of the integration process in which more research is required.

2.3.1 Reservoir Analogues

2.3.1.1 Outcrop

The main barrier to our understanding of reservoirs is that they lie in the subsurface restricting our knowledge to sparsely located boreholes or low resolution seismic data. A solution to the problem is through the use of reservoir analogues. Analogues are outcrops, models or borehole studied examples of depositional settings with similar characteristics to the reservoir of interest. Once the depositional setting of the reservoir has been identified then it is be compared with an appropriate geologically consistent analogue if one exists (Alexander, 1993).

One source of reservoir analogues is to search for modern examples of the depositional setting of interest. This is an example of Charles Lyell's principle of uniformatarianism which explains that by studying what is happening at the present we can gain understanding of previous events. For carbonate production the modern depositional analogues include the Bahama bank platform (Purdy, 1963) and the ramp systems of the Persian gulf (Purser, 1973). The use of modern systems is very useful in understanding how depositional structures are formed but they lack any of the post burial diagenetic structures which are particularly important in carbonate reservoirs. Also in carbonate systems the carbonate maybe produced in situ and varies chemically, from calcite to metastable aragonite, according to water chemistry

which is known to have varied over geological time (Sandberg, 1975, 1983; Stanley and Hardie, 1998).

The study of outcropping geology is an obvious source from which to construct reservoir analogues as outcrops allow the detailed study of normally hidden structures. The study of outcrops has evolved from traditional geological mapping and sedimentary logging through the use of GPS systems to record highly accurate and dense datasets (Bryant et al., 2000). The range of length scales over which the outcrops vary are covered using a range of methods from aerial photography and seismic studies for the largest structures down to borehole studies to investigate petrophysical changes (McCaffrey et al., 2005). All these data sets can be brought together to create a 3D model to use as a reservoir analogue. An example of a detailed carbonate outcrop analogue is the Algerita escarpment, in the Guadaloupe Mountains, USA, which is an example of a carbonate ramp systems (Goggin et al., 1993; Wang et al., 1998). Algerita is particularly useful as the carbonate has been dolomitised prior to uplift and so has not been subject to alteration due to meteoric water during uplift and so retaining a porosity/permeability distribution very similar to the subsurface. Other borehole studied outcrop analogues include the Miocene Llucmajor platform in Mallorca (Pomar and Ward, 1999) and the lower Aptian (Cretaceous) carbonate outcrops in northern Oman which provide information about the large reservoirs within the Shauiba formation (Borgomano et al., 2002).

2.3.1.2 Geological Process Models

An issue with the use of both outcrop and modern analogues is that they maybe restricted to a limited number of examples for each depositional setting and therefore the features observed could be specific to the deposition location and not representative of the general physical depositional processes. A method for avoiding this problem is through the development of computer based process models which can be used to construct reservoir analogues. These models mimic the physical processes that control deposition (e.g. sedimentation rate, water depth, currents) and build up a range of possible geological realisations (Tetzlaff and Harbaugh, 1989; Waltham, 1992). Carbonate process models were initially restricted to 2D and

concentrated on the main process of sediment production, crustal subsidence and sea level change (Bice, 1988; Bosence and Waltham, 1990). With increases in computer processing power the models were expanded to 3D and to increase the number of processes modelled (Hussner and Roessler, 1996; Bitzer and Salas, 2002; Warrlich et al., 2002; Hill et al., 2008). The models are then validated using input data collected from real carbonate systems and comparing them with the model outputs (Scathro et al., 1989; Bosscher and Schlager, 1992).

The advantage of using a computer model is that they can be used to test theories as to how different processes interact to create the features observed such as how changes in sea level and subsidence produce carbonate cycles (Spencer, 1989; Burgess, 2001). One of the main issues with computer based analogues is that the accuracy of the output is dependant on the accuracy of the input parameters and of the equations used to represent true physical processes. As these are generally only known to within limits this results in a range of equally valid output models. Another issue is that not all of the processes which affect deposition can be included due to computational constraints.

Both outcrop and process model based analogues are very useful in allowing us to understand how different carbonate systems develop and then once buried how porosity and permeability might be distributed within in a subsurface reservoir. The key to the use of analogues is to be aware of their limitations. In the case of modern analogues it should be noted that depositional conditions such as sea water chemistry will be different from those in the past. Also the formation has not yet been subjected to the effects of burial and diagenesis. With outcrop analogues it should be remembered that these rocks have been brought to the surface and will be altered due to the effects of weathering and the flow of meteoric waters through them. In the case of computer based analogues it is not possible to capture every process and interaction which influences carbonate sedimentation. Also computer based models produce a range of different but equally valid simulations and care is required in their interpretation.

2.3.2 Inter-borehole Scale

The existence of a potential reservoir is determined largely using remote sensing methods such as reflection seismic surveys. These can image subsurface structures but only in terms of seismic velocity. For more detailed information boreholes are drilled from which specific rock types and packages are identified. This information is used to build up a picture of the reservoir structure between boreholes.

2.3.2.1 Inter-borehole Correlation

The simplest method to achieve this is through the inter-borehole correlation and interpolation of specific, easily identifiable horizons or packages. By linking these horizons and packages throughout a network of boreholes a 3D image of the reservoir structure can be created.

Correlation has conventionally been carried out manually. However such correlations can be highly subjective resulting in different results from different geologists, especially when dealing with complex structures. This has lead to the development of a number of computer-aided methodologies in an attempt to remove subjectivity. The methods still rely on manual classification of log data into stratigraphic units and key surfaces prior to correlation. Initial attempts were based on cross-correlation between pairs of boreholes with the optimal correlation being the maximum value of the cross-correlation function (Rudman and Lankston, 1973; Mann and Dowell, 1978). The method has been further improved through the use of weights based on bed thickness (Olea, 2004).

Another approach has been to utilise sequence matching techniques initially developed in molecular biology such as dynamic waveform matching (DWM). The DWM technique allows the thickness of units in a sequence to be varied. This allows the technique to cope with missing units and variable thicknesses of units (Smith and Waterman, 1980; Waterman and Raymond, 1987). A further refinement to this technique is through the use of dynamic programming which minimises a cost function based on differences between attributes of the two boreholes (Fang et al., 1992). Correlation techniques provide very simple information about what happens

between boreholes – simply that beds change thickness or disappear. For an indication of how the beds might change between boreholes requires more detailed methods.

2.3.2.2 Variograms

One method for predicting behaviour between boreholes is through the use of geostatistics. These are a set of tools which were developed for the mining industry to enable predictions to be made of ore grade potential between boreholes (Matheron, 1963). Geostatistical theory assumes that the data being investigated is a set of realisations drawn from an underlying random function. The aim then is to characterise features of this underlying distribution which can then be used to draw realisations in unsampled locations. The use of geostatistics makes the assumption that the underlying random function remains the same throughout the region and so the data can be described as stationary (Wackernagel, 1998).

The variogram is the main tool used in geostatistics to capture information about the underlying random function. It measures the expected degree of dissimilarity between pairs of points as a function of the distance between the points. The variogram is defined as:

$$\gamma(h) = \frac{1}{2n} \sum_{n} \left[\left(g(x+h) - g(x) \right)^2 \right] \qquad \ldots(2.1)$$

where $g(x)$ is the porosity data at position x, h is the separation between points, and n is the number of pairs of points with a separation h (Clark, 1979). By constraining the direction in which the distance between the pairs is measured, different variograms can be calculated revealing any anisotropy in the data. To enable the calculated variogram to be used to simulate data it must be replaced with a best-fit model variogram to ensure that it has physical meaning and that the random function it represents could exist (Wackernagel, 1998). Model fitting is generally done by eye but there have been several attempts to automate the process using a least squares method (Zhang et al., 1995; Jian et al., 1996).

Once a valid variogram model has been fitted it can then be used to simulate data in unsampled locations using a method called *kriging*. In ordinary kriging a weighted linear combination of neighbouring samples is used to estimate a value at unsampled locations. The weights are determined using the variogram model to ensure the estimation variance is minimised, in a method similar to standard linear regression (Armstrong, 1998). The kriging technique has been adapted to allow multiple sets of data to be used, such as borehole-derived porosity data and seismically-derived porosity data. The technique is known as *cokriging*. To achieve this variograms need to be determined for both sets of data, as was the cross-variogram between the two sets of data (Wackernagel, 1998; Yao and Journal, 2000).

2.3.2.3 Multi-point statistics

The use of traditional geostatistics for modelling has limitations as it is based on variograms. As variograms measure the expected variability between two locations they cannot capture curvilinear features of a reservoir such as meandering channels. To successfully capture such features requires techniques which take information from multiple-points (Strebelle, 2002). However to capture multiple-point statistics requires dense data coverage and when studying the subsurface data is only available from a limited set of boreholes. The solution is to use training images to capture the statistics. Training images are 2D (or 3D) datasets which contain examples of the geological structures which are thought to exist within the reservoir (Caers and Zhang, 2004). They can be taken from analogues observed at the surface, created from a simulation algorithm or can even be digitised by a geologist. Care needs to be taken when selecting which training images are used. As when calculating variograms, care should be taken to ensure that the training images are stationary (i.e. the features of interest are statistically repeated) to allow their multiple-point statistics to be captured.

The multiple-point statistics are measured by comparing the differences and spatial locations of a target cell with those around it. The number of cells involved is normally restricted to a limited number of neighbouring cells using a template. The

template is passed cell by cell over the training image and at each step the state of individual cells beneath the template, their position, and the state of the central cell is stored (Wang, 1996).

The creation of simulations based on the multiple-point statistics can be created using a number of different methods. An early approach was to use simulated annealing (Farmer, 1992). In simulated annealing a random image is created and then pixels are altered until a distance function (which compares the simulation statistics with the training image statistics) is minimised. This is a computationally intensive approach requiring multiple scans of the simulation image and it can be difficult to ensure the real distance function minimum is reached and not a local minimum.

Another borehole used approach is that of the *snesim* algorithm (single normal equation simulation) (Strebelle, 2002). In this algorithm any known data (e.g. borehole data) is assigned to simulation cells. Then a random path is determined which visits each cell without data once. Then at each cell a search is made for surrounding cells containing data (simulated or known), which is then used to construct a probability model using the multiple-point statistics measured from the training image. A draw is made from the probability model which is then assigned to the cell. This process is repeated until the simulation is filled. The advantage of this approach is that each cell is visited only once reducing computing time and also it is relatively straight forward to include information from other sources, such as seismic data, into the probability model to improve the simulation (Caers, 2002; Strebelle et al., 2002).

The use of multiple-point statistics is useful for capturing the curve-linear features poorly determined by variograms which are particularly important when dealing with reservoirs. However the technique is at present limited to data which has been divided into a limited number of states, often restricted to a binary system. This is due to the large number of interactions which are being measured, each increase in state dramatically increases the number of interactions which need to be measured.

The problem will be partially fixed through increases in computing power but there will still remain the issue of ensuring that a multiple state training image contains all the relevant interactions.

2.3.2.4 Markov chain simulation

Another approach related to multiple-point statistics is to capture sequences which are repeated in geology. Many of these sequences and patterns are assumed to be *Markovian* in nature (Davis, 2002). In a Markovian process the future state of the system depends only on the present state and the past states have no influence (Fisz, 1963). This implies that if the small scale behaviour is understood it can be used too replicate large scale behaviour.

In geology the subsurface is often divided into discrete units based on lithology or deposition. In such a discrete system the Markov process is known as a *Markov chain.* Markov chains can be used to simulate geological structures using transition probabilities, which give the probability of a cell containing a certain state given the state of neighbouring cells (Davis, 2002). The transition probabilities tend to be measured from real data rather than training images as in multiple-point statistics. Initially the technique was used to simulate vertical sequences with the transition probabilities being obtained from borehole data (Vistelius, 1949; Gingerich, 1969; Doveton, 1971). Work carried out in the field of image processing developed methods for combining Markov chains in a coupled chain to create multiple-dimensional simulations (Geman and Geman, 1984; Qian and Titterington, 1991). This was utilised to create 2-D geological simulations with the vertical transitions again taken from borehole data and the vertical transitions taken from outcrop data (Carle and Fogg, 1997; Elfeki and Dekking, 2001; Li et al., 2004). These simulations also allowed the conditioning of the simulation to real data.

As with multiple-point statistics the use of Markov chains has been restricted to discrete geological data. However as only a limited number of directions are involved it means there are far fewer interactions to measure and so more data states can be used. This means that the end simulation is more realistic in terms of the

variability of data types but it may poorly represent transitions out with the horizontal or vertical planes.

2.3.3 Single borehole scale

The drilling of boreholes allows access to the subsurface but due to the expense of extraction the amount of physical core samples recovered is generally limited in depth range. Instead a range of remote sensing logging tools have been developed which measure a variety of physical properties (e.g. sonic velocities, neutron density etc) as they are passed through the boreholes. Using the changes observed in the physical properties, predictions can be made about the lithologies within the borehole. The conventional use of such tools provides coverage of the entire borehole but coverage is limited to a 1D profile with a resolution of several feet (Rider, 2002).

Improvements in data acquisition have allowed the increased use of borehole imaging technology. Borehole images provide high resolution, 2D information about the borehole wall. Though they are called borehole images they can reflect changes in acoustic or resistivity properties as borehole as optical properties (Prensky, 1999). The advantage of high resolution, 2D information is that it reveals much of the small scale heterogeneities that are averaged over by conventional logging tools. These heterogeneities can be used to subdivide large formations to reveal more of there depositional history (Williams and Pirmez, 1999; Russel et al., 2002). They can even be used to identify specific fossil types aiding the interpretation of lithofacies (Hughes et al., 2003).

The topic of borehole logging is a very large field and a more indepth study is beyond the scope of this review. For further information on the field I refer the reader to existing reviews of the field (Timur and Toksoz, 1985; Hearst, 2000; Rider, 2002).

2.3.4 Core and below scale

2.3.4.1 Non-Destructive Methods

The only way to be completely sure of what lies in the subsurface is to extract physical rock samples. This allows detailed analysis of the rocks but is generally only available for limited regions of a borehole due to the cost of extracting the samples. These factors make non-destructive analysis methods, which preserve the sample, particularly important. One such method is to produce CT (computed tomography) scans of the sample. CT scans are produced by passing X-rays through a sample and measuring the attenuation of the X-ray beam due to the sample. The measurements are repeated as the sample is rotated and then back projection algorithms are used to construct a 2D image of the sample. By stacking a set of 2D slices together a 3D volume can be constructed based on changes in X-ray attenuation within the sample. The differences in X-ray attenuation can be attributed to changes in density caused by sub resolution porosity or areas with different chemical compositions (Duliu, 1999; Ketcham and Carlson, 2001). By restricting the size of the samples analysed the CT volumes can have a resolution down to 2 μm (Knackstedt et al., 2004). The high resolution images produced can be used to analyse the 3D distribution of fractures (Sellers et al., 2003; Vandersteen et al., 2003), to extract the pore network from which porosity and permeability estimates can be made (Arns et al., 2001; Arns et al., 2003; Knackstedt et al., 2004; Arns et al., 2005b) or to directly image fluid progression through a sample by taking repeated scans as a liquid with contrasting X-ray attenuation properties is pumped into one end of the sample (Hirono et al., 2003).

2.3.4.2 Destructive Methods

Another non destructive analysis method is the visual description of the rocks as if they were observed in outcrop at the surface to produce sedimentary logs. These logs can be used to identify different facies and help determine the stratigraphy of the rocks (Boyles et al., 1986). The visual descriptions can be tied to geophysical log data by measuring the geophysical properties of the actual samples (Rider, 2002).

The visual description of facies can then be used to aid the interpretation of the geophysical logs.

To visually identify the rock components requires that rock samples are cut up to produce thin sections. The thin sections are very thin slices of rock which can be analysed under a microscope or electron microscope (Anselmetti et al., 1998). This allows the rock sample to be described according to a standard rock classification system. In carbonate rocks the first classification systems were based on either the major constituents of the rock (Folk, 1959). This was then expanded to include the amount of cement/mud between the constituents (Dunham, 1962). These systems described the rock fabric and provide little information about the petrophysical properties of the rock. This lead to the development of a classification system based on the types of pore observed (Choquette and Pray, 1970). This was followed by classifications which linked specific rock fabrics with petrophysical properties (Lucia, 1983, 1995, 1999). More recently a classification scheme has been proposed which combines the pore types observed with the rock fabrics to provide permability estimation (Lonoy, 2006). This expansion of the classification systems to quantifying porosity and permeability is of particular importance when characterising reservoirs as these are the key properties which control fluid flow.

The analysis of thin sections is generally carried out manually. Attempts have been made to automate the process particularly when studying the pore network. The method involves the impregnation of thin sections with blue epoxy which fills the pore network. The pore network can then be easily identified in an optical image and the pore distribution measured (Mowers and Budd, 1996). The problem with the analysis of thin sections is that they represent only a small section of the rock and are restricted to a single plane. A solution to this problem is to capture the spatial statistics of the pore network from the thin section and then produce a range of simulations based on those statistics. This has been carried out using the multiple-point geostatistical method (Okabe and Blunt, 2004, 2005) and using a 2D Markov chain (Wu et al., 2004). The Markov chain method has been expanded to measure 2D Markov chains from 3 orthogonal thin sections and then combine these to create

3D simulations of the pore network. These simulations can then be used in fluid flow models to give accurate permeability information (Wu et al., 2006).

2.4 Integrating data

In carbonate reservoirs heterogeneity is observed over a vast range of length scales. It can be seen in the micron sized gaps between crystals that have under gone diagenesis, at larger scales (mm's to 100's of metres) the rocks are composed of skeletal material and so vary depending on both the species present and the position within the reef complex, and controls of sea level change and tectonics control the shape and structure of the reservoir at the kilometre scale laterally. To capture the heterogeneity within a carbonate reservoir requires the use of a range of the techniques outlined above. The techniques can provide detailed information about heterogeneity at specific length scales but to understand the behaviour of the whole reservoir requires the integration of this information. Some of the techniques described already offer some scope for data integration such as the use of seismic and borehole log data to constrain multiple-point geostatistical simulations (Caers, 2002; Strebelle et al., 2002). The process of integration is more generally carried out through some form of up-scaling process. Up-scaling is the process of converting high resolution data to a low resolution equivalent by taking some average value. The advantage of up-scaling is that it allows high resolution data from boreholes to be converted to a form which can be used as an input into a reservoir simulator which, due to the scale of the reservoir and the relatively intense computation required for fluid flow simulation, have a far lower resolution (Pickup and Hern, 2002).

2.4.1 Up-scaling in General

The individual measurements in a data set represent the value for a given sample size, known as the measurements *support*. If the measurements are repeated with a different sized support (i.e. different sample size) then both the values and variability of the measurements will usually change. This change can be illustrated if we consider a set of point measurements, a_x of a physical property and a second set of

measurements, b_x, of the same physical property but with a support which spans several of the point measurements (Figure 2.4.).

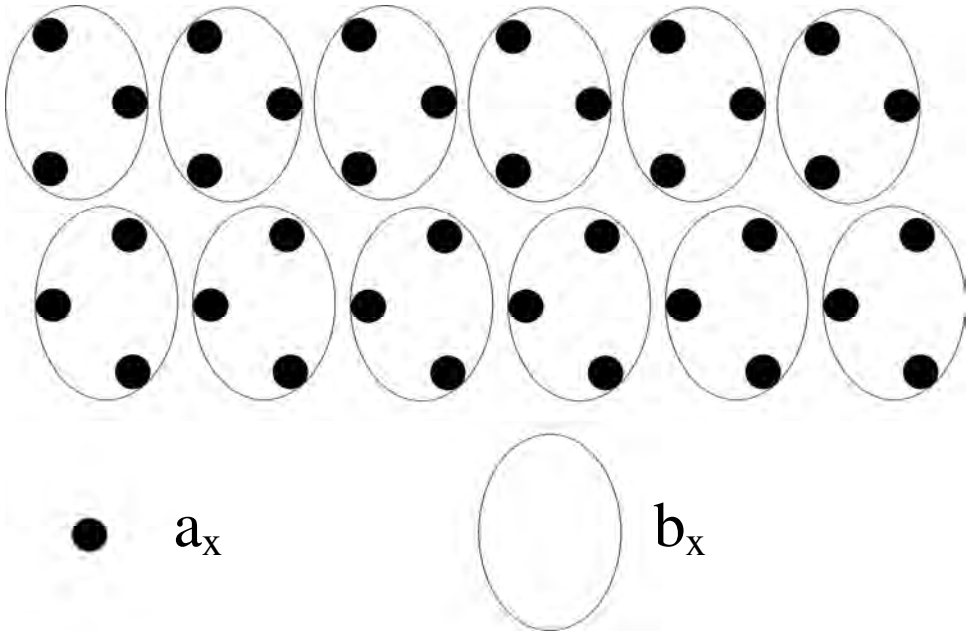

Figure 2.4. An example of why scaling is required. The two sets of measurement a_x and b_x have different supports and therefore require scaling relative to each other in order to be compared.

In this case the measurements, b_x, are some average combination of the point measurements a_x spanned by the support. The effect of this averaging is to lower the variability of the measurements b_x as it smoothes out the extreme values in the data set. The effect has been demonstrated using real core measurements of lead and zinc in (Clark, 1979) and also using porosity measurements in (Doveton, 1994). The aim of up-scaling is to replicate the type of averaging which occurs when measurements are repeated at a larger scale.

2.4.2 Permeability up-scaling

The bulk of the literature on up-scaling in the subsurface has concentrated on up-scaling permeability measurements as these are a key parameter in reservoir fluid flow simulations (Renard and Marsily, 1997). However permeability up-scaling is complicated as permeability is a non additive property (Wen and Gomez-Hernandez,

1996). This means that an average over a thin impermeable barrier (e.g. reservoir seal) and highly permeable surrounding rocks will have zero permeability at all resolutions. In special circumstances simple means can be used to perform up-scaling (e.g. the arithmetic mean parallel to infinite set of layers (Marsily, 1986)), but in general more complex methods are required. One such method is a variation on the averaging method and uses a power average in which the exponent depends on the spatial distribution and the result lies between the harmonic and geometric means (Journel et al., 1986). Other methods involve solving the diffusion equation using techniques such renormalisation (King, 1989) or tensors (Pickup et al., 1994). In an attempt to integrate information about the geological structure with these numerical solutions a method was proposed which divides the data by detecting large changes in the permeability. These regions are then scaled individually to create a more realistic model (Liu et al., 2002). The problem with many of these methods is in the amount of computational time required to achieve a result with the result that in order to obtain quick results the less valid methods are used in which either a mean value is taken or a high resolution sample value is assigned to a larger scale block (Renard and Marsily, 1997).

2.4.3 Variogram Scaling

In geostatistics a set of laws were developed for which allow both the up and the downscaling of variograms. These were developed to allow variograms calculated from different samples with different supports to be compared (Matheron, 1963). The scaling laws utilise the concept of a point scale variogram (the variogram which would be obtained if infinitely small samples were used) to calculate a variogram at any desired support (Frykman and Deutsch, 1999). A detailed description of the laws is provided in section 6.3. Once the variogram has been calculated for a new support then it can be used to create a kriging simulation. An example of the use of geostatistical scaling laws is in the comparison of heterogeneity measured in high resolution image logs with that measured in standard low resolution wireline logs (Tilke et al., 2006). The advantage of using variogram scaling laws is that they allow downscaling as borehole as up-scaling but the method is again computationally expensive requiring numerical integration over the different volumes of investigation.

2.5 What's missing

In order to fully integrate data gathered over a wide range of length scales still requires the solution of several key problems. One of these is the accurate correlation between data measured at different spatial resolutions and measured using different techniques. This is a requirement for both the development of scaling relationships and also for the relative positioning of different data sets within a reservoir model. In regions with large scale features, such as bed boundaries or faults, which can be observed in both data sets the problem is relatively straightforward (e.g. matching features in core and high resolution borehole images (Lofts and Bristow, 1998)). However in large formations away from such features the correlation of data sets is much more complicated. Without features the correlation has to be inferred from the nearest large scale feature. If the nearest feature lies some distance away this can result in a large degree of uncertainty in the correlation. In this thesis I propose a new correlation method based on matching the statistical features of the data distributions.

Another area requiring investigation is that of downscaling. As already highlighted there has been much work devoted to the problem of up-scaling. This has been principally driven by the need for realistic inputs into reservoir simulations. However in some carbonate formations the bulk of the porosity is found at the 10μm scale between crystals (Budd, 1989; Moshier, 1989). This lies borehole below the resolution of any of the available logging tools and can only be measured using rock samples. As the availability of rock samples is limited it would be useful to be able to estimate porosity and hence permeability by downscaling low resolution data. These estimates would allow fluid flow simulations to be carried out at high resolution and the results can then be up-scaled to input into reservoir models. The problem with downscaling is that as opposed to up-scaling which is a deterministic process, downscaling is a probabilistic process as the up-scaled data only constrains the probability distribution of possible down-scaled values. The geostatistical scaling laws offer a framework for downscaling and so in this thesis I will investigate their application to carbonate data through up-scaling carbonate measurements.

Another issue is the integration of data which sample different spatial volumes such as 2D borehole wall images with 3D core measurements. Permeability measurements made on a 2D data set will only capture connections in one plane and so may be very different to those made using 3D data. However as with the scaling problem the 3D data sets require physical rock samples and the bulk of data is restricted to 2D or even 1D borehole logs. If it was possible to capture spatial statistics from the borehole logs then these could be used to create 3D realisations. These realisations can then be used to constrain the range of possible porosity and permeability measurements. In this thesis I will develop a modelling technique which captures spatial statistics from borehole wall images and then simulates a range of valid realisations.

Chapter 3 - Data

3.1 Introduction

In this chapter I will introduce the data sets which were provided to the project to enable the relationships between extracted core and borehole logs to be investigated. Two sections of extracted core data were provided in the form of Computed Tomography (CT) scanned volumes, which representing changes in x-ray attenuation. The associated borehole data came from a Fullbore MicroImager (FMI) tool which provides resistivity images of the borehole wall. These images were provided to the project as well as a set of images which had been converted to porosity estimates.

3.2 Geological Background

All the data sets were obtained from a borehole through the Lower Cretaceous carbonate Shu' aiba Formation, which holds many prolific hydrocarbon reservoirs throughout the Middle East (Buchem et al., 2002). The Shu' aiba was deposited in a shallow marine carbonate ramp setting and grades broadly from packstones and wackestones to inter-mixed rudist grainstones and algal boundstones (Alsharhan, 1987; Pittet et al., 2002). Much of the lime mud has been recrystallised as microrhombic calcite crystals (1-10μm), and a considerable proportion of the Shu' aiba's porosity lies between these crystals with typical pore diameters of less than 2μm (Budd, 1989; Moshier, 1989).

3.3 Core Data

Two sections of extracted core where provided to the project. One was 120mm in length and the other 165mm in length with a 500ft difference in depth between them. Each of the core sections was extracted from of a section of rudist rudstone. The only obvious large-scale features within the cores are shell fragments from a marine bivalve known as a rudist. These fragments are typically elliptical, up to 1" (25mm) in length and 0.6" (15mm) in width. The outer shells of rudist valves are composed of low-Mg calcite and hence are generally preserved; the inner valves, originally composed of aragonite, are now represented by either recrystallised calcite or large

vugs. The cores had previously been scanned using X-ray computed tomography (CT) to produce a 3D volume made up of volume elements known as voxels. The voxels are cubic with dimensions of 0.006" (0.165mm) which represents the resolution of the tomogram. The CT scan assigns to each voxel a value representing the average linear X-ray attenuation of the material bounded within that voxel. As no siliciclastic material has been observed in the formation, and the abundance of high-magnesium echinoderm debris is minimal, the core samples were assumed to be composed largely of low magnesium calcium carbonate (personal communication, R. Wood 2006). Since the carbonate core is essentially monomineralic, changes in linear attenuation reflect changes in density (Duliu, 1999; Ketcham and Carlson, 2001). It follows that the observed changes in CT value can be explained mainly by changes in the porosity of the material within each voxel, which is due to the variation in the distribution of micropores with lengthscales beneath the tomogram resolution.

3.4 Borehole Data

Almost 770ft of borehole data was also made available from a Fullbore MicroImager (FMI) tool. The FMI tool has a series of electrode pads which are sprung to press against the borehole walls. Current is passed into the formation and measured at the electrodes. These measurements are converted to local resistivity estimates and plotted as an image. The resolution of the FMI data is defined by the electrode spacing and is 0.1" (2.54mm) (Safinya et al., 1991). Note that this is more than an order of magnitude larger than the CT data resolution.

The FMI data from the borehole had previously been converted to a measure of porosity by Tilke et al (2006). The porosity estimates were calculated using the following relationship:

$$\Phi = \Phi_{Ave} \frac{R^{-1/m}}{R_{Ave}^{-1/m}} \qquad \ldots(3.1)$$

where Φ is porosity, R is the resistivity of the borehole wall, m is the cementation exponent and the subscript Ave indicates an average value for a given depth. The relationship is derived from the classic Archie saturation equation. The average porosity value for a given depth was taken from a conventional porosity logging tool. The cementation exponent was taken from laboratory core measurements (Ragland, 2002). In this borehole, m was 2.0 for the interval of investigation, within measurement uncertainty.

3.5 Correlation between Core and Borehole Data

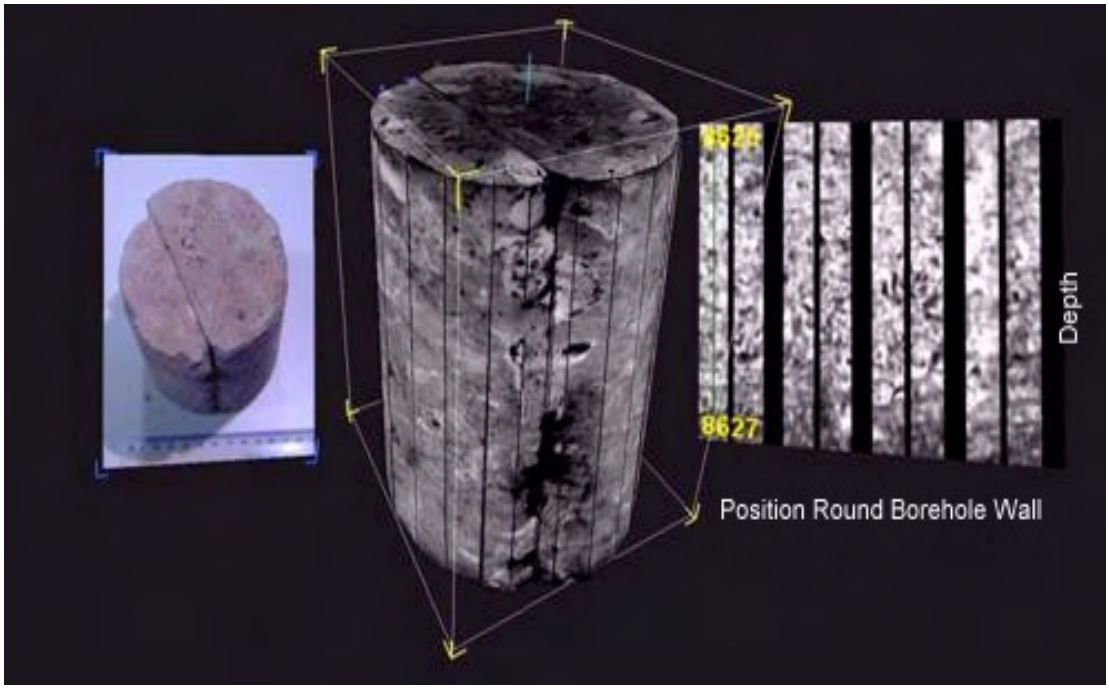

Figure 3.1 An illustration of the data sets used in the project. On the left is a photograph of one of the extracted core sections, while in the centre is the CT scan made of the core section. On the right is the corresponding 2ft section of porosity converted FMI data.

The FMI and extracted core sections were all obtained from the same well. Due to the different systems used to measure the depth of two data sets there is a mismatch between their measured depths. Attempts to correlate the data sets using bedding planes and other distinctive lithological marker features were only able to constrain the correlation to within 2ft (609.6mm) (personal communication, P.Tilke 2004). The core section with a measured depth 8626ft correlates with the region 8637ft to

8639ft within the FMI data and the 8121ft core section correlates with the 8133.25ft to 8135.25ft section of FMI.

The uncertainty in the correlation is primarily due to the large distances between bedding planes in the formation. However, during the process of core extraction a 2" annulus of rock is lost between the core and the borehole wall. To aid correlation any lithological feature would have to span the 2" gap, but the largest features observed in the core sections are the 1" fragments of rudist shell.

The correlation between the data sets has been constrained using bedding planes to within 2ft. However this is still over 5 times the length of the core sections and given that the bulk of the porosity within the formation is at the micron scale, a further improvement is required if the porosity is to be investigated between the data sets.

Chapter 4 - Statistical Correlation between Geophysical Logs and Extracted Core

The work presented in this chapter has been published in the journal Geophysics (Price et al., 2008), and has been presented in poster form at the IMA Modelling Permeable Rocks Conference 2007, Edinburgh.

4.1 Introduction

In this chapter a solution is proposed to the correlation problem for depth intervals in between marker features by matching a cascade of statistics of the core and log measurements. The individual statistics are calculated for each data set individually and correlations between them identified. The matching of individual statistics produces multiple possible correlation locations. By combining the results from a number of statistics using a joint likelihood function, a powerful prediction tool is created.

We apply the developed method to correlate Fullbore MicroImager (FMI) log data with a section of X-ray Computed Tomography (CT) scanned carbonate reservoir core. While core and logs contain many more detailed features within their complex porosity distributions, these features do not span the interval between the outer core surface and the borehole wall (an annulus of rock between the two surfaces of approximately 2" (50.8mm) thick is lost during the coring process), and hence can not be used for direct visual correlation. As a result, it was only possible to locate the core section to within a 2 foot section of the log data using the standard method of visually matching lithological features. I attempted higher resolution correlations using the following porosity statistics: mean, variance, and the spatial range. As expected these statistics produce relatively uncertain results when applied on their own. However when combined in a likelihood function they enable the correlation to be constrained to within 0.06ft or 0.72” (18.29mm).

4.2 Data Processing

Before any statistical methods could be used, a number of processing steps were applied to the CT scan of the extracted core to make it comparable to the FMI derived data. There were artefacts created during the scanning process which were removed. The data had to be converted to an estimate of porosity to match the FMI. Finally the CT data was averaged spatially to a resolution matching that of the FMI.

4.2.1 Removal of Artefacts from CT Data

X-ray CT scanners measure the attenuation of an X-ray beam that has passed through a sample. The sample is rotated and the attenuation measured at regular angular intervals. A back-projection algorithm is then applied to the data to create a 3D reconstruction tomogram of the sample's attenuation properties.

This technique works well for scanners using single energy frequency X-ray beams (monochromatic signals). Most scanners, however, use X-ray beams that are composed of a range of energies, which creates artefacts in the tomogram as X-ray attenuation is energy dependent. High energy X-rays are preferentially attenuated compared to low energy X-rays. The incident X-ray beam therefore changes energy composition as it passes through the sample. The outer parts of the sample will be measured using the complete beam when facing the source and an attenuated beam when facing the detector. If the sample is circular the centre of the sample will be measured by a beam of similar (depleted) energy composition at all rotations. The resulting artefact, known as beam hardening, is manifested as a gradient from high CT values at the edge to low CT values at the centre of the image. This gradient does not reflect actual heterogeneity within the material.

The artefact is reduced during the scanning process by using filters to pre-attenuate high energies in the X-ray beam (Curry et al., 1990). However, some residual beam hardening remains in the tomogram of the extracted core. It is most noticeable in a vertically averaged profile through the core (Figure 4.1).

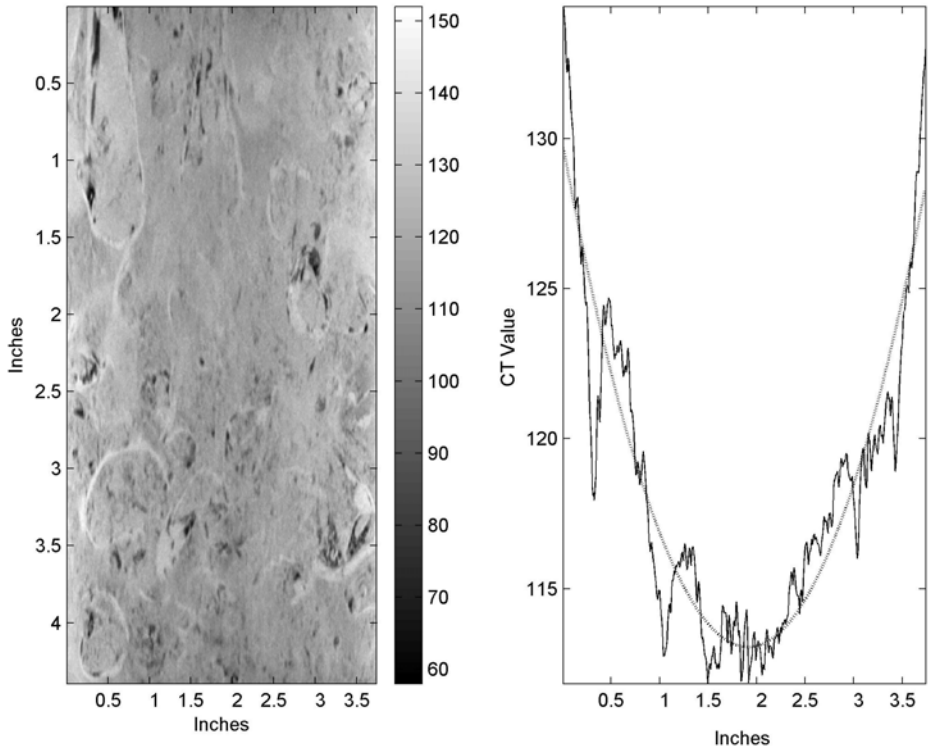

Figure 4.1 (left) Vertical slice through the centre of the CT volume. Colour scale represents differences in CT value and hence X-ray attenuation. (right) Vertically averaged CT values from the slice (solid) with fitted polynomial (dotted) used to correct for beam hardening.

To remove the artefact, the vertically averaged profile was fitted with a 2nd order polynomial (Figure 4.1). Horizontal slices were extracted from the CT volume and the centre of the core within each slice determined. Then each voxel within the slice was assigned a correction factor from the polynomial, determined by its radial distance from the centre of the core.

4.2.2 Conversion of X-ray density to Porosity Estimates

To enable statistics to be compared between different data sources they must reflect a common property. Key to our analysis is the assumption that the core sample can be considered essentially monomineralic. Under such an assumption, differences in X–ray attenuation can be attributed to averaging over varying porosity below the resolution of the CT data. Therefore a method was devised to derive porosity estimates from the CT data.

The CT data were stored using 8 bits and hence lie in the range 0 to 255. The value 0 is assigned to the least attenuating voxel of the scan while the value 255 is assigned to the most attenuating voxel which is often part of the scanning apparatus. Using the assumption above, low attenuation areas (low CT values) correspond to porous areas of the core. The lowest CT values will be assigned to large pores and to the air surrounding the core, and have porosity equal to 1. The high attenuation areas (high CT values) will have low porosity, closer to 0.

The following relationship was used to convert CT values to porosity estimates. It assumes that there exists a dense carbonate region with zero porosity at the lengthscale of the CT data which has been assigned the value C_{Max}:

$$P(x, y, z) = \frac{C_{Max} - C(x, y, z)}{C_{Max}} \qquad \ldots(4.1)$$

where *C(x,y,z)* is a CT value at each location and *P(x,y,z)* is the corresponding porosity estimate.

The maximum CT value corresponding to a carbonate voxel correlates with the outer, calcite layers of rudist shells (large, oval features observed in Figure 4.1, left). The low Mg calcite outer parts of rudist valves possess a prismatic microstructure with virtually zero porosity (Figure 4.2). This made them resistant to the recrystallisation process that created microporosity in the Shu' aiba. Hence these shell fragments have little or no porosity and correspond to high CT values compared to the surrounding matrix.

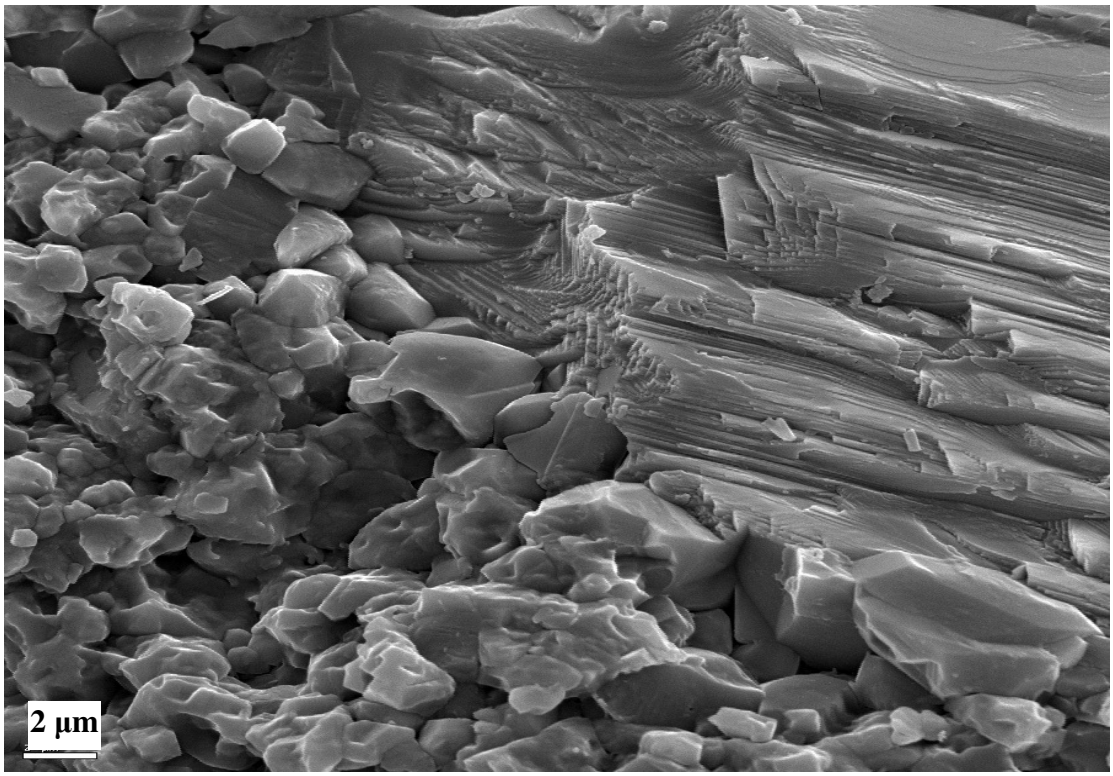

Figure 4.2 Scanning Electron Microscope (SEM) image of carbonate matrix with microporosity (left), and the outer part of a rudist valve composed of virtually zero porosity, prismatic, low Mg calcite (right). The white bar (lower-left) is a 2µm lengthscale.

However, the maximum CT value overall within the core was 150 and occurred in slice 359 (Figure 4.3). This voxel does not correlate with a fragment of rudist shell. It is an isolated and sharply defined anomaly. This suggests that it was caused by an anomalous material, probably a series of diagenetic pyrite framboids.

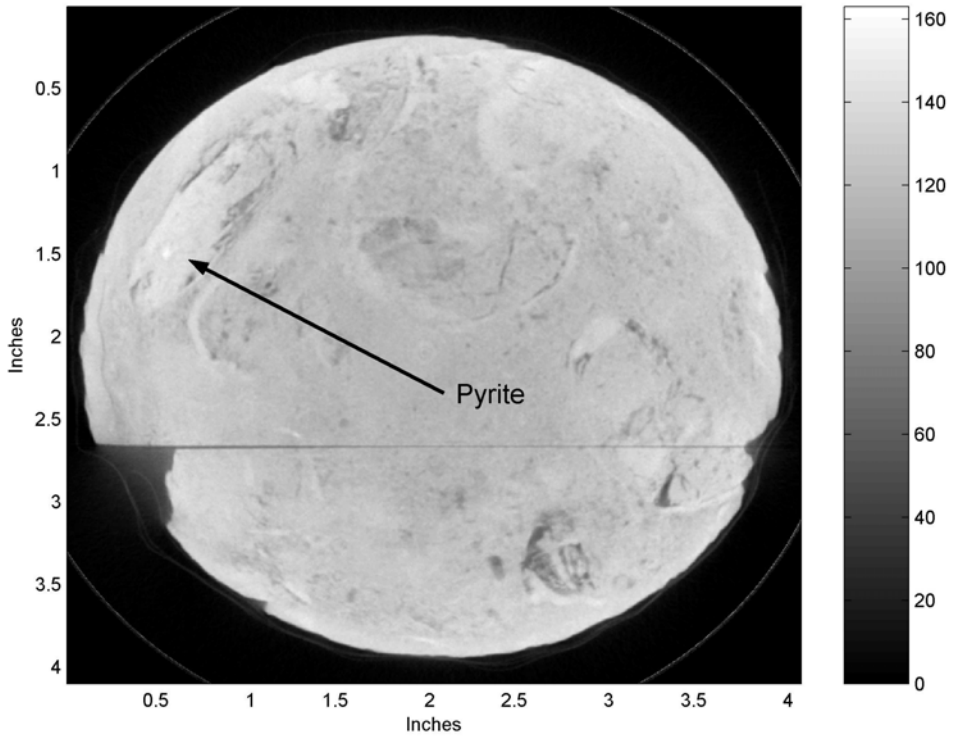

Figure 4.3 Horizontal slice through CT volume containing maximum CT value.

The presence of pyrite within the core sample threatens the assumption of monomineralic composition. However similar peaks in CT value are only observed in a limited number of slices. I therefore make the assumption that pyrite is rare, and volumetrically insignificant, within this section of core (personal communication, R. Wood, 2006).

The background maximum was then taken as the maximum CT value for a carbonate voxel. This was observed to be 144 ± 2. This range of values correlates with fragments of rudist shell.

The tomogram and the FMI data have resolutions of 0.006" (0.165mm) and 0.1" (2.54mm) respectively. To enable statistical comparison between the data sets they were converted to the same resolution. This was achieved by averaging the CT data to the same resolution as the FMI data using a 3D kernel of weights:

$$Kernel(i,j,k) = \frac{\left(1+\sin\left(\left(\frac{i}{15}\right)*\pi+\frac{\pi}{2}\right)\right)*\left(1+\sin\left(\left(\frac{j}{15}\right)*\pi+\frac{\pi}{2}\right)\right)*\left(1+\sin\left(\left(\frac{k}{15}\right)*\pi+\frac{\pi}{2}\right)\right)}{8} \quad \ldots(4.2)$$

where i, j and k are the discrete x, y and z coordinates of each voxel in the kernel discretised by the CT data at 0.165mm. The kernel used was 31*31*31 voxels in size. The choice of kernel size was determined to make the central section, with weights above 0.5, correspond to an FMI-sized pixel (15*15 CT voxels in size).

4.3 Correlation Methodology

In order to compare individual statistical values either between core length windows of FMI data down the borehole, or between CT and FMI data, a non-dimensional misfit measure is used:

$$M(x) = \sqrt{\frac{(T(x)-T)^2}{\sigma^2}} \quad \ldots(4.3)$$

where $M(x)$ is the misfit at depth x, $T(x)$ is the observed value of any particular statistic in the FMI data at depth x, σ is the standard deviation of $T(x)$, and T is the reference value of the statistic in the area of interest. For statistics other than the mean, the value of σ^2 is taken to be the variance of each statistic $T(x)$ within the 2ft region of the well from which the core was known to have been extracted.

The misfit for statistic i is normalized to lie between 0 and 1 by converting to a likelihood function, $L_i(x)$, using (Tarantola, 1994),

$$L_i(x) = \exp\left\{-[M(x)]^2\right\} \quad \ldots(4.4)$$

which is valid for the Gaussian uncertainty on the values of the statistics. The Central Limit Theorem (Hoel, 1962) is used to justify this choice. The likelihood increases with improved fit (unlike the misfit), and can also be calculated for more than one statistic. A joint likelihood function for n independent statistics is given by:

$$J(x) = \prod_{i=1}^{n} L_i(x) \qquad \ldots(4.5)$$

The proposed correlation method requires statistics to be identified that have predictive power when used to correlate core data to geophysical data. These statistics were identified by calculating the entropy of normalized likelihood functions, using:

$$H = -K \sum_{i}^{I} p_i \ln p_i \qquad \ldots(4.6)$$

where p_i is the normalized likelihood at location i and K is a constant relating to the measurement scale. The entropy value is the negative of the information represented by the normalized likelihood function. Low entropy values indicate that a likelihood function contains more information than one with high entropy values (Shannon, 1948).

Finally there is always have prior information about the likely correlation of core and logs (e.g. from the closest marker horizons, or operationally measured core and log depths). If this information is described by a probability distribution $\rho(x)$, then our final uncertainty in correlation depth is represented by $P(x) = \rho(x)J(x)$ by Bayes theorem. In this paper, the prior is chosen to be uniform: constant within the 2 foot (609.6mm) interval and zero elsewhere. Hence, $P(x) \alpha J(x)$ within the interval and $P(x) = 0$ outside it.

4.4 Statistics

A number of statistics were applied to the data sets. The first four moments of the data distributions were used, as well as the geostatistical range parameter. As the range parameter was calculated on a curved surface instead of a plane, a new technique for its automatic determination was developed.

The following equations 2.8 to 2.11 are the first four moments of the distribution of values $g_1,\ldots,g_N$.

Mean: $$\bar{g} = \frac{1}{N}\sum_{j=1}^{N} g_j \qquad \ldots(4.7)$$

Variance: $$\sigma^2 = \frac{1}{N-1}\sum_{j=1}^{N}\left(g_j - \bar{g}\right)^2 \qquad \ldots(4.8)$$

Skewness: $$Skew = \frac{1}{N}\sum_{j=1}^{N}\left[\frac{g_j - \bar{g}}{\sigma}\right]^3 \qquad \ldots(4.9)$$

Kurtosis: $$Kurt = \left[\frac{1}{N}\sum_{j=1}^{N}\left[\frac{g_j - \bar{g}}{\sigma}\right]^4\right] - 3 \qquad \ldots(4.10)$$

The mean and variance are well known. The skewness and kurtosis are non-dimensional. Positive skewness values indicate a distribution with a longer asymmetric tail towards larger values and vice versa. The kurtosis describes the peakedness or flatness of a distribution compared to a Gaussian distribution, with positive values being more peaked. A potential problem with the skewness and kurtosis is that they are higher order statistics and hence are known to have larger sampling errors than others (Bulmer, 1979).

The variogram is a measure of the expected dissimilarity between pairs of points as a function of the distance between them. The definition of variogram used in this study is:

$$\gamma(h) = \frac{1}{2n}\sum_{n}\left[\left(g(x+h) - g(x)\right)^2\right] \qquad \ldots(4.11)$$

where *g(x)* is the porosity data at position *x*, *h* is the separation between points, and *n* is the number of pairs of points with a separation *h* (Clark, 1979).

An example of one of the variograms calculated for a particular window of the FMI data is shown in Figure 4.4. The variogram follows the classic shape, rising steeply at first then levelling off. The variance at which the variogram levels off is termed

the sill. The distance (or lag) at which the sill value is attained is termed the range. Conventional variogram analysis involves fitting a model variogram to the calculated variogram which allows the variograms to be described and compared by their sill and range values.

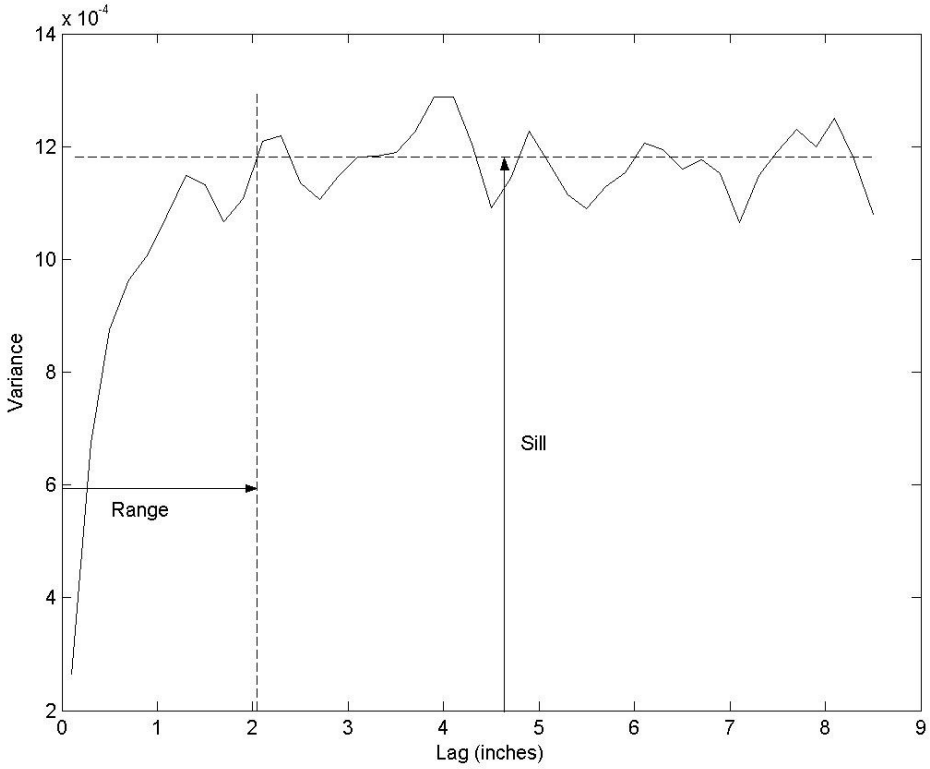

Figure 4.4 An example of a calculated variogram with the key terms used to describe its shape.

Most least-squares model-fitting algorithms implicitly assume that the number of points separated by short distances is far greater than the number separated by larger distances (this occurs when a variogram is calculated for data distributed over a plane such as a map). The assumption biases the model fitting algorithms towards fitting the initial rise and plateauing of the variogram curve which leads to accurate estimates of the sill and range parameters. However the FMI data was collected around circular surfaces and hence have a greater number of pairs of points separated by large distances than small distances. Therefore, a new technique was required to estimate the range and sill parameters.

Variograms calculated from the FMI data are generally noisy so the data was smoothed. The smoothing was carried out using a 1 inch moving average filter. An example of the smoothed data is shown in Figure 4.5 (dotted line). The sill value was then taken from the smoothed data by averaging between lags 4.5" to 6.3", an interval chosen to span part of the steady state region and to be unaffected by edge effects caused by the smoothing process. The range was then defined as the first crossing point of the estimated sill value with the original (non-smoothed) variogram (Figure 4.5).

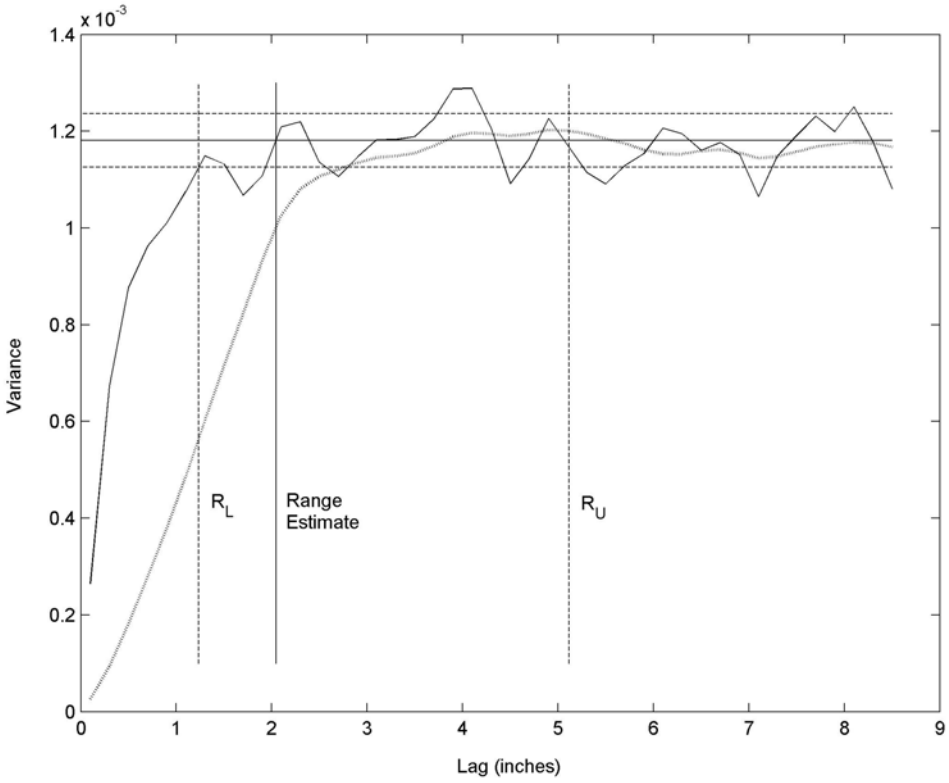

Figure 4.5 Example of range fitting. The calculated variogram (solid) is smoothed (dotted) and then the average sill (solid horizontal) and its bounds (dashed horizontal) are calculated. The range estimate is the lag at which the calculated variogram and average sill first cross, RL the lag at which the calculated variogram and the lower sill bound cross and RU is calculated from equation 4.12.

The point pairs in FMI data used to find the sill are separated by large distances relative to the size of the largest significant sedimentary features in the core (rudist

shell fragments). Hence the sill value should be similar to half the calculated variance within each window. The variance statistic will be used independently from this fitted model (equation 4.8) so the principal new statistic estimated by the above process is the range. One advantage of using the range estimate is that it does not depend on the absolute linear scaling of the porosity data. Hence the range is unaffected by any errors introduced by that scaling.

To estimate the possible error in the range estimate, R, the standard deviation, σ_R, of the original variogram from R to the maximum lengthscale (8.5") was calculated (horizontal dashed lines, Figure 4.5). The lower bound, R_L, was then taken as the first crossing of the sill minus one standard deviation with the original data.
A similar approach was tried for the upper bound, R_U, but the results were erratic. Instead R_U was defined as the *expectation* of the crossing between the sill, S, plus one standard deviation and the original data, calculated using:

$$R_U = \frac{\sum_x \exp\left\{-\left[\frac{[f(x)-(S+\sigma_R)]^2}{2*\sigma_R{}^2}\right]\right\} * x}{\sum_x \exp\left\{-\left[\frac{[f(x)-(S+\sigma_R)]^2}{2*\sigma_R{}^2}\right]\right\}} \qquad \ldots(4.12)$$

where $f(x)$ is the original variogram. An example of the lower and upper bounds R_L and R_U, respectively, are shown in Figure 4.5.

4.5 Results

4.5.1 Testing the Differentiation Power of Statistics

In order to test the power of various alternative statistics independently from the FMI-CT correlation data methodology, a test was made of the ability of each statistic to differentiate the FMI-derived porosity distribution within the targeted 2ft depth interval from the FMI-derived porosity distribution in the rest of the borehole. Thus avoiding the circularity of argument of both testing and applying each statistic to the FMI and CT correlation problem.

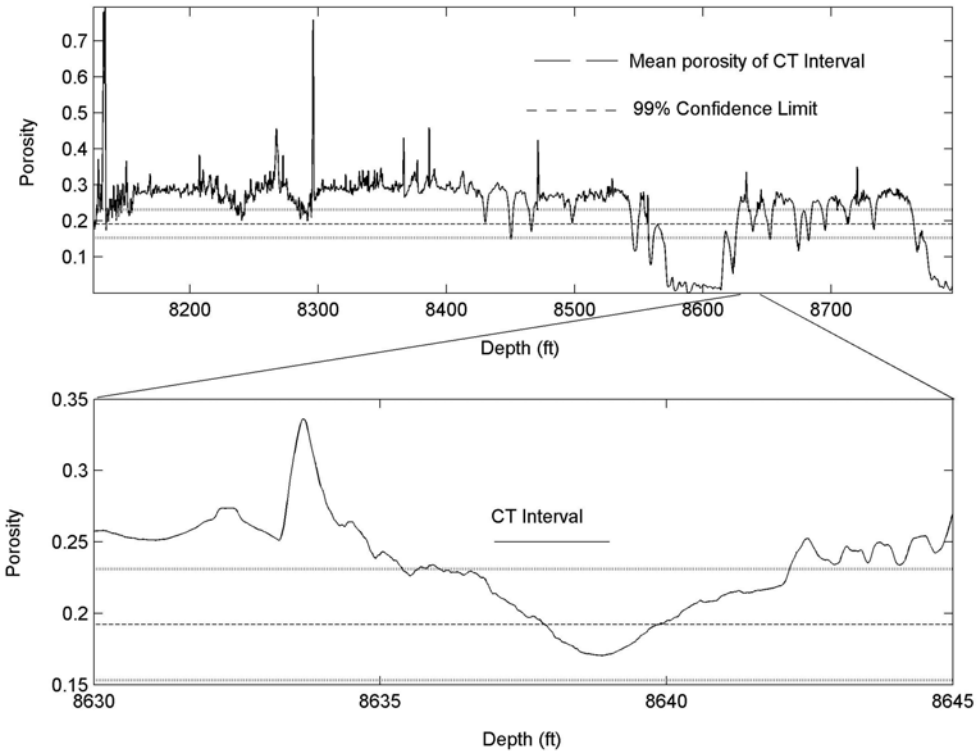

Figure 4.6 The calculated mean FMI-derived porosity values for windows of FMI, plotted against depth.

Each of the statistics was calculated for core length (116mm) windows of the FMI derived porosity data. Between each calculation the window was moved down the well by one horizontal row of data (0.1" (2.54mm)). This resulted in 80,478 windows and associated statistic values. The mean estimates calculated for windows of FMI data are shown in Figure 4.6 as a function of depth. The top plot shows the results for the available FMI data, while the bottom plot focuses on the region from which the core was extracted. The 2ft target interval, from which the core was extracted, is marked as the "CT interval". The average value of the mean, and its standard deviation, σ, within the windows of the CT interval was also calculated (Figure 4.6): 99.7% of the values lie within the range μ +/- 3σ (dotted line, Figure 4.6). To test the differentiating power of the mean, a set of likelihood functions (equation 4.5) were calculated to compare each core-length window (120mm in length) within the CT interval against the rest of the borehole. Likelihood values of

1 indicate regions with the similar mean values, while values close to 0 indicate regions with significantly differently mean values. A selection of four of the likelihood functions are shown in Figure 4.7 for four core-sized windows within the CT interval.

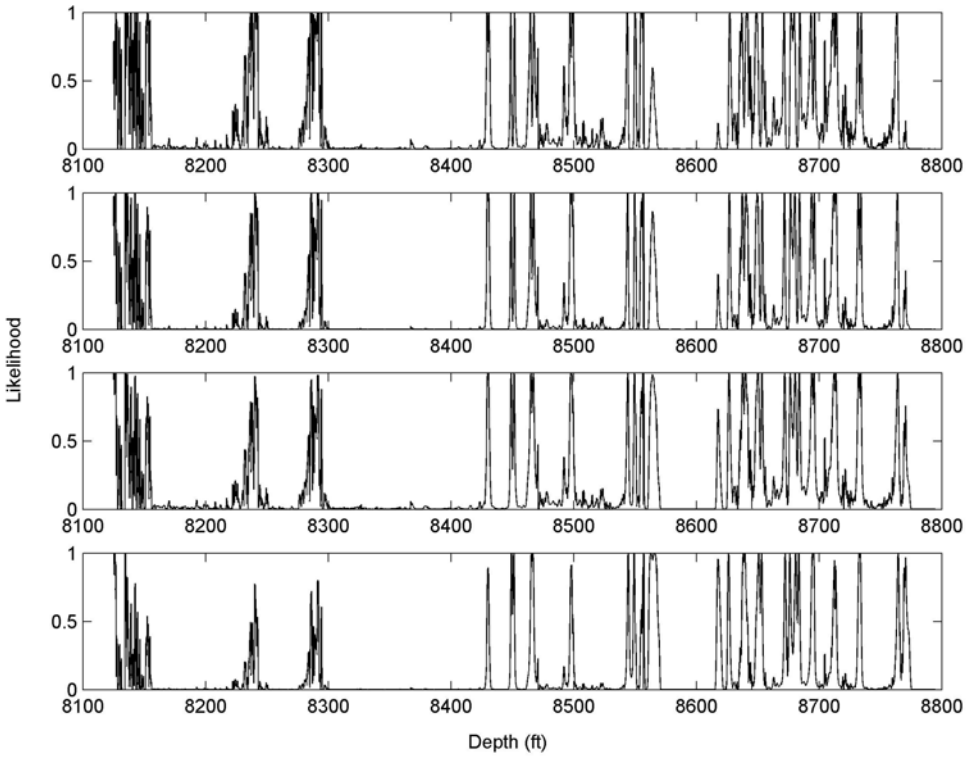

Figure 4.7 Four separate likelihood functions. Each likelihood function was created by comparing a separate core-length window within the CT interval with the rest of the borehole.

To measure the depth differentiation offered by the different likelihood functions, the entropy (equation 4.6) was calculated for each. A similar procedure was repeated for the other statistics and all calculated entropy values are shown in Figure 4.8 (lines connecting values using the same core-length window).

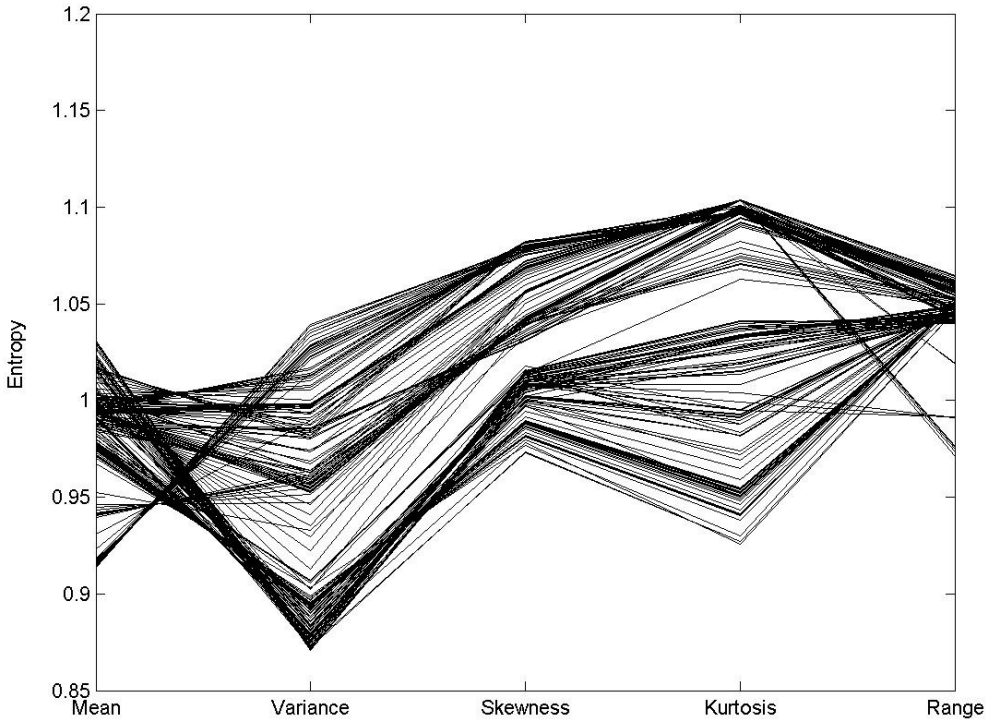

Figure 4.8 The entropy for each of the likelihood functions comparing the core-sized windows within the CT interval and the rest of the core, calculated for each statistic.

Likelihood functions with low entropy values contain more differentiation (or correlation) information than those with high entropy values. Therefore the entropy results in Figure 4.8 show that the variance generally contains the greatest depth differentiation, followed by the mean. The skewness, kurtosis and range statistics contain roughly similar amounts of information.

The appropriate order in which to combine the likelihood functions was determined using the entropy of the functions. A range of joint likelihood functions were calculated using different combinations of statistics. Each of the combinations involved the variance since it contains the most information. The resulting entropy values averaged across all windows within the CT interval are shown in figure 4.9. The results show that when using two statistics, the combination of variance and mean provides the most information. When using three statistics the addition of the range parameter provides the most information.

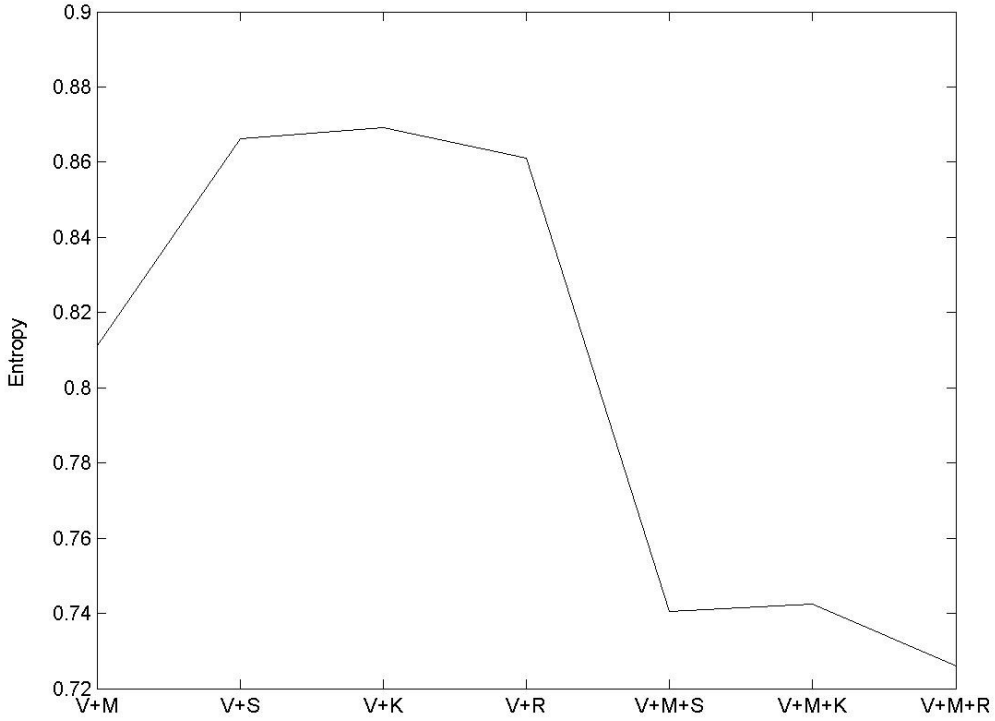

Figure 4.9 The entropy for each of the likelihood functions comparing the windows within the CT interval and the rest of the core, calculated for different combinations of statistics (V=variance, M=mean, S=skewness, K=kurtosis, R=range).

4.5.2 CT Results

Having determined the order in which to combine the statistics in the correlation method using the FMI data, the first four statistical moments were then calculated from the averaged CT volume and the results are given in Table 4.1. The values in the Estimate, Upper and Lower bound columns were calculated using porosity values derived using CT maximum values 144,142 and 146 respectively in equation 4.1. The Skewness and Kurtosis each have only one calculated value as these statistics describe the shape of the distribution and are independent of the choice of maximum CT value.

Table 4.1 Conventional Statistics that describing the CT data.

	Estimate	Upper Bound	Lower Bound
Mean	0.214	0.224	0.203
Variance	0.001	0.001	0.001
Skewness	0.338	-	-
Kurtosis	1.139	-	-

A horizontal variogram was calculated for the averaged CT data using Equation 4.11. For the CT data the horizontal distances were assigned to 35 0.1" (2.54mm) bins with centres between 0.1" and 3.5". The calculated variogram is shown in Figure 4.10. The variogram in Figure 4.10 is unlike the 'classic' variogram shape shown in Figure 4.4. It climbs steeply initially then levels off around a lag of 0.5"; at a lag of 1.75" it starts to climb again, the slope increasing with increasing lag. This behaviour suggests that at least two different lengthscale processes are responsible and this type of variogram is generally referred to as nested.

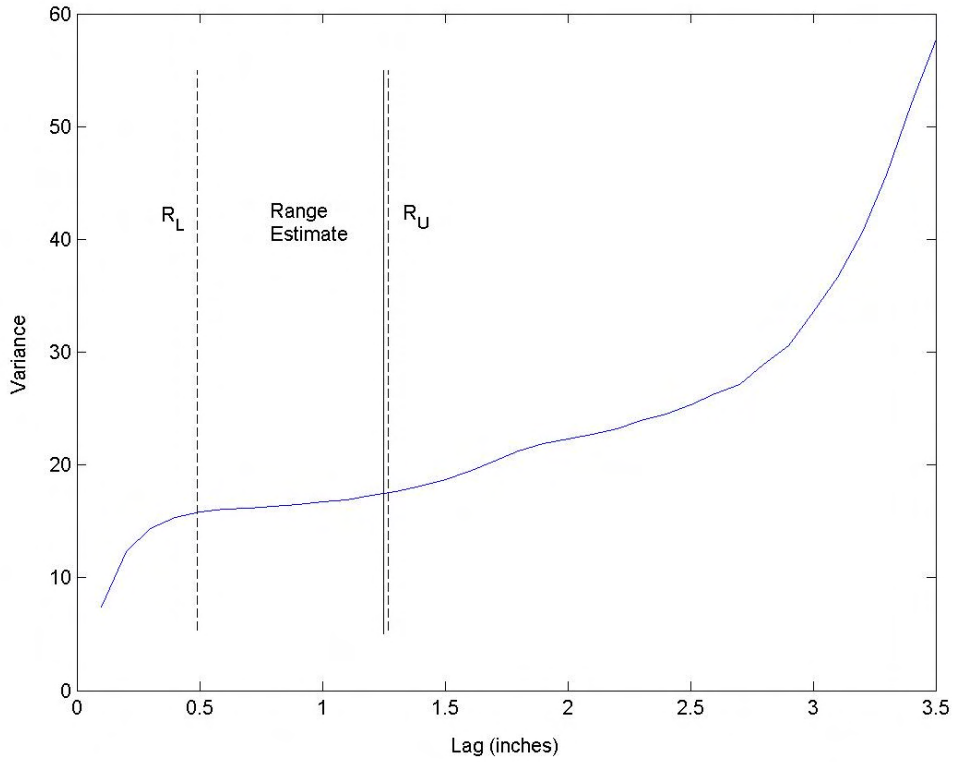

Figure 4.10 Horizontal variogram calculated for the averaged CT volume, with the range estimate and its upper and lower bounds marked.

Unlike the FMI variograms previously, the averaged CT volume variogram is better determined at short lags. This is due to the larger number of pairs of points separated by short distances compared to pairs separated by larger distances within a volume. Therefore the calculation of the range, using the same algorithm as for the FMI variograms, used the data between 0 and 1.75". The estimated range for the averaged CT volume was 1.25" with a lower bound of 0.49" and an upper bound of 1.27".

4.5.3 Likelihood Functions

Using the likelihood function defined in equation 2.5, the statistics from the two data sets were compared. From the entropy results (Figure 2.8) the variance was shown to be the statistic containing the most information. The likelihood function for the variance values is shown in Figure 2.11. The three curves reflect the three estimates of the porosity derived using different maximum CT values. The curves are similar

and show strong likelihood values (>0.5) in the region 8637ft to 8637.6ft and around 8638.05ft and 8638.4ft. These suggest that the core was extracted from somewhere within one of these regions.

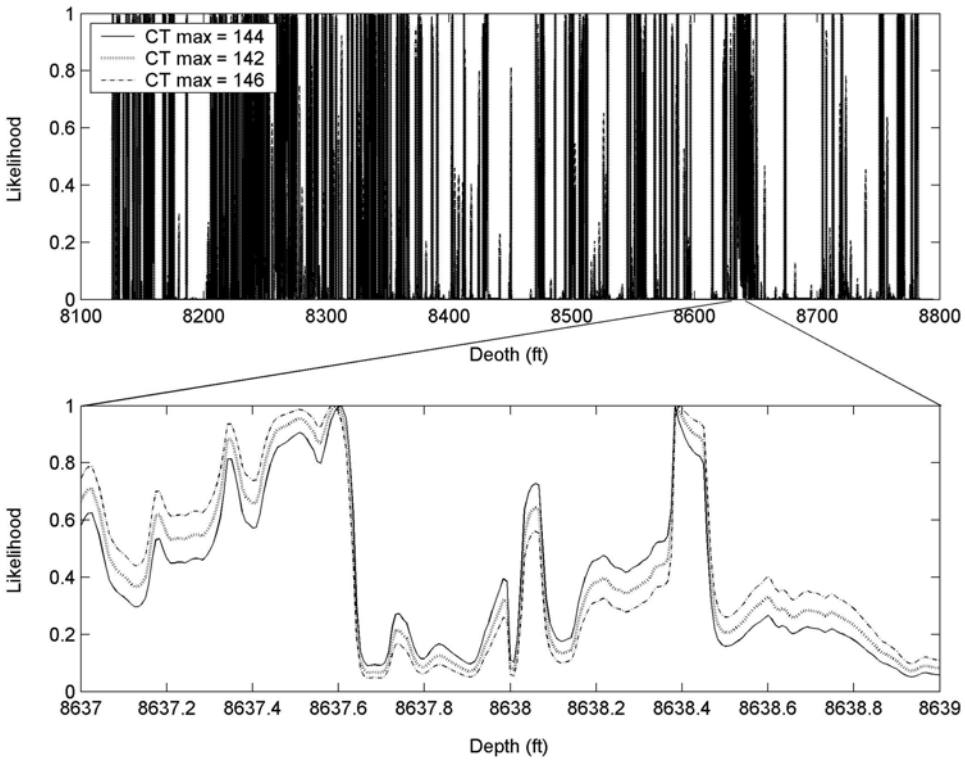

Figure 4.11 Comparison of CT and FMI variance values using likelihood function: (top) whole borehole; (bottom) CT interval.

The pair of statistics containing the most information was shown to be the variance and the mean and hence the joint likelihood between these statistics was calculated and shown in Figure 4.12. The plots were constructed using the best estimate of CT porosity (solid line, Figure 4.12). The upper plot shows a great improvement in the number of possible correlation locations, with 8 regions having likelihood values above 0.5. Within the CT interval (lower plot) the joint likelihood narrows the correlation locations to the region [8637.00ft, 8637.6ft].

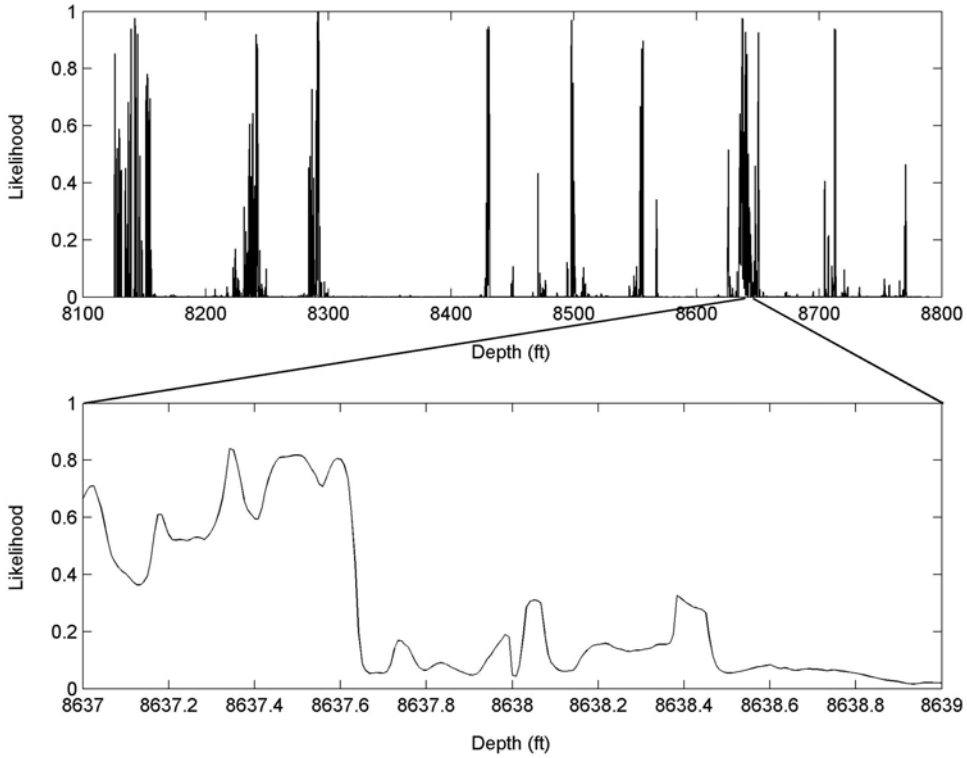

Figure 4.12 Comparison of CT and FMI mean and variance values using a joint likelihood function: (top) whole borehole; (bottom) CT interval.

To further improve the correlation the range statistic was added. The joint likelihood for mean, variance and range values is shown in Figure 4.13. The addition of the range to the likelihood has further constrained the number of possible correlations within the well, but at the expense of a drop in likelihood strength. Within the CT interval the addition has constrained the correlation to a single region between 8637.0ft and 8637.06ft.

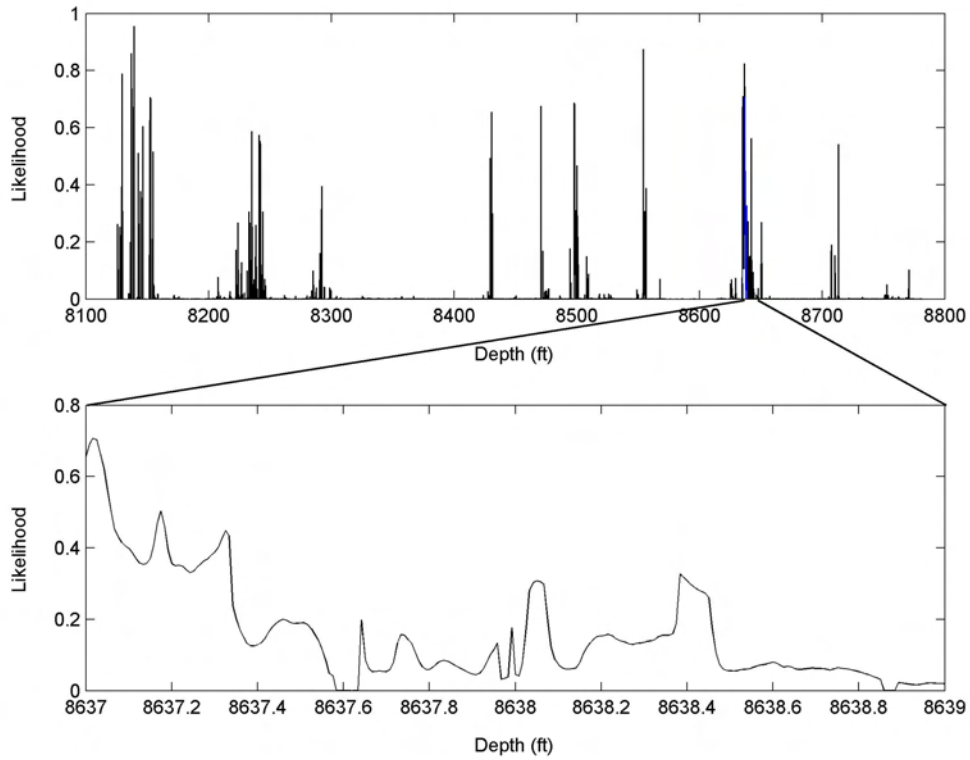

Figure 4.13 Comparison of CT and FMI mean, variance and range values using a joint likelihood function: (top) whole borehole; (bottom) CT interval.

It was hoped that skewness and kurtosis results could be added to the joint likelihood to further constrain the correlation. However there proved to be a mismatch between the FMI and CT data sets making these statistics unusable. For the averaged CT scan the Skewness was calculated as 0.338 and the Kurtosis as 1.139. These values fail to match any of the FMI values within the CT interval. The mismatch is attributed to the large sampling errors associated with these statistics as noted earlier. The lower plot in Figure 4.13 therefore represents our final state of information about the depth correlation of core and FMI data (since $P(x) \alpha J(x)$ within the CT interval and is zero otherwise)

4.6 Discussion

This method has been demonstrated using the mean, variance and the range parameter as these statistics were shown to have some predictive power within the data sets. However the method could be applied to any combination of statistics, and hence be applied to many different correlation problems.

There are a number of sources of uncertainty with the study. These mainly result from aspects of the data processing either in the choice of maximum CT value, or estimation of the range parameter.

4.6.1 Difference in Measurement Conditions

The FMI data was measured at a depth of around 8600ft and hence at considerable pressure. In contrast, the CT scan was carried out at the earth's surface at atmospheric pressure. It is possible that the core sample underwent decompression as it was brought to the surface, changing its porosity. To test the magnitude of this effect the change in dimensions between a standard limestone at depth and at the Earth's surface was calculated using Young's Modulus (Davis and Reynolds, 1996): $E = PL/\Delta L$ where P is pressure, L is length and ΔL is length change. The density of limestone was taken to be 2611 kg/m^3 (personal communication, S. Elphick 2006) and the overlying rocks were all assumed to have a similar density. The value of pressure at 8600ft was then estimated at 67.8 MPa. Using a value of 53 GPa for Young's Modulus in limestone, the ratio ΔL to L is calculated to be 0.0013 or 0.13%. Therefore decompression can be discounted as a major source of error.

4.6.2 Error in Maximum CT value

Another potential source of error is the conversion of CT values to porosity estimates. The key to the conversion process was finding a CT value representing a carbonate voxel with zero porosity. The maximum CT value in the core section was 150, but this was shown to correspond to non-carbonate features, probably pyrite. To ensure the maximum value represented a carbonate voxel, a fragment of outer rudist shell was chosen as these are known from scanning electron microscopy to have little porosity. The resulting maximum CT value was 144 ± 2. The range in the joint

mean, variance and range likelihood corresponding to the choice of maximum CT value is shown in Figure 4.14.

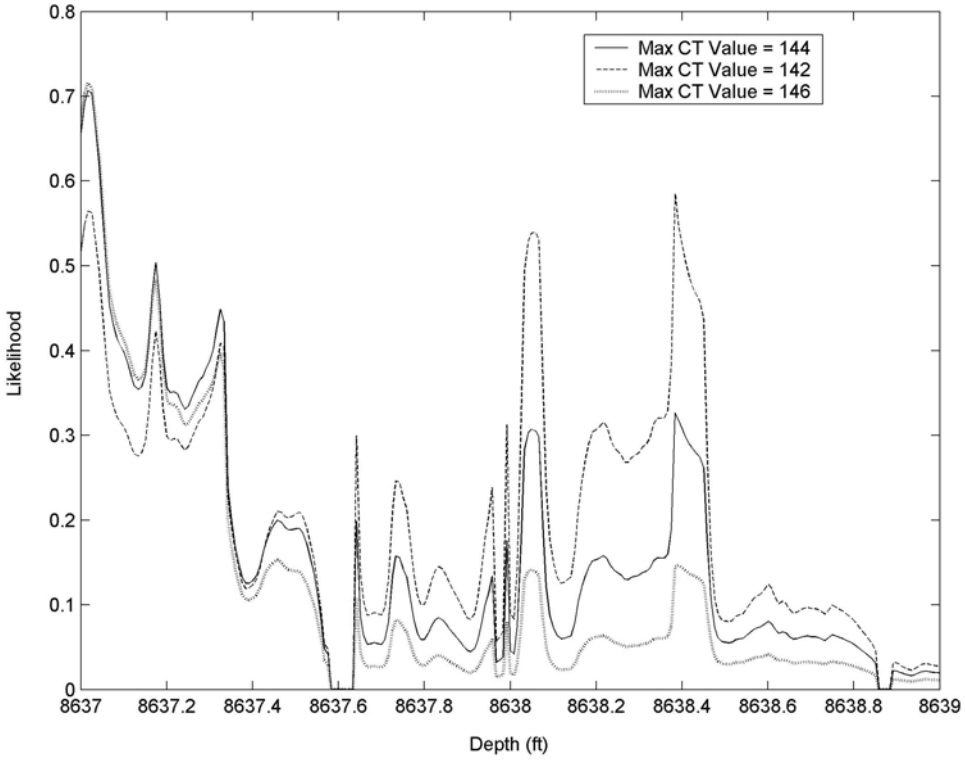

Figure 4.14 Range of joint mean, variance and range likelihood values caused by choice of maximum CT value.

The single strong correlation (likelihood above 0.5), found around 8637.0ft (Figure 4.13), is replicated for both the upper (dotted line, Figure 4.14) and lower (dashed line, Figure 4.14) maximum CT values. The lower bound also produces two strong correlations around 8638.0ft and 8638.4ft. The insensitivity of the correlation around 8637.0ft, to the choice of maximum CT value, makes this the most likely correlation location. The other peaks only appear for extreme values of maximum CT value.

4.6.3 Error in Range Estimate

Another source of error lies in the estimation of the range parameter from variograms. In an attempt to quantify this error an upper and lower bound was also estimated.

The effect of using the extreme values for the range within the joint likelihood of the mean, variance and range are shown in Figure 4.15 for the CT range and Figure 4.16 for the FMI ranges.

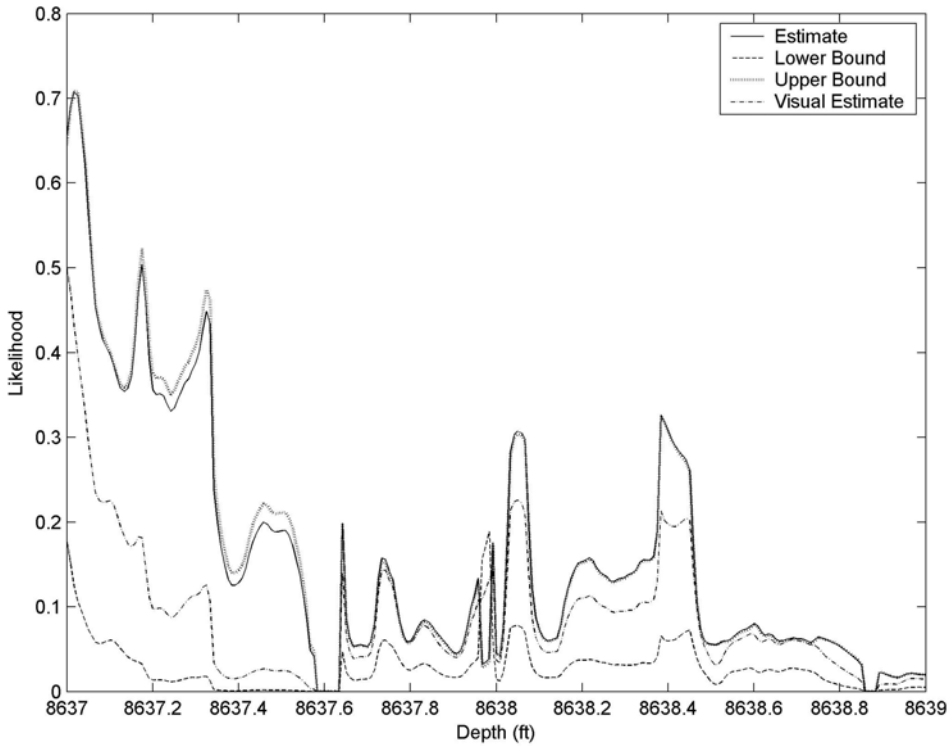

Figure 4.15 Range of joint mean, variance and range likelihood values caused by estimation of CT range value.

For the CT range values (Figure 4.15) the upper bound (dotted) agrees well with the estimated value. This is to be expected given the similarity between the range values. The lower bound (dashed) is significantly different, with no strong correlations. The difference in behaviour is due to the shape of the variogram (Figure 4.10). The sill does not flatten out completely and so the range estimate and upper bound are similar. The lower bound is much smaller and lies close to the point where the variogram starts to flatten out. Visual inspection of the CT variogram would suggest that the range actually lies midway between the calculated estimate and lower bound at 0.85". A joint likelihood was calculated using this value (Figure 4.15, dash-dot line). This

plots between the estimate and lower bound curves but importantly has its strongest values around 8637ft, consistent with the calculated estimate.

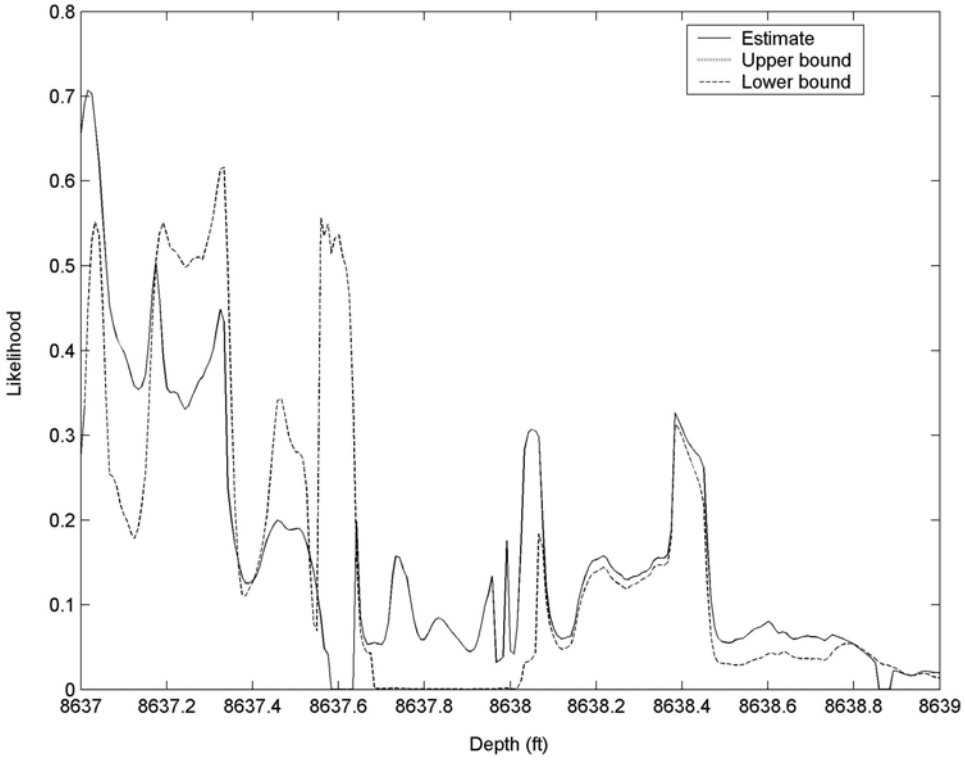

Figure 4.16 Range of joint mean, variance and range likelihood values caused by estimation of FMI range values.

For the FMI range values (Figure 4.16) the upper bound (dotted line) is almost zero for the entire interval. The lower bound (dashed line) produces a number of strong correlations, one of which matches the best range estimate around 8637.0ft. The other strong locations only occur when using the extreme lower range value.
The likelihood plots using the extreme range values show that the choice of range value is critical. However in the correlation method uses the same algorithm to determine the range value for each variogram and therefore any bias or procedural error should be the same for each result. The results may be improved subjectively by visual inspection of each variogram, but this approach would greatly increase the time required to apply the method due to the enormous number of variograms considered.

4.7 Conclusions

A method has been proposed to constrain the correlation of geophysical logs with extracted core. A number of statistics are calculated for each data set and an entropy- based measure has been proposed in order to find the most informative combination of these. Then the individual statistical correlations are combined using a joint likelihood function, and these are combined with any other prior information using a Bayesian methodology. The method has been demonstrated using FMI logs and X-ray CT scans of extracted core. The use of the mean and variance statistics proved successful in constraining the depth of the FMI data relative to the CT data but failed to produce a unique depth range. Calculated higher order conventional statistics proved unmatchable between the two data sets. A geostatistical approach using the range parameter from variograms constrained the correlation to a single depth interval of 0.06ft = 0.72" (18.29mm), or 7 possible FMI window positions, allowing for the subsequent development of interpretation techniques requiring accurate core-log correlation.

Chapter 5 - Application of Correlation Methodology

5.1 Introduction

The correlation methodology developed in the previous chapter was applied to a second core section. The second core section came from the 8121ft region of the same well as the core section used in chapter 4. The extracted core was again scanned with X-rays to produce a 3D tomogram based on X-ray attenuation. Log data was available in the region in the form of resistivity data from a Fullbore MicroImager (FMI). As before the aim was to improve the correlation between these two data sets from the 2ft interval provided by conventional depth matching methods.

The same processing methodology as used previously was applied to the data sets, with the CT data being averaged to FMI resolution and both data sets being converted to porosity estimates. The application of the correlation method resulted in a decrease in the correlation uncertainty from 2ft down to two possible locations, each 0.15ft in length.

5.2 Core Description

The second core section was extracted from the same Middle Eastern borehole as the first but 500ft nearer the surface at 8121ft. It is still from the Cretaceous Shu' aiba formation deposited on a platform at the edge of the Tethys ocean (Konert et al., 2001). The core section is 165mm in length and is made up of rudist rudstone, with the dominant features being rudist shells up to 1" in diameter. The core was scanned using X-ray CT to produce a 3D volume with cubic voxels with a length scale of 0.125mm.

The associated log data was again taken from the FMI resistivity tool. As in described in chapter 3, the data had already been converted to porosity estimates using the method outlined in Tilke et al (2006). As with the first core section, there are no large scale features which would allow a direct correlation to be made between the two data sets, due to the 2" annulus of rock lost during the coring process.

5.3 Data Processing

The CT data processing followed the same procedure as for the first core. A 'beam hardening' correction was applied using a second order polynomial to remove the gradient in CT values between the centre and the edge of the volume. After the correction was applied a number of anomalously high CT values were observed in the centre of the core (Figure 5.1, light voxels around 3.5 inches down within box). The regular shape and association of these high values with shell fragments suggests that they are due to the presence of pyrite rhomboids. Therefore the conversion from CT value to porosity was carried out using the maximum CT value for a purely carbonate voxel. The CT value used was 150, which correlates with fragments of assumed-zero porosity rudist shell. The CT scan was then averaged to the same resolution as the FMI. Given the different CT resolution (0.125mm opposed to 0.165mm) of the second CT scan, the kernel used in the averaging process was changed to be 41*41*41 voxels in size. The final averaged volume was the same size as the averaged volume used in the correlation of the first core section.

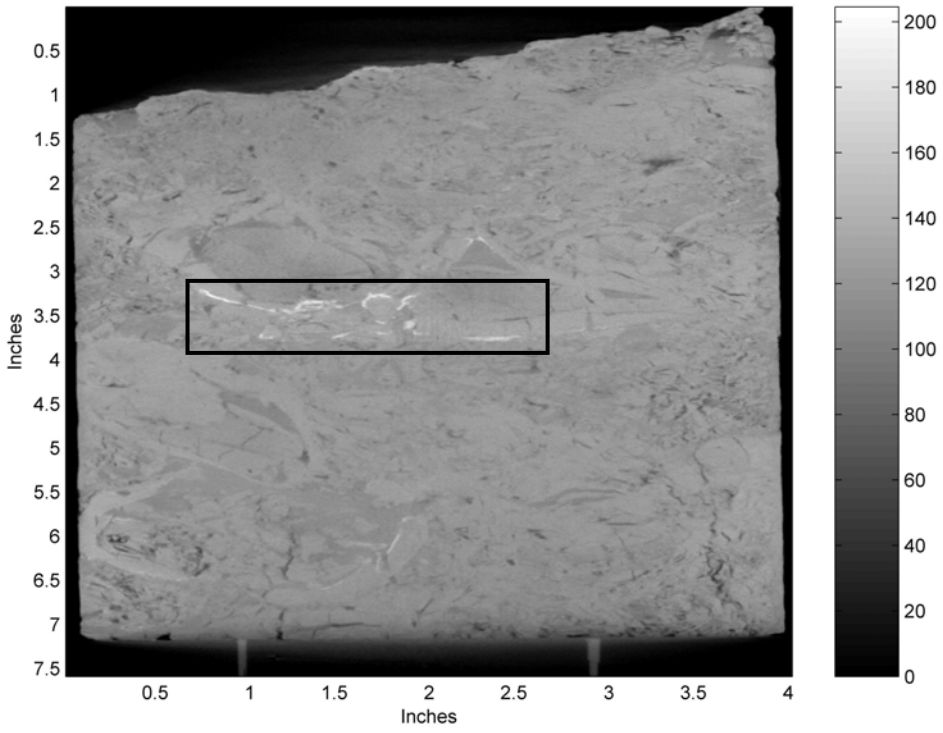

Figure 5.1. Vertical slice through the centre of the CT tomogram after the 'beam hardening' correction had been applied. The high CT values around 3.5 inches down (within box) are due to the presence of pyrite.

5.4 Entropy Analysis

Since the averaged core sections here and from the previous chapter are of the same size, the statistics calculated, in Chapter 4, for core sized windows of the FMI data could be used unchanged. As with the correlation of the first section of core, the most appropriate order for combining the statistics was determined using FMI data alone. For each statistics a set of likelihood functions were calculated to compare each window within the CT interval against the rest of the borehole. The amount of differentiation information contained within each of the likelihood functions was determined by calculating its entropy. The entropy results for each of the individual statistics are shown in Figure 5.2.

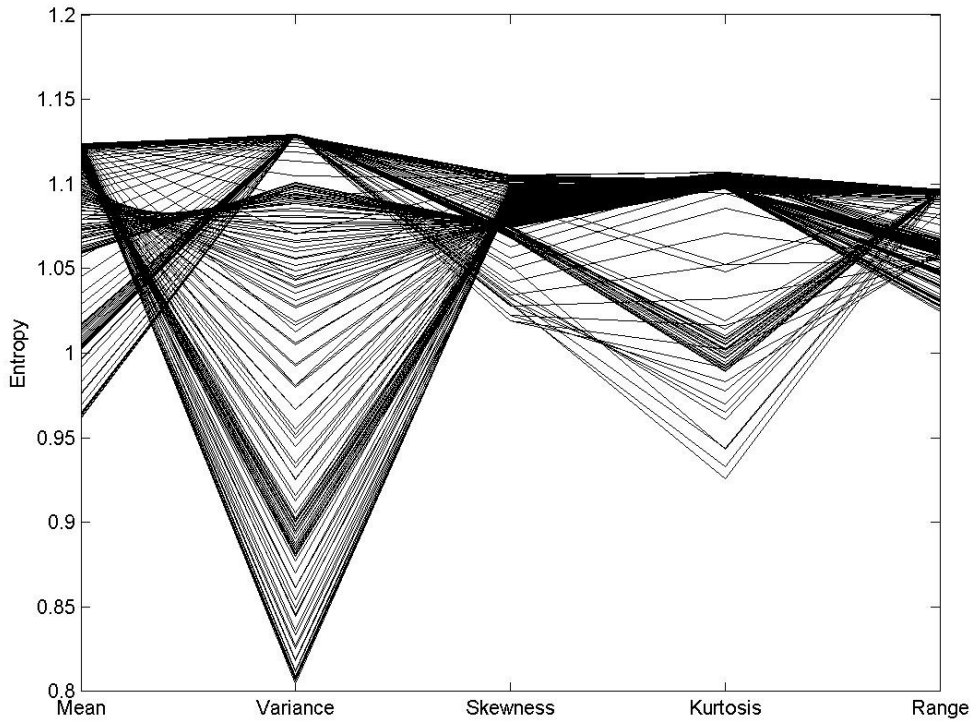

Figure 5.2. The entropy for each of the likelihood functions comparing the core-sized windows within the CT interval and the rest of the core, calculated for each statistic.

Low entropy values indicate functions containing more differentiation information than those with high entropy values. Hence Figure 5.2 shows that, as previously, on average the variance contains the most differentiation information. However the remaining statistics contain similar amounts of information. The entropy results for different combinations of statistics, averaged across all windows within the CT interval, are shown in Figure 5.3.

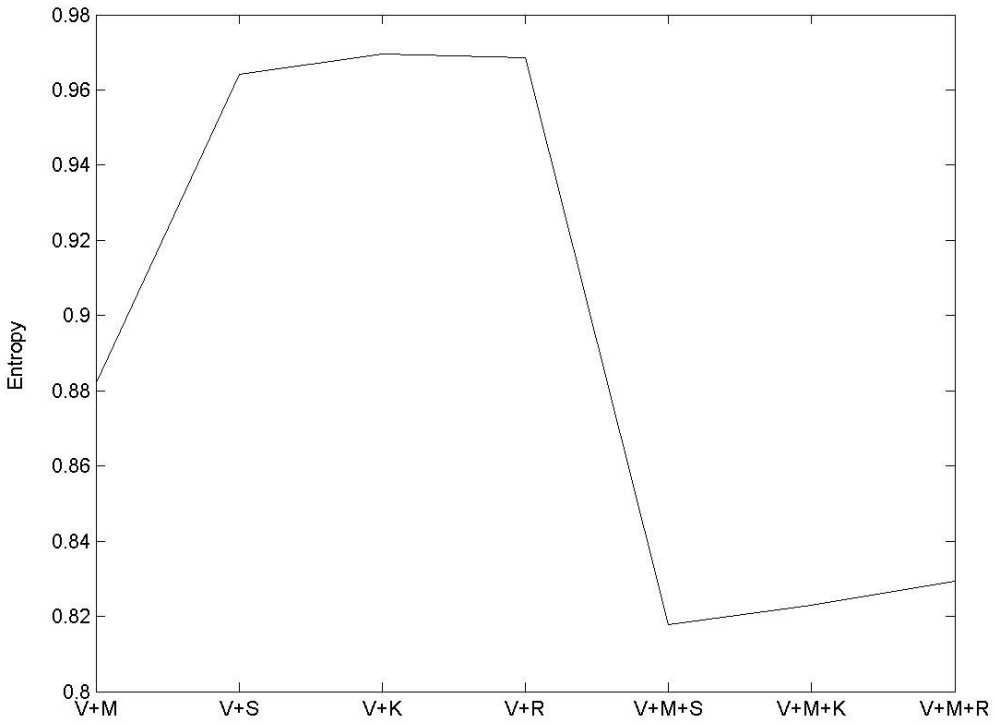

Figure 5.3. The entropy for each of the likelihood functions comparing the windows within the CT interval and the rest of the core, calculated for different combinations of statistics (V=variance, M=mean, S=skewness, K=kurtosis, R=range).

The results in Figure 5.3 show that the most information, when using two statistics, is provided by the mean and variance. When using three statistics the addition of the skewness provides the most information.

5.5 CT Results

The values for the different statistical techniques, calculated from the averaged CT volume are given in Table 5.1. The values in the Estimate, Upper and Lower bound columns were calculated using porosity values derived using a CT maximum value of 150, 152 and 148 respectively. There are no skewness or kurtosis values in the Upper or Lower Bound columns. Both of these techniques describe aspects of the shape of the distribution that are unaffected by the choice of CT maximum.

Table 5.1. Statistical results describing the averaged CT data.

	Estimate	Upper Bound	Lower Bound
Mean	0.190	0.200	0.179
Variance	0.001	0.001	0.001
Skewness	0.877	-	-
Kurtosis	10.572	-	-
Range	1.201	1.275	0.574

5.6 Likelihood functions

The statistics calculated from the averaged CT data and core sized windows of FMI data were compared using a likelihood function. The entropy results (Figure 5.2) show that the variance has the most differentiation information for a single statistic. The likelihood function of the relative location of the core within the FMI log found by comparing only the variance values is shown in Figure 5.4. The plot shows that there are strong likelihood values (>0.5) over much of the length of the borehole. However, within the CT interval there is a clear differentiation between the upper and lower sections with strong likelihood values only being found in the lower section between 8134.3ft and 8135.25ft. These suggest that the core was extracted from somewhere within this region.

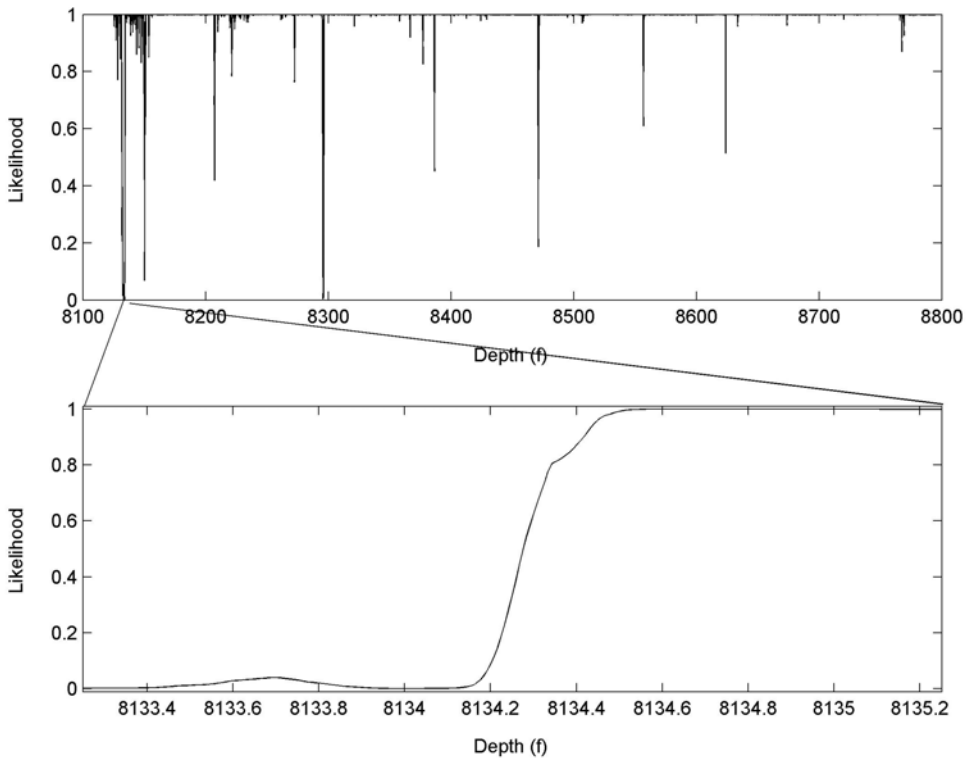

Figure 5.4. Likelihood function comparing the variance values of the CT and core sized windows of FMI data: (top) whole borehole; (bottom) CT interval.

When using two statistics, the combination of the variance and the mean was shown to provide the most information. Therefore the joint mean and variance likelihood function was calculated and shown in Figure 5.5. The function again has strong values in the lower section of the CT interval but with the strongest values occurring in the region between 8134.4ft and 8135ft.

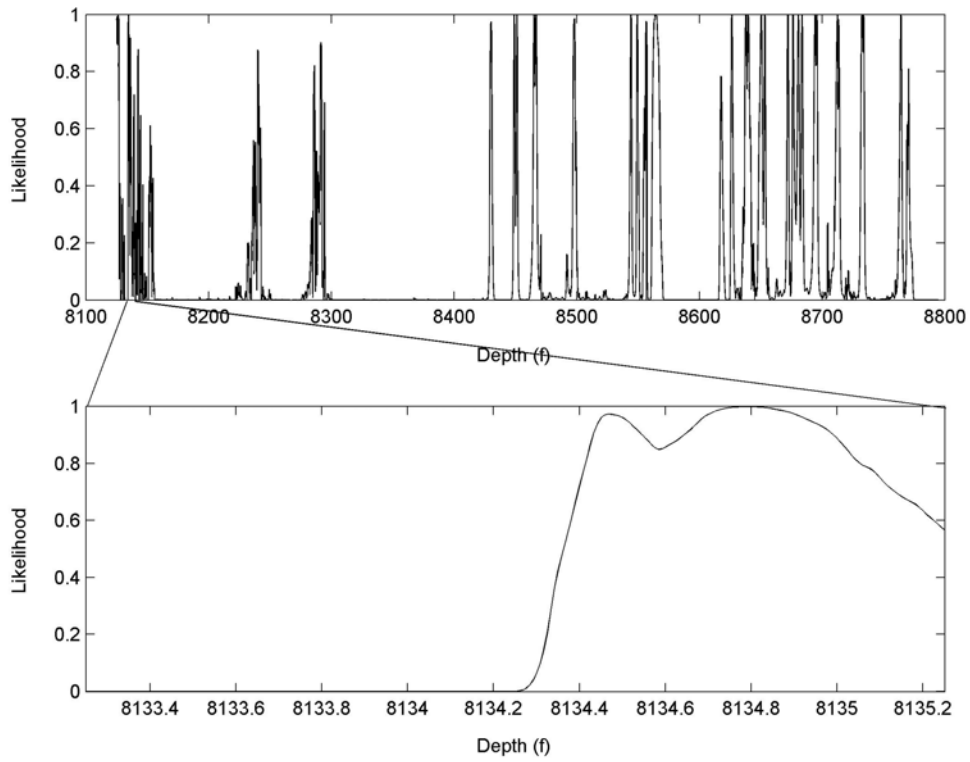

Figure 5.5. Joint likelihood function comparing the variance and mean values of the CT and core sized windows of FMI data: (top) whole borehole; (bottom) CT interval.

To further improve the correlation a third statistic was added to the joint likelihood. The entropy results show that the skewness, followed by the kurtosis, would provide the most differentiation information. However the joint likelihood functions calculated using these statistics show very weak likelihood values (<0.01) throughout the CT interval. A mismatch in these statistics was observed between the FMI and the first section of CT data, which was attributed to the magnification of errors during their calculation. Therefore, as in the previous chapter, it was decided to ignore these statistics and use the range parameter instead.

The joint variance, mean and range likelihood function is shown in Figure 5.6. The results show strong likelihood values in the regions between 8134.4 ft and 8134.55ft and 8135.1ft and 8135.25ft. However there is a single very strong peak (0.95) at 8134.5ft. This is the most likely position from which the core was extracted.

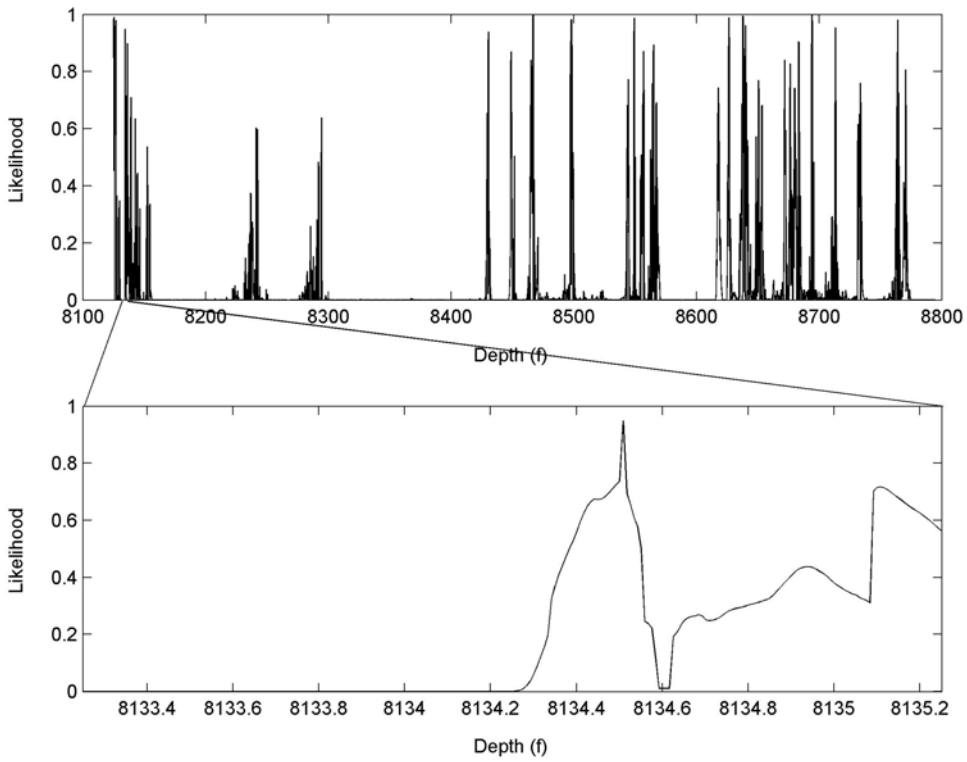

Figure 5.6. Joint likelihood function comparing the variance, mean and range values of the CT and core sized windows of FMI data: (top) whole borehole; (bottom) CT interval.

5.7 Discussion

5.7.1 Error in Maximum CT

As with the first core section a potential source of error lies in the choice of the CT value used to represent solid carbonate. The CT value was chosen by selecting the voxel with the maximum value which correlates with shell fragments which are known to have little porosity. The chosen value was found to be 150 ± 2. The change in the joint variance, mean and range likelihood caused by the choice of maximum CT value is shown in Figure 5.7.

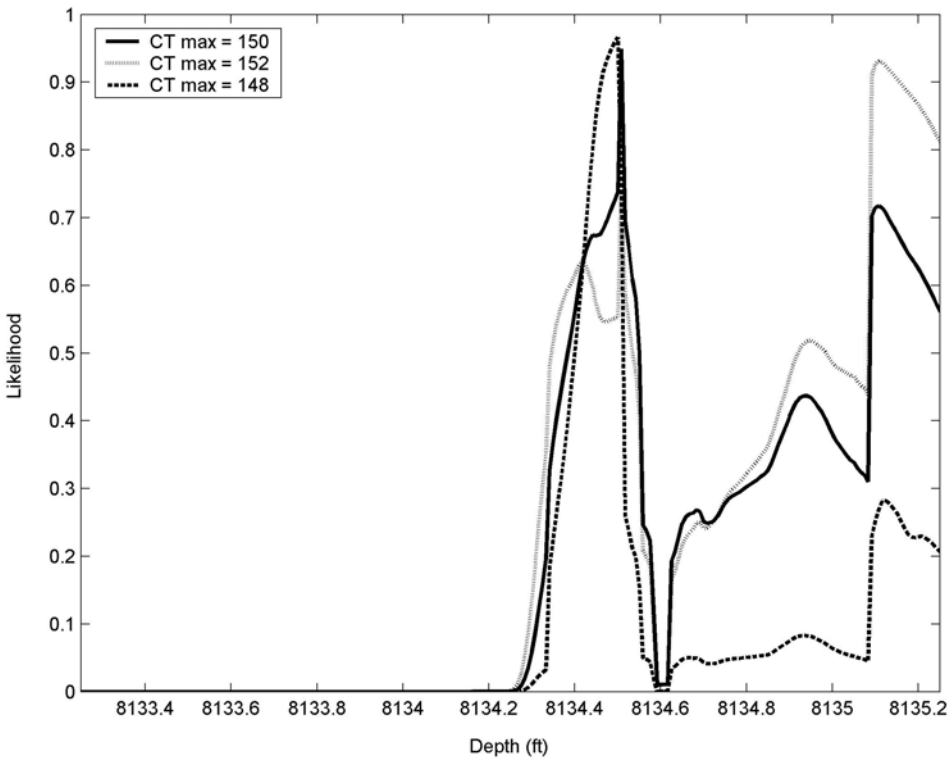

Figure 5.7. The changes in the joint variance, mean, and range likelihood values caused by the choice of maximum CT value.

The different likelihood values all follow a similar pattern with peaks in the same regions but show changes in amplitude. The single strong peak observed in Figure 5.7 at 8134.5ft broadened for the lower maximum CT value (Figure 5.7, dashed line) and the peak between 8135.1ft and 8135.25ft is greatly reduced. The upper maximum CT value (Figure 5.7, dotted line) has similar amplitude values between 8134.4 ft and 8134.55ft but lacks the spike at 8134.5ft. The peak between 8135.1ft and 8135.25ft is however greatly increased, to above 0.9 at its peak, using the upper value.

5.7.2 Error in Range Estimate

Another source of error is estimation of the range parameter from variograms. Upper and lower bounds on the estimates were calculated and the resulting effect on the joint variance, mean and range likelihood values are shown in Figures 5.8 and 5.9.

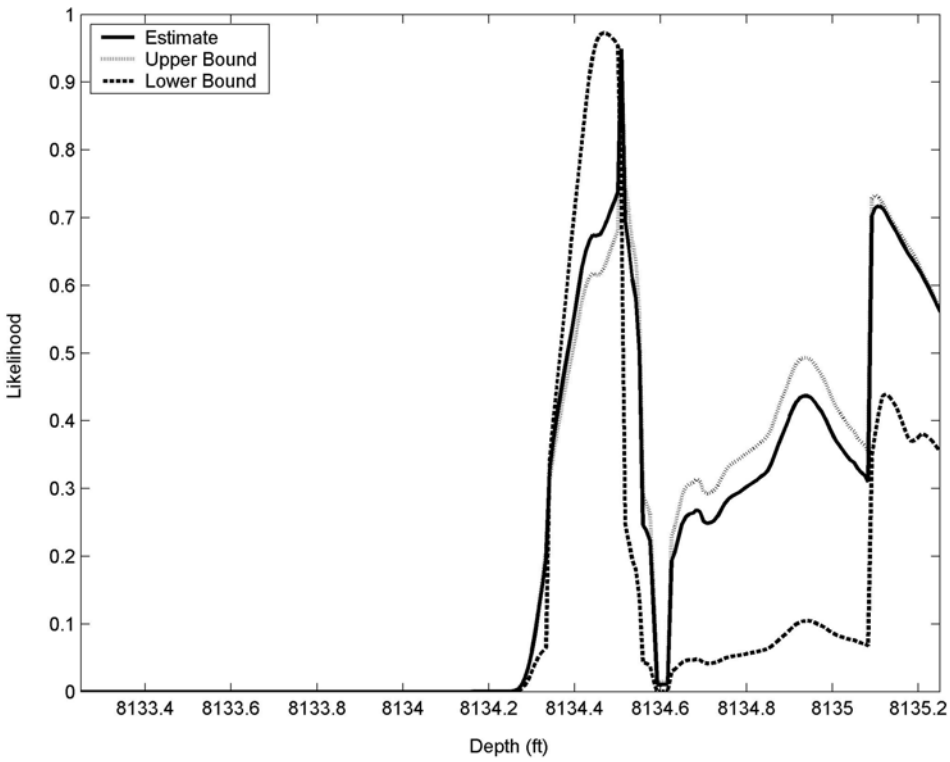

Figure 5.8. The range of joint variance, mean, and range likelihood values caused by the estimation of the range from the variogram of the CT data.

The upper (Figure 5.8, dotted line) and lower (dashed line) range values estimated from the CT data agree well with the estimated (solid line) values. The upper bound in particular closely mirrors the estimated values. The lower bound values have a broader maximum peak than the estimated values between 8134.4 ft and 8134.55ft. The peak between 8135.1ft and 8135.25ft is however much reduced.

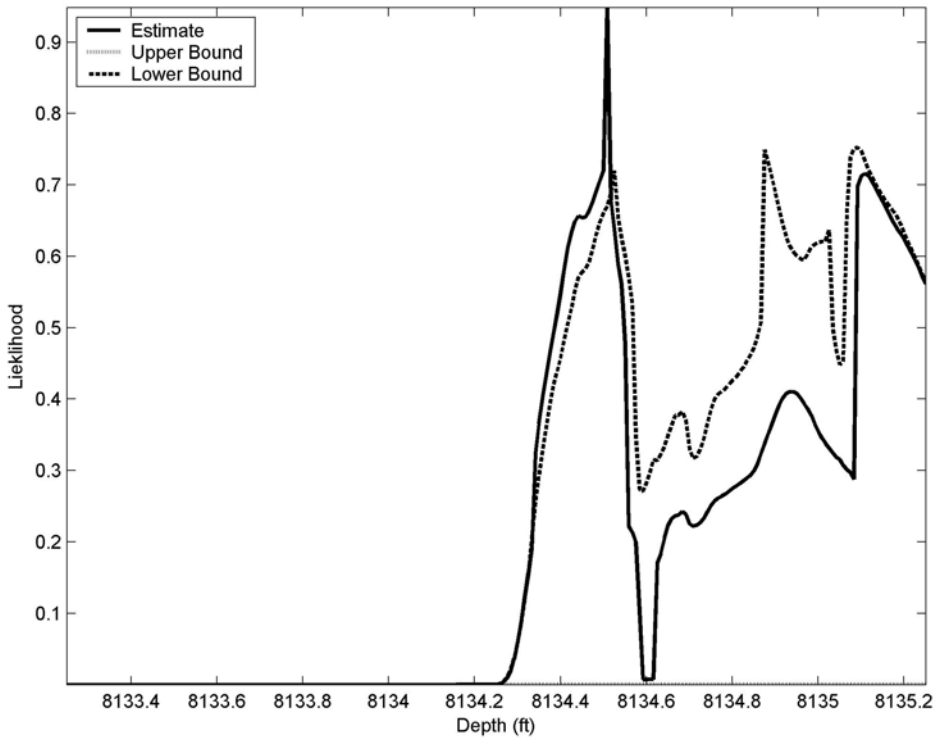

Figure 5.9. The range of joint variance, mean, and range likelihood values caused by the estimation of the range from the variograms of the FMI data.

For the FMI range values (Figure 5.9) the upper bound (dotted line) is almost zero for the entire interval. The lower bound (dashed line) is similar to the estimated values but has a new strong correlation between 8134.85ft and 8135ft.

5.7.3 Comparison with first core section correlation

The correlation results for the second core section are not as precise as those for the first section as they give two possible correlation regions. They do however greatly improve upon the correlation obtained using conventional methods. The presence of two peaks indicates that there are two regions within the 2ft section which have similar mean, variance and range statistics. The inclusion of additional statistics to the likelihood function might eventually discriminate between the two peaks.

However the addition of statistics would also increase the amount of error contained within the likelihood function. This would lead to a decrease in the amplitude of the

likelihood peaks observed making correct correlation harder to determine. The key to the successful application of this correlation technique is to identify a small number of statistical techniques which have most predictive power.

5.8 Conclusion

The application of the statistical correlation technique to an X-ray CT scanned section of core and a corresponding section of resistivity data measured from the borehole wall resulted in two strong correlation locations in the regions between 8134.4 ft and 8134.55ft and 8135.1ft and 8135.25ft. The strongest peak (0.95) was found at 8134.5ft. This is the most likely position from which the core was extracted.

Chapter 6 – Up-Scaling

6.1 Introduction

In chapters 4 and 5 a method for the accurate statistical correlation of extracted core to measurements from wireline logging tools has been set out and applied. The creation of such a correlation allows the development of statistical up- and down-scaling relationships between the high resolution core data and the lower resolution logging data. The down-scaling relationships could then in principle be applied in regions of the borehole with logging data but without core samples to provide a statistical constraint on the range of high resolution structures consistent with the lower resolution logging data (Figure 1.1).

The creation of down-scaling relations can be considered as an inverse problem: in order to achieve it, we first have to understand the far simpler 'forward' problem of up-scaling, in this case using variogram scaling laws. In this thesis I will not get on to down-scaling, but will create a foundation for it by studying the up-scaling relationship.

As in chapters 4 and 5 the high resolution core data is taken from a CT scan of extracted core and the low resolution logging data is taken from the FMI resistivity tool. In previous chapters the CT data was averaged prior to statistics being calculated and compared with those from the FMI data. In this chapter, for the first time, statistics calculated at multiple scales are compared.

Two comparisons are made in this chapter. Firstly, the validity of applying variogram up-scaling theory to the CT data is tested. This is carried out by comparing up-scaled variograms, calculated using the original CT data, with those calculated after averaging of the CT data. Secondly a comparison is made between up-scaled CT variograms and those calculated from FMI data.

6.2 Background

In geological investigations the gathered data often spans a range of different scales (e.g. core plugs, well logs, seismic, etc). This is a particular problem for mining engineers trying to determine the grade of a mineral reserve from diverse data sources. To solve the problem, scaling laws were developed for the variogram, the standard spatial statistic used in mining (Matheron, 1963; Journal and Huijbregts, 2003). Though initially developed for the mining industry the use of variograms, or geostatistics, has spread into many other areas of study including the oil industry (Hohn and Neal, 1986), hydrology (Kitandis, 1997) and remote sensing (Curran and Atkinson, 1998). The scaling laws are therefore useful tools for a variety of areas of study.

6.3 Scaling Laws

The following description of variogram scaling has been adapted from Clark (1979), Frykman and Deutsch (1999), Journel and Huijbregts (2003) and Tilke et al (2006).

The variogram scaling laws are conventionally defined using the exponential variogram model:

$$\gamma(h) = C_0 + C_1\left(1 - e^{-\frac{h}{L_1}}\right) \qquad \ldots(6.1)$$

where $\gamma(h)$ is the model variance at lag h, C_0 is the nugget effect, C_1 the sill, and L_1 is the range.

Now consider two finite volumes, v (measurement volume of the original CT volume) and V (measurement volume of the averaged CT volume), with $v < V$. These are measurement volumes: each measurement in the original CT data is an average over the volume v, and each measurement in the averaged CT data is an average over the volume V. The variogram scaling laws can then be used to derive the variogram parameters for V ($C_{0,V}$, $C_{1,V}$, and $L_{1,V}$) from the parameters for v ($C_{0,v}$, $C_{1,v}$, and $L_{1,v}$) as follows:

The nugget effect can be up-scaled using the relation:

$$C_{0,V} = C_{0,v}\frac{v}{V} \qquad \ldots(6.2)$$

The range can be up-scaled using the relation:

$$L_{1,V} = L_{1,v} + \left(|V| - |v|\right) \qquad \ldots(6.3)$$

where $|V|$ and $|v|$ are the dimensions, or lengths, of the volumes V and v, in the direction in which the variogram is measured. In this chapter the variograms are always measured parallel to the sides of the volumes and so $|V|$ and $|v|$ are $\sqrt[3]{V}$ and $\sqrt[3]{v}$ respectively.

To upscale the sill requires the concept of a point scale sill C_p. This is the sill which would be calculated if the area of interest was divided into infinitely small volumes creating a data set of point measurements with no averaging. Then the decrease in the sill for the volume v, is:

$$C_p - C_v = C_p\overline{\Gamma_v} \qquad \ldots(6.4)$$

where $C_p\overline{\Gamma_v}$ is the point scale sill within the volume v, and $\overline{\Gamma_v}$ is the normalised point scale sill in v, which is calculated using the double integral:

$$\overline{\Gamma_v} = \frac{1}{v^2}\iint_{vv}\Gamma_p\left(|a-b|\right)dadb \qquad \ldots(6.5)$$

where $|a-b|$ is the Euclidean distance between all pairs of points a and b within the volume v. Γ_p is the full normalised (has maximum value 1) point scale model semi-variogram expressed as:

$$\Gamma_p\left(|a-b|\right) = 1 - e^{-\frac{|a-b|}{L_{1,v}-|v|}} \quad \ldots(6.6)$$

where $L_{1,v} - |v|$ is the modelled point scale range by equation 6.3 applied to the volume v and the infinitesimal point volume.

Similarly to equation 6.4 the decrease in sill for the volume V is:

$$C_p - C_V = C_p \overline{\Gamma_V} \quad \ldots(6.7)$$

where $\overline{\Gamma_V}$ is given by:

$$\overline{\Gamma_V} = \frac{1}{V^2} \iint_{VV} \Gamma_p\left(|a-b|\right) da db \quad \ldots(6.8)$$

Equations 6.4 and 6.7 can be combined to eliminate the point scale sill C_p and give C_V:

$$C_V = C_v \frac{1-\overline{\Gamma_V}}{1-\overline{\Gamma_v}} \quad \ldots(6.9)$$

6.4 Validation of Code

A section of code was developed in Matlab (MathWorks, 2002) which numerically evaluated the double integrals involved in equations 6.5 and 6.8. To ensure the stability of the integration the size of the integration intervals *da* and *db* were steadily decreased until the integration result became stable. This approach minimises any uncertainty introduced through the use of numerical integration. The code was validated using data from Frykman and Deutsch (1999) and the results proved to be in good agreement.

6.5 Data

The FMI and CT data sets used in previous chapters have different measurement scales. Before the correlation method could be applied, the CT data, (with resolutions of 0.0064" and 0.0049"), was up-scaled to the FMI resolution of 0.1". The up-scaling was carried out using a kernel of Gaussian distributed weights. The averaged data was taken as the sum of products of the kernel and the CT data.

The scaling validation was applied to both sets of extracted core CT scans. Variograms were calculated for each CT scan using the original data and the averaged data. Like the CT variogram calculated in chapter 4 the variograms were calculated using horizontal slices. However the 8626ft core scan had $631 \times 631 \times 813$ voxels while the 8121ft section had $823 \times 823 \times 1542$ voxels. These large data sets made the calculation of a 2D variogram impractical due to the large number of data pairs. Instead a rectangular section was extracted from each horizontal slice of the scan. Two variograms were then calculated for the two directions parallel to the sides of the rectangle. These directions were termed horizontal and vertical and are shown in Figure 6.1.

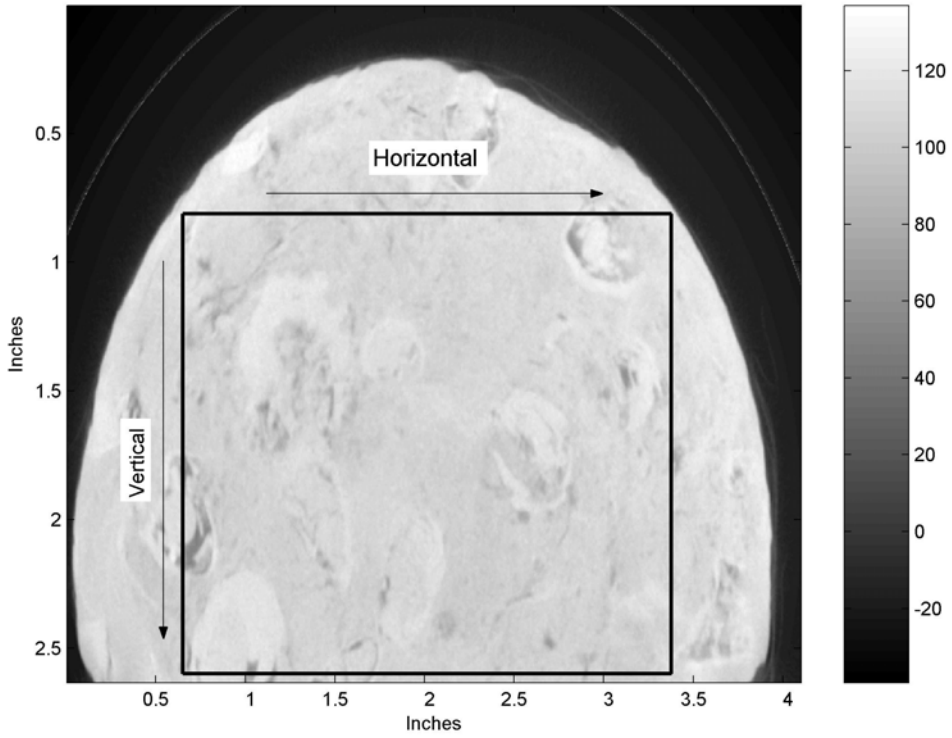

Figure 6.1. A horizontal slice of original scale CT scanned extracted core. Box marks the region used to calculate variograms with the direction labels, horizontal and vertical, marked.

A similar approach was used to calculate the variograms from the averaged CT data. The same rectangular section was extracted from each horizontal slice of the averaged CT scan. Variograms were then calculated in the same directions as for the original data.

6.6 Variogram Scaling using CT Data

6.6.1 8626ft Core Section

The calculated variograms from the original and averaged CT data are shown in Figure 6.2.

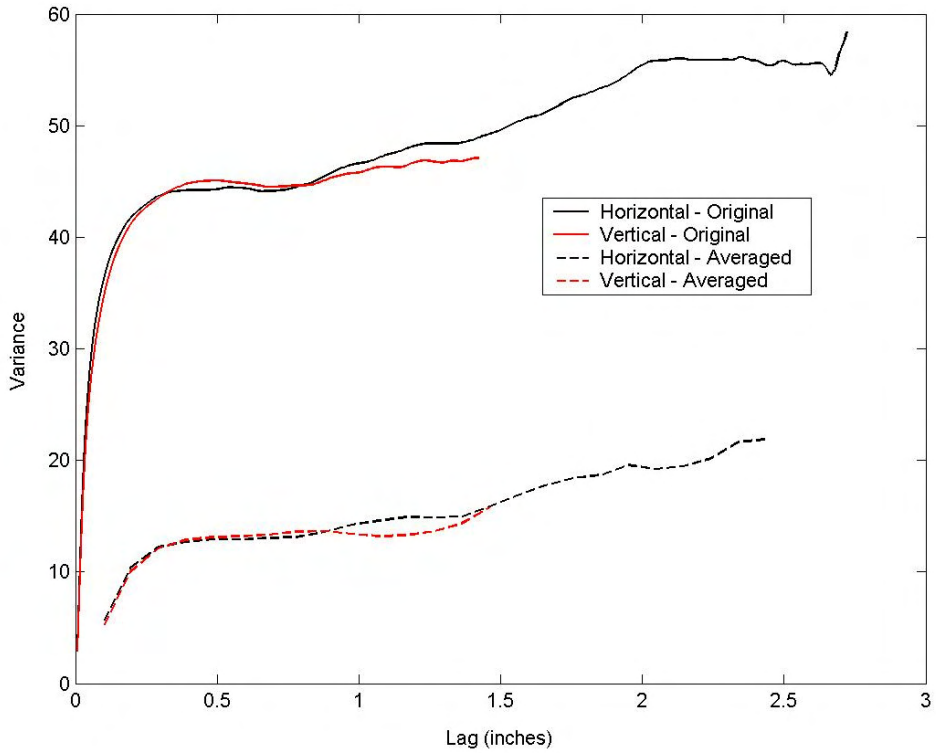

Figure 6.2. The variograms calculated from the 8626ft section of core. Variograms calculated using the original data is shown with a solid line while those calculated from the averaged data is shown with a dashed line.

For each data set the variograms in each direction are very similar. They have consistent range (the distance at which the variogram levels off) and sill values (the variance at which the variogram levels off). However between the data sets there is a large change in the sill value. It drops from a value of 44 for the original data down to a value of 13 for the averaged data. This drop is to be expected as any averaging process removes a degree of variability. The range value has changed little, increasing from 0.4" for the original data, to 0.45 for the averaged data.

The up-scaled range was calculated using equation 6.3. The original CT measurement scale, v, was 0.0065". The averaged CT data measurement scale, V, was 0.1". This gave a predicted up-scaled range of 0.49". This is very close to that observed from the averaged data.

To calculate the up-scaled sill required the evaluation of the terms $\overline{\Gamma_v}$ and $\overline{\Gamma_V}$ from equations 6.5 and 6.8 respectively. The terms were evaluated using numerical integration to give $\overline{\Gamma_v} = 0.414 \times 10^{-3}$ and $\overline{\Gamma}_V = 0.0916$. These values gave an up-scaled sill value of 40. This value is far larger than the value of 13 observed for the averaged data variogram. A summary of the results is given in Table 6.1.

Table 6.1. Variogram parameters calculated from the CT scan of core section 8626ft.

	Range (inches)	**Sill**
Original Data	0.4	44
Predicted Up-scaled Data	0.49	40
Averaged Data	0.4	13

6.6.2 8121ft Core Section

The calculated variograms from the original and averaged CT data are shown in Figure 6.3.

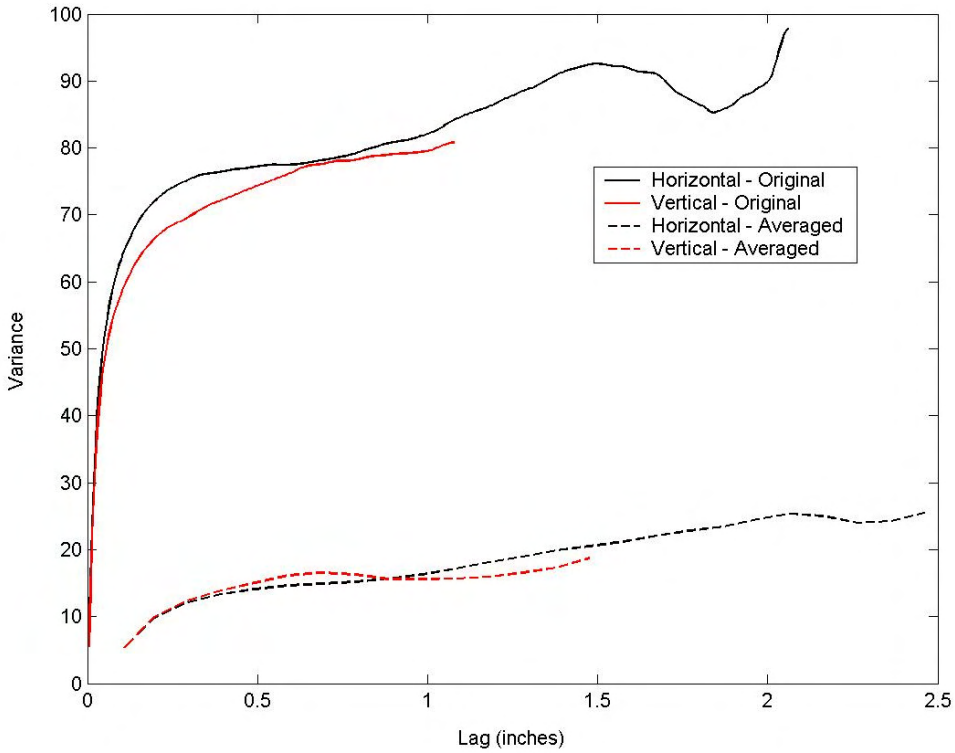

Figure 6.3. The variograms calculated from the 8121ft section of core. Variograms calculated using the original data is shown with a solid line while those calculated from the averaged data is shown with a dashed line.

As with the 8626ft core section the directional variograms are similar in magnitude. However those calculated from the original data show a difference in shape. The vertical direction variogram starts to flatten off before the horizontal variogram at around 0.05". There is then a change of slope around 0.24" before reaching a plateau, of 77, at around 0.65". The change of slope suggests that there are two or more spatial scales which interact to create this complicated behaviour. The horizontal variogram reaches a plateau of 77, at around 0.55" and beyond this its behaviour also becomes more complex. To simplify the scaling algorithm, only the horizontal variogram with a range of 0.55" and a sill of 77 was used in the test.

The variograms calculated using the averaged data are also shown in Figure 6.3 and are far more consistent. They both rise up to a sill of 13 at a range of 0.6". They also exhibit more complex behaviour beyond a lag of 0.8".

The up-scaled range was again calculated using equation 6.3, with original CT measurement scale, $v = 0.0049$" and the averaged CT scale, $V = 0.1$". This gave a predicted up-scaled range of 0.645". The predicted range value is slightly larger than that observed using the averaged data.

Again numerical integration was used to evaluate the terms required for the up-scaled sill calculation as, $\overline{\Gamma_v} = 0.123 \times 10^{-3}$ and $\overline{\Gamma}_V = 0.0488$. These values give a predicted value for the up-scaled sill as 73. As with the first core section this is far larger than the 13 observed from the averaged variogram. A summary of the results is shown in Table 6.2.

Table 6.2. Variogram parameters calculated from the CT scan of core section 8121ft

	Range (inches)	**Sill**
Original Data	0.55	77
Predicted Up-scaled Data	0.645	73
Averaged Data	0.60	13

6.6.3 Discussion of Variogram Scaling

If the assumptions underlying the up-scaling theory are valid, the application of the up-scaling theory to the CT data sets should produce consistent results as the only change in the data has been the application of the averaging process. The comparison of the range parameter shows good agreement in the 8626ft core section. In the 8121ft core section there is a difference of 0.045" between the up-scaled and averaged values. This is a relatively small difference and maybe explained by the uncertainties introduced by estimating the range value on a shallow slope. However, the comparison of sill values shows considerable differences for both core sections.

There are a number of possible reasons for the difference in sill values observed. Firstly the choice of an exponential variogram model for the variograms may not be appropriate. All the variograms calculated show complicated behaviour after the first break of slope. This behaviour could be modelled using a set of nested variograms representing different scaled processes. However, the variogram

parameters were measured at the first break in slope and assumed to be the result of a single process. The combination of a number of different variograms, which would each up-scale differently and then be combined, could produce the difference in sill values observed. However a misfit in the range parameter might also be expected if this was the case.

Another reason for the difference in the sill values could be the choice of averaging process used to average the CT data. The averaged CT data was calculated using a kernel of Gaussian distributed weights. This weighting scheme may remove too much of the variability in the data resulting in the lower than expected sill values for the averaged data. To test this theory, the CT data from the 8626ft section of core was averaged again using a square kernel of uniform weights. Variograms were then calculated for the horizontal and vertical directions. The resulting variograms are shown in Figure 6.4.

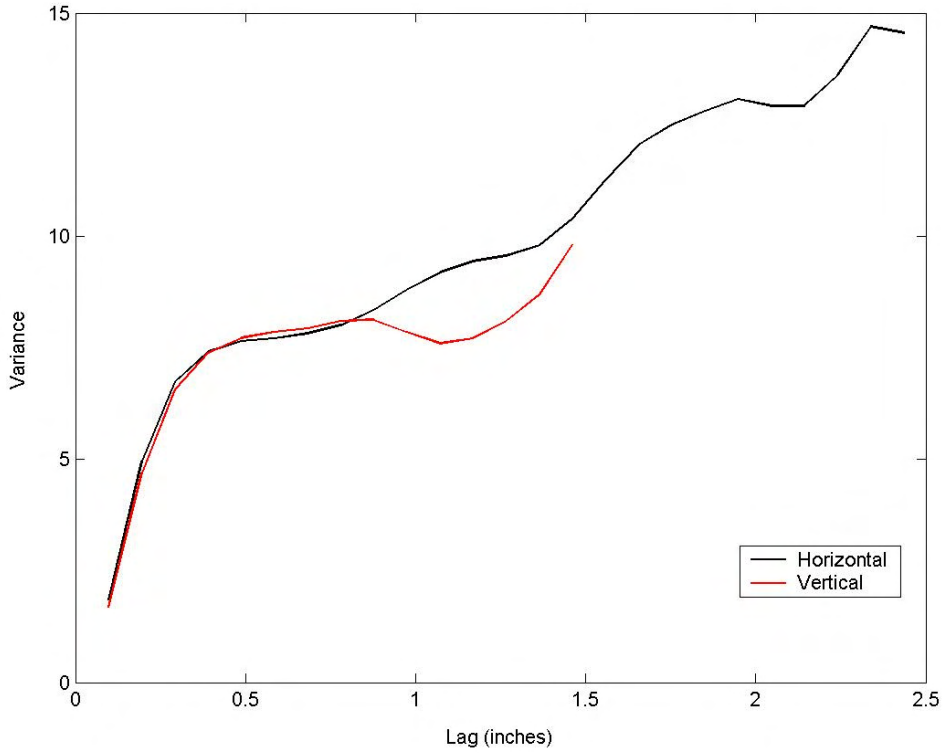

Figure 6.4. The variograms calculated from the CT scan of the 8626ft section of core, averaged using a uniform weighting kernel.

The variograms in Figure 6.4 have a range of 0.5 and a sill value of 7.5. This is taken from the first break in slope. As before the variograms show more complex behaviour beyond this point. The range values are similar to those up-scaled from both the original CT data variograms and from the Gaussian averaged CT data variograms (Figure 6.2). The sill values are slightly lower than those for the Gaussian averaged data (13) and far lower than the up-scaled data (40). The change in the averaging method for the CT data produced only a small change in the sill value. Therefore it is unlikely that the averaging process is the primary cause of the sill differences.

Finally, the datasets used may not be suitable for investigation using variograms. The use of variograms assumes that each data measurement is a draw from a random variable. This variable is assumed to be, at least, second-order stationary (Wackernagel, 1998). This means that the first two moments (mean and variance) of the random variable remain constant throughout the dataset. If they are not then the use of variograms is invalid and the scaling laws will not work.

6.7 Comparing Up-scaled CT and FMI

Though I have questioned whether the use of variograms is valid for the CT data sets, they will be used in this section simply to illustrate the general method for comparing parameters up-scaled from core measurements with those derived from wireline (image) logs. The up-scaled range parameters seem to match those determined from variograms of the averaged CT data. Therefore the method is illustrated by comparing up-scaled range parameters from the core data with those determined from FMI data.

6.7.1 8626ft Section

The range values for the FMI data were measured from variograms calculated using core length windows of data as described in chapters 4 and 5. The range values for the region of the borehole around the 8626ft section of core are shown in Figure 6.5.

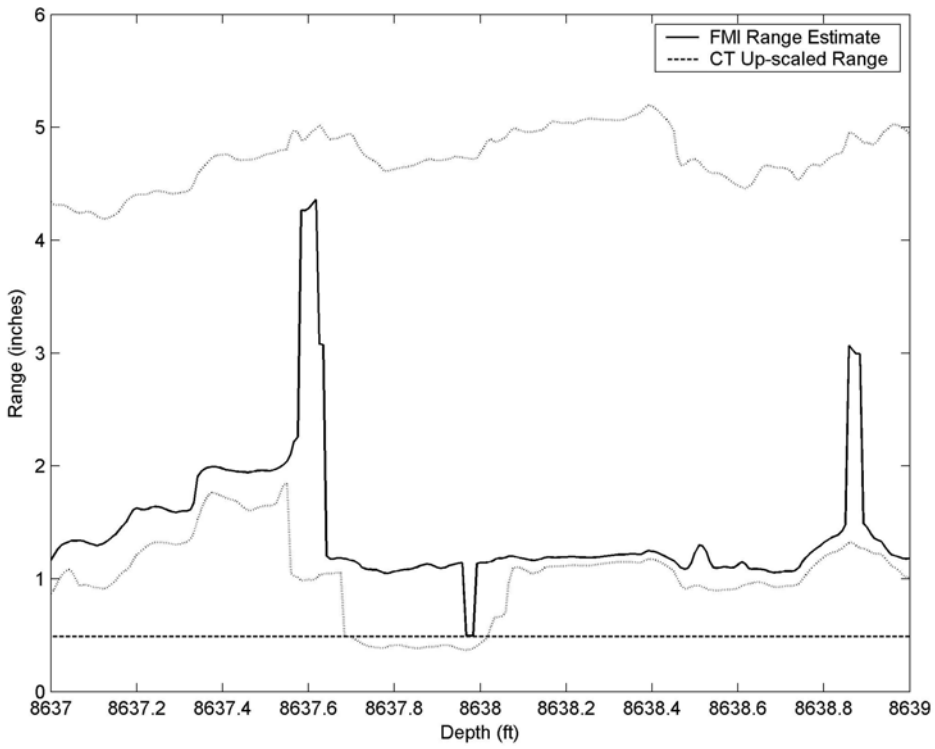

Figure 6.5. Comparison of Range values, for the 8626ft core section, determined from variograms calculated from core length windows of FMI data (solid line) and the up-scaled range value from the original CT data (dashed line). The uncertainty in the FMI range values, is also indicated (feint dotted line).

The best estimate of the FMI range values is shown in Figure 6.5 (solid line) as well as estimated upper and lower bounds on the values (feint dotted lines). The up-scaled range from the variogram of the original CT data is also marked (dashed line). The up-scaled range correlates well with a marked trough in the estimated FMI range at 8637.97ft. It is also within the range parameter bounds of uncertainty in the region 8637.69ft to 8638.04ft.

The combined likelihood function, containing the range parameter, in chapter 4 (figure 2.13) predicts a correlation around 8637.02ft. This is almost 1ft further up the borehole from that predicted by the up-scaled CT range. Potential reasons for this mismatch will be discussed in section 6.8.

6.7.2 8121ft Section

The comparison of the range values associated with the 8121ft section of core is shown in Figure 6.6.

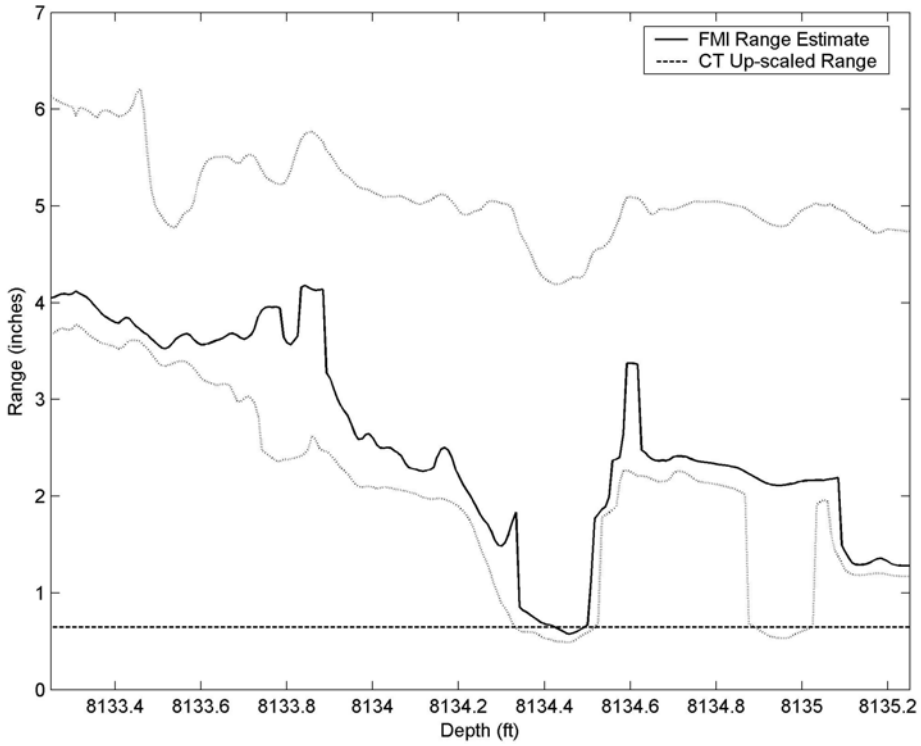

Figure 6.6. Comparison of Range values, for the 8121ft core section, determined from variograms calculated from core length windows of FMI data (solid line) and the up-scaled range value from the original CT data (dashed line). The uncertainty in the FMI range values, is also indicated (feint dotted line).

As before the best estimate (solid line), upper and lower bounds (feint dotted lines) and the up-scaled CT range (dashed line) is shown in Figure 6.6. The up-scaled range correlates well with the FMI in the region 8134.4ft to 8134.5ft, and lies within the bounds of uncertainty in the regions 8134.32ft to 8134.52ft and 8134.88ft to 8135.03ft.

The combined likelihood function, containing the range parameter, in chapter 5 (figure 3.6) predicts a correlation in the region 8134.4ft to 8134.55ft. This region matches well with that predicted by the up-scaled CT range.

6.7.3 Discussion of Comparison with FMI

The comparison of range parameters measured from variograms of FMI data and up-scaled from the original CT data, show regions of possible correlation in both core sections. This tells us the up-scaling laws may produce range values with the correct magnitude. However it is difficult to gauge the robustness of these correlations.

One test is to compare the correlations found above with those found in chapters 4 and 3 using combined likelihood functions. Whereas in the 8121ft core section the two correlations are in good agreement, in the 8626ft core section the depth match of the up-scaled correlation is significantly different, of the order of 1ft, from the combined likelihood correlation. This difference in behaviour for the different core sections makes it difficult to draw definite conclusions from the results, but the lack of consistent success suggests that the up-scaling method employed above is inappropriate for the range parameter, as well as for the sill as shown earlier.

6.8 Discussion and Conclusion

A major problem with the application of the scaling laws may lie in the use of simple variogram models. None of the variogram plots in this chapter have followed the conventional variogram shape that rises steeply at short lags before levelling off to a constant sill at longer lags. Instead they tend to rise again after having levelled off. This indicates that a nested combination of variogram models should be used to represent them. Each of these variograms would then be scaled independently before being combined. However there is currently no simple and reliable method for automatically fitting multiple variogram models. This would be a pre-requisite due to the large number of variograms produced from the FMI data. Therefore future work involving variogram scaling should include the development of a technique for the fast, accurate and efficient fitting of nested combinations of variogram models.

Another problem may be the unsuitability of carbonate data for analysis using variograms. The use of variogram analysis assumes that the mean and variance the same throughout the data. This is because variogram analysis assumes that the data

is a draw from a stationary random variable. If the mean and variance vary throughout the data then the use of a variogram analysis is not invalid.

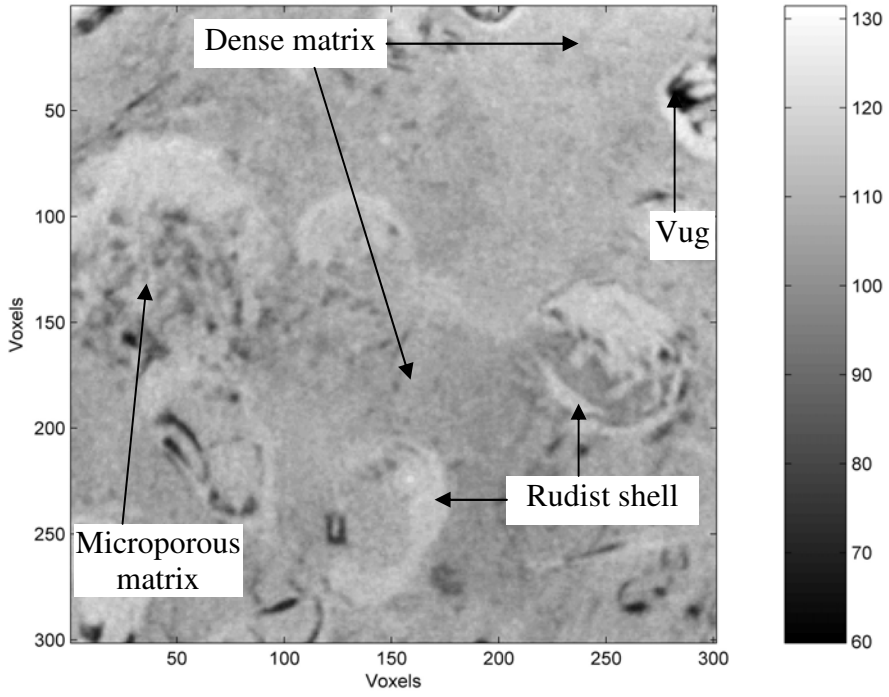

Figure 6.7. A random slice of porosity converted, CT data from the core section 8626ft. Each voxel has a side length of 0.165mm.

Figure 6.7 shows a slice through the CT data from the core section 8626ft. It shows the heterogeneity of the pore system of the carbonate rock, with different rock components clearly identifiable. On visual inspection this data does not appear to be stationary and therefore invalidates the use of a variogram analysis model.

The implication of this result is that the correlation results between up-scaled CT statistics and FMI data in section 6.7.3 are invalid as they are based on up-scaling variogram models. This can then explain the deficiencies in performance observed earlier in this chapter. Note, however, that the general approach to relating scale statistics with log data is still valid and could be applied if another up-scaling method could be found.

This conclusion does not call into question the validity of the statistical correlation technique described in chapter 4. In that technique the variogram range is used purely as a diagnostic statistic. It was calculated using the same technique, from CT and log data sets that had been converted to the same resolution. Hence, no scaling was performed, and the technique relied on finding a similar estimate for the range statistic in log and CT data sets. Even if the single variogram was inappropriate, a similar procedure applied to both data sets should find a similar range estimate when core and logs are correctly aligned, which is the only underlying assumption of that correlation methodology.

In summary, the results shown in this chapter have proved unsuccessful in validating the use of variograms and variogram scaling laws to up-scale CT data to FMI resolution. This failure can be attributed to the non-stationary nature of the data.

Chapter 7 – Modelling

7.1 Introduction

This thesis investigates some of the various challenges which need to be overcome to improve our understanding of carbonate reservoirs across a range of lengthscales (Figure 1.2). So far a method has been proposed which will allow extracted core to be precisely aligned with borehole measurements. A precise correlation would allow up- and down-scaling relationships to be developed between the core and borehole data sets. One such scaling method, using variograms has been demonstrated. Once scaling relationships have been developed the goal is to apply them in areas of the borehole with log measurements but without extracted core. In these regions, particularly for carbonate formations, the porosity information is required in 3D to understand the storage and flow of fluids within the formation. Therefore a method is required to simulate the 3D volume of rock from which the borehole has been cut.

The simulation of geological formations is a useful tool to aid our understanding of how structures are formed. It can also help constrain predictions about what lies in the subsurface. Ideally these simulations would be created by modelling the cumulative effects of a number of physical processes in a *process model*. However in geological structures the processes are often highly complex and poorly constrained (Wijns et al., 2003). In carbonates in particular, the complex biological origins and subsequent diagenetic overprinting creates highly heterogeneous formations (Choquette and Pray, 1970; Lucia, 1995). In such circumstances a *stochastic* approach can be used. A stochastic simulation is one based on the probability of given events or states occurring.

In geology, many sequences and structures are assumed to be Markovian in nature. A Markov process is one in which future states depend only on the present state, with past states having no influence (Fisz, 1963). In a discrete system Markov processes are referred to as *Markov chains*. For a simulation, Markov behaviour implies that probabilities measured at small scales are sufficient to simulate large scale structures.

Markov chain theory can be applied using transition probabilities. These measure the probability that a cell of interest contains a certain state given the state of reference cells. The transition probabilities are calculated from a training image with similar structures to those in the area of interest. This approach was initially used to simulate 1-D lithological sequences in boreholes (Vistelius, 1949; Gingerich, 1969; Doveton, 1971). Advances were then made in the field of image processing, expanding Markov chain theory into multiple dimensions (Geman and Geman, 1984; Qian and Titterington, 1991). This lead to a similar expansion in geological Markov chain simulations to 2-D (Li et al., 2004; Wu et al., 2004) and 3-D simulations (Carle and Fogg, 1997; Wu et al., 2006).

In this chapter I propose a method for the simulation of borehole data using Markov chain theory. While the technique used for individual cell simulation is similar to those used in previous studies, the method utilises a novel approach for capturing transition probabilities from the curved borehole wall and determining the order of cell simulation. The borehole data used came from the Fullbore MicroImager (FMI) resistivity tool, which produces a 2-D image of the borehole wall. Initially, to develop the simulation method, only a 2-D binary simulation is created. This minimises the number of transition probabilities required. The 2 – D simulation is orientated perpendicular to the trajectory of the borehole. Therefore only a single row of FMI data is used to calculate two point transition probabilities between the nearest neighbouring cells. These transition probabilities are then combined to infer multi-point statistics which cannot be measured directly due to the tool geometry. Two methods are proposed for this combination, one based on averaging and another using least squares estimation. The two methods also produce a ranking to determine the order in which cells should be simulated. The two methods are then compared using a set of synthetic geological models.

7.2 FMI Layout

The FMI tool gathers resistivity data from the wall of a borehole through a system of pads and flaps. The layout of the pads and flaps around a cross-section of the borehole is shown in Figure 7.1.

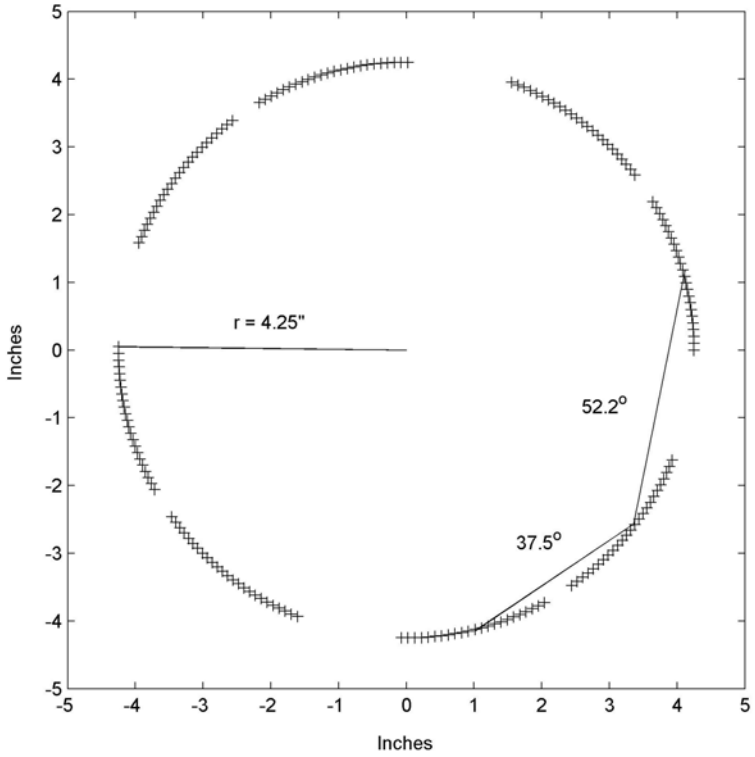

Figure 7.1. Arrangement of FMI electrode pads and flaps

Transition probabilities, the probability of a cell containing a certain state given the state of surrounding cells, are conventionally calculated from linear data, such as boreholes (Doveton, 1971), or horizontal surfaces, such as maps (Weissmann et al., 1999). As the FMI data is collected from a cylindrical surface it must be assigned to an appropriate coordinate system to allow transition probabilities to be calculated.

The obvious and mathematically rigorous coordinate system would be Polar coordinates, using the angle θ around the borehole and the borehole radius, r. With the centre of the borehole taken to be the origin of the system, the measurements from the borehole wall will provide information about transitions in the θ direction. However, as the measurements are all made at a constant radius, transitions in the r

direction will not be observed. This shows that the FMI data geometry is particularly deficient in transition information.

Instead the FMI measuring positions were converted from a Polar to a Cartesian coordinate system. A Cartesian grid was chosen such that each FMI measurement could be assigned to a separate grid cell. This allows transitions to be measured in all directions, but still at a fixed radius, *r*. Hence, the transition probabilities should not, in principle, be used to simulate away from the fixed radius, *r*. This forces the assumption to be made that the Cartesian transition probabilities are independent of radius.

A 125 cell, square grid was setup to represent a 9" square centred on the centre of the borehole (each cell being 0.072" in side length). For a single horizontal slice each element of FMI data was converted from polar coordinates to Cartesian coordinates and then assigned to an individual cell in the grid. Each cell of data was then binarised into two states, 0 and 1, depending its value was above or below a threshold. An example of a horizontal slice of the FMI data represented in this way, using a threshold of 0.2, is shown in Figure 7.2.

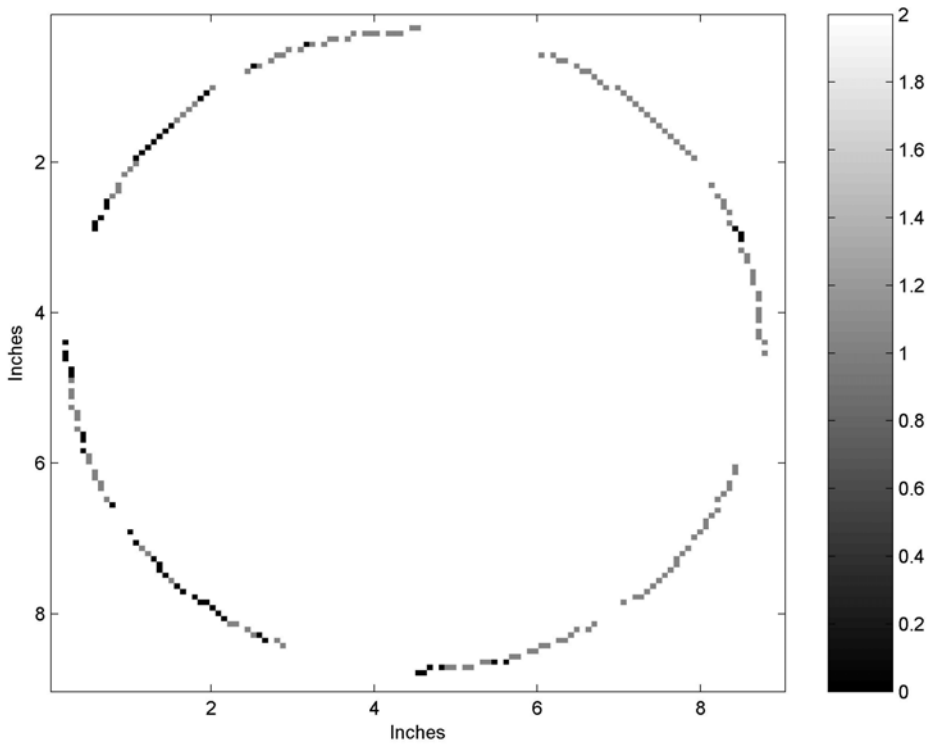

Figure 7.2. Example of FMI data assigned to square grid. The data has been binarised and cells containing data are either grey (solid) or black (pore), while empty cells are white.

7.3 Calculation of Transition Probabilities

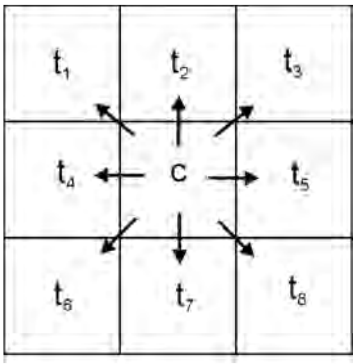

Transition Template

Transitions : t_i i = 1,..,8
Centre : c

Possible Transitions for each t_i:

	c	**t_i**
Event 1	0	0
Event 2	0	1
Event 3	1	0
Event 4	1	1

Figure 7.3. Template used to capture two-point transition probabilities; arrows define the direction of each of the surrounding cell's relationship to the central cell.

To calculate the two-point transition probabilities the 9-cell template in Figure 7.3 is in turn centred above each FMI data measurement location in Figure 7.2. Those surrounding cells, t_i, containing FMI data are identified, each of which has a direction relative to the central cell as defined in Figure 7.3. The binarised data values within these surrounding cells and the central cell determines one of four possible transition events, 1 to 4. This process is repeated for each of central cell location in Figure 7.2 and the number of each type of transition observed, and their directions are histogramed and stored in a 4×8 matrix. The transition probability $p_{i,0}$, for a particular direction i, of a 0 being in a target cell given that the reference cell contains a 0, is then calculated using:

$$p_{i,0} = p(t_i = 0 \mid c = 0) = \frac{n_1}{n_1 + n_2} \qquad \ldots(7.1)$$

where n_k is the number of times event k is observed in the histogram. Similarly the probability of a 0 in the target cell given the reference cell contains a 1 is then:

$$p_{i,1} = p(t_i = 0 \mid c = 1) = \frac{n_3}{n_3 + n_4} \qquad \ldots(7.2)$$

To make a prediction in a particular cell, given the state of a neighbouring reference cell, the relevant probability of the cell containing a 0 for the orientation between the cells is calculated. Then a random draw is made from the range 0 to 1 using a random number generator (in this work the *rand* function from Matlab is used (MathWorks, 2002)). If the result is less than the probability then the cell is assigned the value 0 and if it is greater than the probability then the cell is assigned the value 1.

7.4 Simulation

To simplify the problem, while investigating different simulation strategies, it was restricted to the simulation of a 2D surface. The surface represents a single

horizontal slice perpendicular to the borehole. Data taken from the FMI tool is included in the surface and acts as a starting point for the simulations.

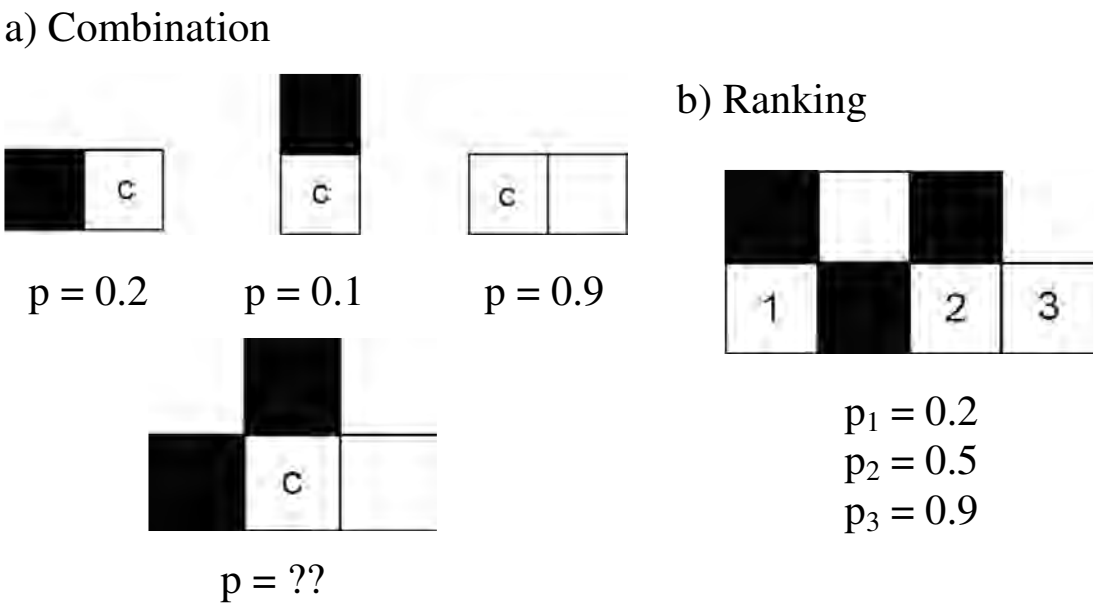

Figure 7.4. Illustration of the two challenges to creating a simulation using binary data (black and white): a) How to combine two-point transition probabilities to infer multi-point probabilities. b) The ranking problem of how to select the order in which cells are simulated.

There are two main challenges to be tackled in the simulation. Firstly there is the problem of how to combine two-point transition probabilities (Figure 7.4 a). The cells which are to be simulated may be surrounded by more than one cell containing data. Each of these data cells will have a different transition probability for the state of the cell to be simulated. The simulation technique must combine these individual two-point probabilities to infer the multi-point probability. Secondly there is the issue of how to decide upon the next cell to simulate (Figure 7.4 b). With each cell assigned a multi-point transition probability a method is then required which ranks the cells in the order in which they should be simulated. Two different methods are proposed to tackle these problems one using simple averaging, while the second utilises a least squares approach.

7.5 Neighbourhood Averaging

The simplest method to combine a number of transition probabilities is to take an average value. This approach is used by (Wu et al., 2006) to combine transition probabilities calculated in 3 perpendicular planes in order to create a 3D volume.

For any given cell, with i nearest neighbour cells containing data, the probability of the cell containing a 0 can be calculated using:

$$\overline{p_0} = \frac{\sum_{i=1}^{k} p_{i,0}}{k} \qquad \ldots(7.3)$$

Then to determine the order in which cells should be simulated each cell in the surface is ranked according to the number of nearest neighbouring cells containing data. The cell with the maximum number of neighbours containing data is then simulated. In the event of more than one cell having the same maximum number of neighbours, one of them is selected at random. After a cell has been simulated the ranking of its neighbouring cells is re-evaluated. This method ensures that the simulation is always carried out for cells which have the greatest amount of information at each step.

7.6 Least Squares

7.6.1 Combination

The neighbourhood averaging approach weights each transition probability equally and takes no account of how well each probability is determined. A more mathematically rigorous method is to use a least square approach, with each transition probability weighted by a function of its variance.

The least squares approach requires the assumption that each of the individual transition probabilities follows a binomial distribution. A binomial distribution is the discrete probability distribution which would be expected following a series of independent yes/no trials, such as tossing a coin (Wetherill, 1982). Say x is a random

variable that takes the values 0 or 1 according to a Binomial distribution. Then, consider *N* trials or draws of *x*, and let *r* be the number of these that result in a value *x = 1*. Then the Binomial distribution of *r* is:

$$P(r) = {}^{N}C_{r}\theta^{r}(1-\theta)^{N-r} \qquad \ldots(7.4)$$

where θ is the probability of trial resulting in *x = 1* and

$${}^{N}C_{r} = \frac{N!}{r!(N-r)!}$$

which is the binomial coefficient and is the number of possible ways of achieving r successes in N trials. The expectation of *r* is given by,

$$E(r) = N\theta \qquad \ldots(7.5)$$

and the variance of *r* is,

$$\sigma^{2}(r) = N\theta(1-\theta) \qquad \ldots(7.6)$$

If it is assumed that the transition probabilities follow a binomial distribution, in that they represent the probability of a trial with only two outcomes, 0 and 1. Then the variance of the transition n_1 in direction *i* is,

$$\sigma^{2}(n_1) = Np_{i,0}(1-p_{i,0}) = (n_1+n_2)p_{i,0}(1-p_{i,0}) \qquad \ldots(7.7)$$

Note that the term n_1 appears on both sides of the equation, this is because $n_1+n_2 = N$ the number of trials carried out. The variance on probability $p_{i,0}$ is then:

$$\sigma^{2}(p_{i,0}) = \sigma^{2}\left(\frac{n_1}{n_1+n_2}\right) = \frac{p_{i,0}(1-p_{i,0})}{n_1+n_2} = \frac{n_1 n_2}{(n_1+n_2)^{2}} \qquad \ldots(7.8)$$

Similarly the variance on the probability $p_{i,1}$ is:

$$\sigma^2\left(p_{i,1}\right)=\sigma^2\left(\frac{n_3}{n_3+n_4}\right)=\frac{p_{i,1}\left(1-p_{i,1}\right)}{n_3+n_4}=\frac{n_3 n_4}{\left(n_3+n_4\right)^2} \qquad \ldots(7.9)$$

Then the combination of transition probabilities to estimate the overall probability of a cell having a zero can be set out as a least squares problem weighted by variance. A least squares estimate can be obtained using the following definition (Sneider and Trampert, 1999):

$$\hat{p}_0=\left[A^T Q^T Q A\right]^{-1} A^T Q^T Q d \qquad \ldots(7.10)$$

With:

$$A=\begin{bmatrix}1\\|\\|\\1\end{bmatrix},\ Q^T Q=\begin{bmatrix}\sigma_1^2 & - & 0\\ | & \backslash & |\\ 0 & - & \sigma_k^2\end{bmatrix},\ d=\begin{bmatrix}p_1\\|\\|\\p_k\end{bmatrix}=A\hat{p}_0$$

A is a linear operator between the model and data space, $Q^T Q$ is the covariance operator made up of the variance estimates on the individual transition probabilities and d is the vector of individual transition probabilities. An estimate of the combined transition probability of the target cell containing a 0, $\hat{p}_0$, constructed from k individual transition probabilities, is then given by:

$$\hat{p}_0=\frac{\sum_{i=1}^{k}\frac{p_{i,0}}{\sigma^2\left(p_{i,0}\right)}}{\sum_{i=1}^{k}\frac{1}{\sigma^2\left(p_{i,0}\right)}} \qquad \ldots(7.11)$$

The variance of the combined transition probability of the target cell containing a 0 is given by:

$$\overline{\sigma_0^2} = \left[\sum_{i=1}^{k} \frac{1}{\sigma^2\left(p_{i,0}\right)} \right]^{-1} \qquad \ldots(7.12)$$

7.6.2 Ranking

To determine the order in which cells are selected for simulation they are ranked according to both the confidence in the combined probability estimate, and the *strength* of the probability. In this work the term strength is used to describe how close the probability is to 0 or 1. In the extreme case, a well constrained probability of 0 or 1 will provide a prediction with a great deal of certainty, whereas a prediction made using a probability of 0.5 is simply a fair random draw.

The strength of a probability function is measured using a 'Utility' function, taken from Decision Theory (Berger, 1980). The Utility function reflects the strength of information contained within different values of the variable of interest. In our case it is a quadratic function of probability *U(p)*:

$$U(p) = 4p^2 - 4p + 1 \qquad \ldots(7.13)$$

The utility function is dimensionless and has a value of 1 for $p = 0$ and $p = 1$, and a minimum of 0 for $p = 0.5$. The uncertainty in the combined probability estimate is assumed to follow a Gaussian distribution with the variance determined in equation 7.12. An example of the utility function, *U(p)*, and a Gaussian distribution of transition probabilities are shown in Figure 7.5.

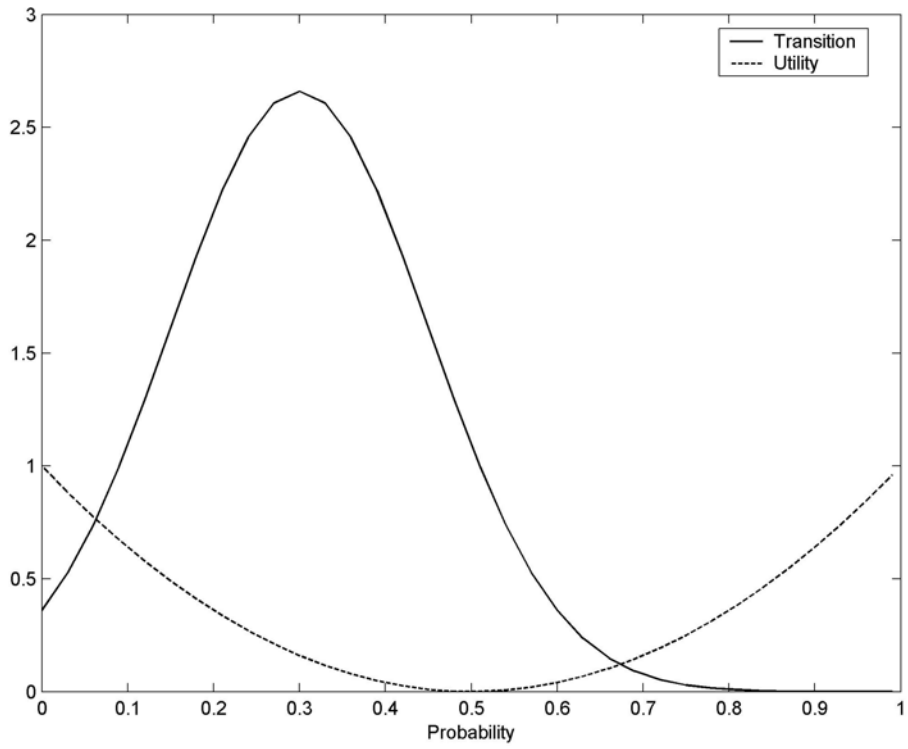

Figure 7.5. An example of a Gaussian distribution of transition probabilities (mean=0.3, variance=0.15) and the utility function, *U(p)*.

For each cell a ranking, *R*, can be calculated by integrating between 0 and 1, the product of the Gaussian distribution of transition probabilities and the utility function:

$$R = \int_0^1 \left[\left(\frac{1}{\sigma_0 \sqrt{2\pi}} \exp\left(\frac{-\left(p - \bar{p}^2\right)}{2\sigma_0^2} \right) \right) * \left(4p^2 - 4p + 1\right) \right] dp \qquad \ldots(7.14)$$

7.7 Test Results

There are two major areas for investigation in the simulation problem. The first concerns the ability of the FMI data to capture sufficient spatial information to enable realistic simulations to be created. Secondly there is the performance of the proposed simulation methodologies in creating simulations which honour the spatial information.

7.7.1 Synthetic Features

To investigate the simulation problem, code was developed to simulate planes containing a number of different synthetic geological features. The planes were the same size as the FMI grid shown in Figure 7.2: 125×125 cells. This enabled the slices to be used as training images for the simulation from which synthetic FMI data can also be extracted and for comparison with the simulation results.

Examples of the synthetic features used are shown in Figure 7.6(a-e). They are respectively,

Faults:	A series of straight lines, with a constant orientation, representing any linear features (faults, closed fractures etc.)
Vugs:	A series of circles that represent the large scale pores sometimes found within carbonates.
Faults and Vugs:	A mixture of both Fault and Vug features.
Rudists:	A series of crescent shapes, representing the rudist shells observed in the carbonate core sections.
Fractures:	A series of elliptical features similar to the Fault features. These represent open fractures which change in aperture along their length.

All the features were randomly distributed within the plane and varied in size. The features were represented in binary form.

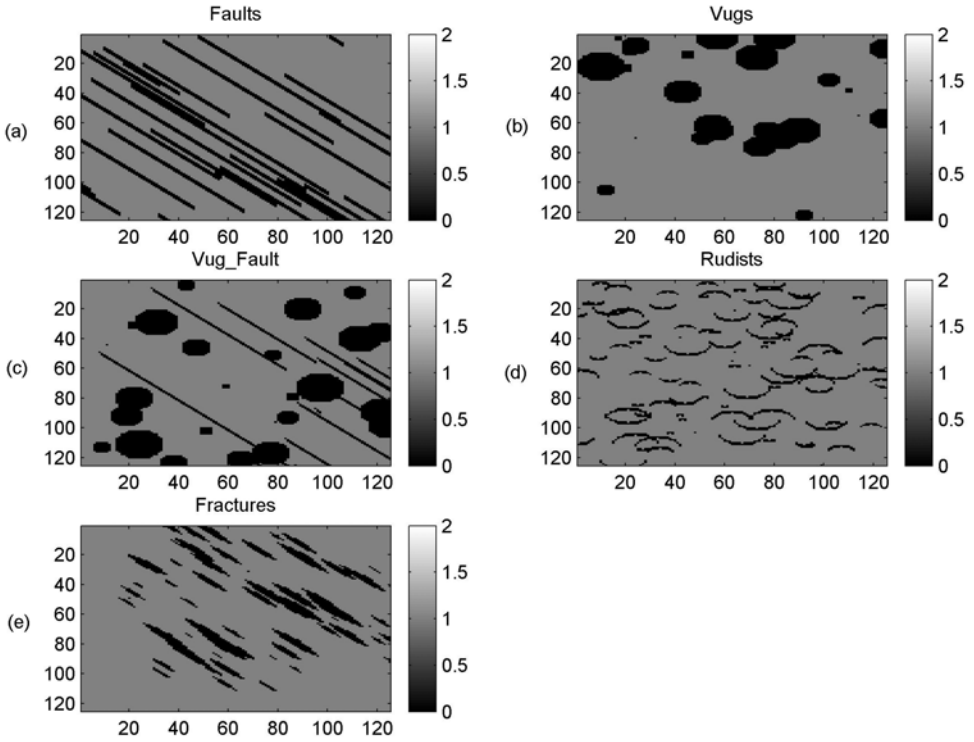

Figure 7.6. Examples of the synthetic features used during the testing of the simulation method.

The transition probabilities, calculated from different images (Training (synthetic), FMI, or simulated realisations), were compared using the root mean square error (RMSE). The RMSE, *R*, between the two transition probabilities *a* and *b*, is defined as:

$$R = \sqrt{\sum_{i=1}^{N}\left(\frac{a_i - b_i}{N}\right)^2} \qquad \ldots(7.15)$$

The calculation is normalised by *N*, the number of transition probabilities calculated for each image. In this case *N* equals16 as there are 8 transition probabilities for the centre cell containing a 0 and 8 fro the centre cell containing a 1. To estimate the variability in the RMSE the comparison was repeated using twenty different sets of statistics allowing the standard deviation to be calculated. To provide an indication of the scale of the RMSE values the absolute average value (AAV) was also calculated using:

$$AAV = \frac{1}{N}\sum_{i=1}^{N}\frac{|a_i + b_i|}{2} \qquad \ldots(7.16)$$

The AAV provides a single value which can be compared with the RMSE value to estimate the scale of the RMSE value relative to the probabilities from which it is calculated.

7.7.2 FMI Results

To test the ability of the roughly circularly sampled FMI data to capture the correct spatial statistics of features in a plane, a set of experiments were run. First a synthetic training image containing Fault features was created. Synthetic FMI data was then extracted from this image by placing an FMI template similar to that in Figure 7.2, over the image and extracting the data (0 or 1) that lies beneath the template. The transition probabilities for both the training image and the synthetic FMI were calculated. The two sets of statistics were then compared using the root mean squared error (RMSE) in Equation 7.15.

This comparison was repeated using an increasing numbers of training images to calculate the transition probabilities. The number of images was increased as this should improve the accuracy of the FMI statistics as it allows the FMI geometry to sample more of the structures present and better constrain the transition probabilities. The transition probabilities were averaged over the number of images by summing the transition counts for each image. The entire set of experiments was then repeated using each of the different synthetic feature types in Figure 7.6. The results are shown in Figure 7.7.

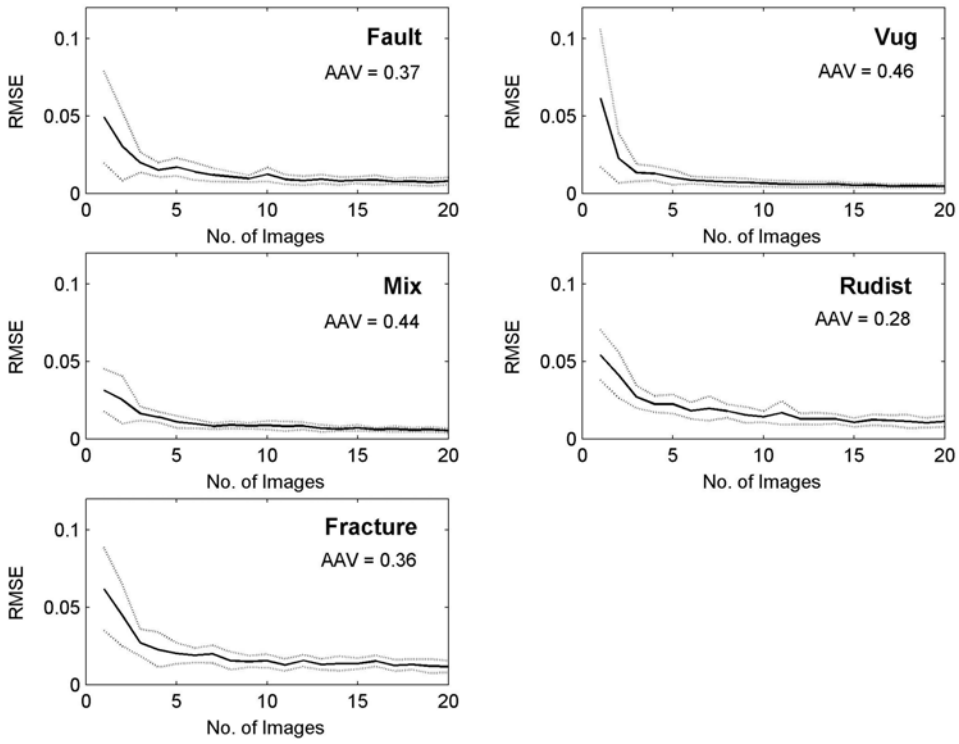

Figure 7.7. The mean RMSE between transition probabilities calculated from training images and synthetic FMI extracted from the training images. The dotted lines show the +/- 1 standard deviation from the mean RMSE.

The mean RMSE (solid lines) for all of the synthetic features show a decrease as the number of images over which they are measured increases. They all level off to relatively constant values below 0.02, with the rate of decrease in RMSE greatest when using 1-4 images. The standard deviation (dotted lines) also decreases as the number of images increases. The best RMSE values are consistently observed for the simple fault and vug features.

The AAV results are given as a single average value as the plots were flat curves. If the curves had been included in Figure 7.7 then the detail of the RMSE results would have been lost. For each feature type the RMSE value levels off at 0.02 which is less than 10% of the AAV value. This suggests that the FMI geometry is sufficient to capture spatial statistics, particularly if averaged over a number of images.

7.7.3 Simulation Results

Having successfully tested the ability of the FMI geometry to capture canonical pore-scale spatial statistics, the two simulation methods proposed were then compared. This was carried out using a similar experiment to that used to test the FMI layout. An outline of the experiment is shown in Figure 7.8.

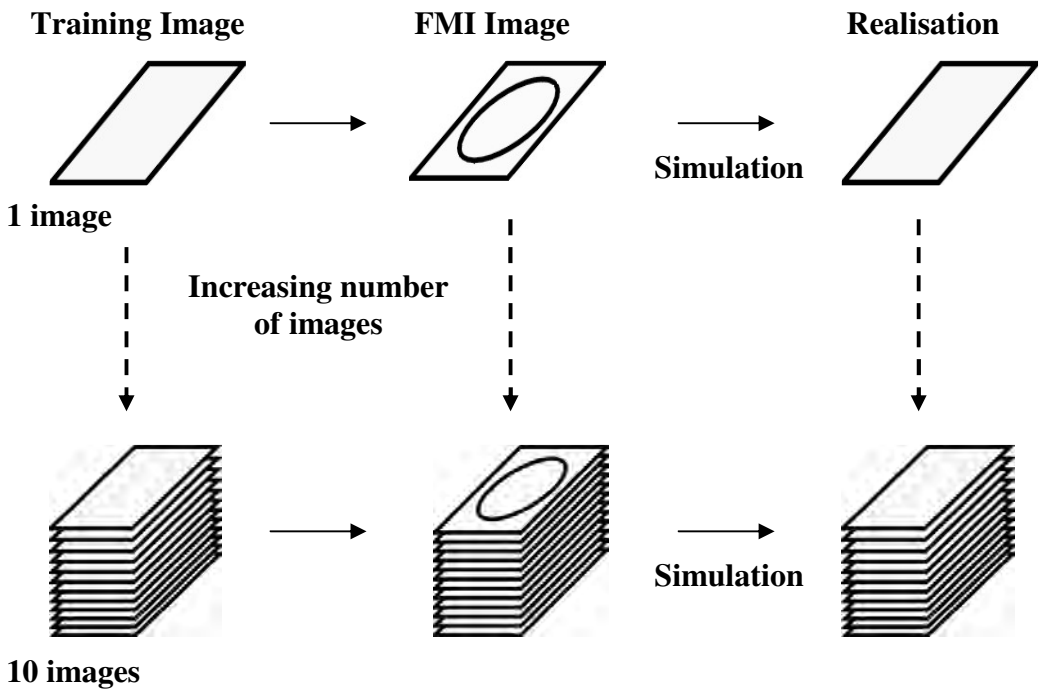

Figure 7.8. Outline of the experiment used to asses each simulation method.

Again a single training image was constructed, from which synthetic FMI data was extracted. Then the transition probabilities calculated from the synthetic FMI data were used to create a realisation using one of the simulation methods. Transition probabilities were calculated for the realisation and compared, using the RMSE, against both the FMI probabilities used in the simulation, and those calculated from the initial training image. The variability in the comparison was determined by repeating the process 20 times.

The whole process above was then repeated ten times, each time increasing the number of training images and the number of realisations by one. Finally, all of the

above experiments were repeated using each of the different types of synthetic features in Figure 7.6. The results are shown in Figures 7.9 to 7.13.

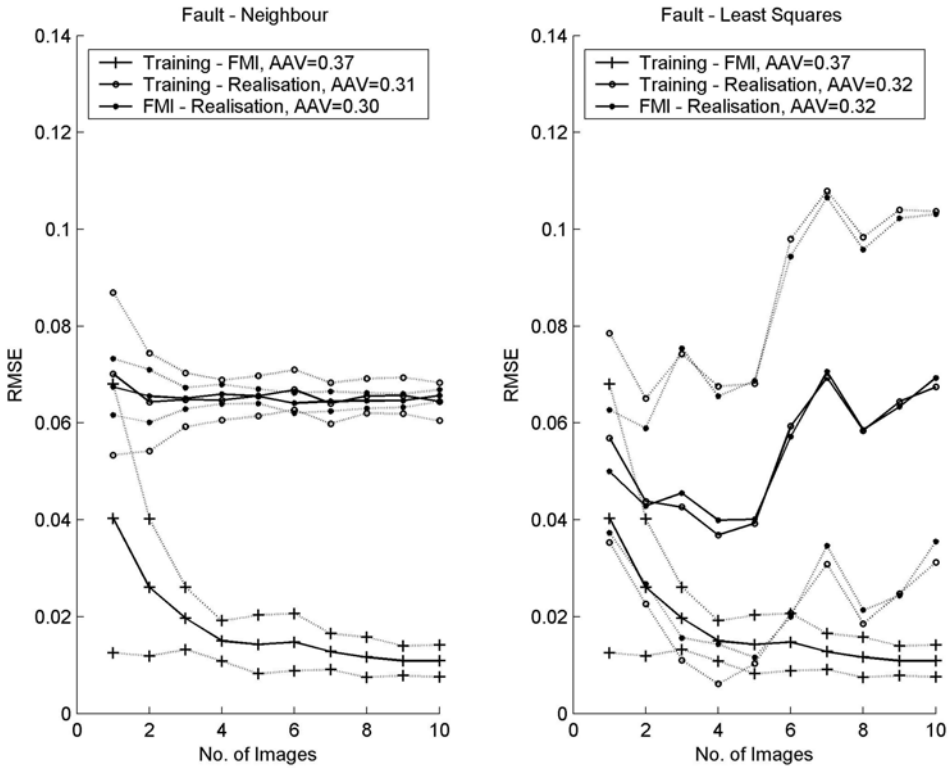

Figure 7.9. The mean RMSE between pairs of transition probabilities calculated from training images, synthetic FMI data, and simulated realisations using Fault features. The results using the Neighbourhood averaging method are shown on the left, and the results using the Least Squares method on the right. The dotted lines show +/- 1 standard deviation from the mean RMSE. The legends give the AAV value for each comparison.

The Fault features appear to be the simplest of those created, consisting of straight lines with a constant orientation. They might therefore be expected to be the simplest to simulate. The comparison of the RMSE results (Figure 7.9) for the two simulation methods however shows significant differences between the various sets of probabilities. Only the comparison between the training image and FMI statistics ("+" symbol) is the same across the two plots as this is unaffected by the choice of simulation method and is the same as in Figure 7.7. The results for the neighbourhood averaging method (Figure 7.9, left) are very consistent for both the Training image/Realisation and FMI/Realisation

comparisons. The mean RMSE remains steadily around 0.065 as the number of images increases. The range of RMSE values (dotted lines) reduces as the number of images used is increased from 1 to 10. The RMSE value of 0.065 represents a 20% error when compared to the AAV values of around 0.3.

The RMSE results for the Training image/Realisation and FMI/Realisation mean using the least squares method (Figure 7.9, right) are again very consistent with each other. However instead of remaining constant they start off at 0.055, drop to 0.04 using 4 images, then rises to 0.065 using 10 images. The greatest difference from the neighbourhood averaging results is in the variation of the RMSE values, with one standard deviation starting around 0.02 using 1 image and increasing to 0.03 using 10 images. Again the RMSE value represents a 20% compared with the AAV value.

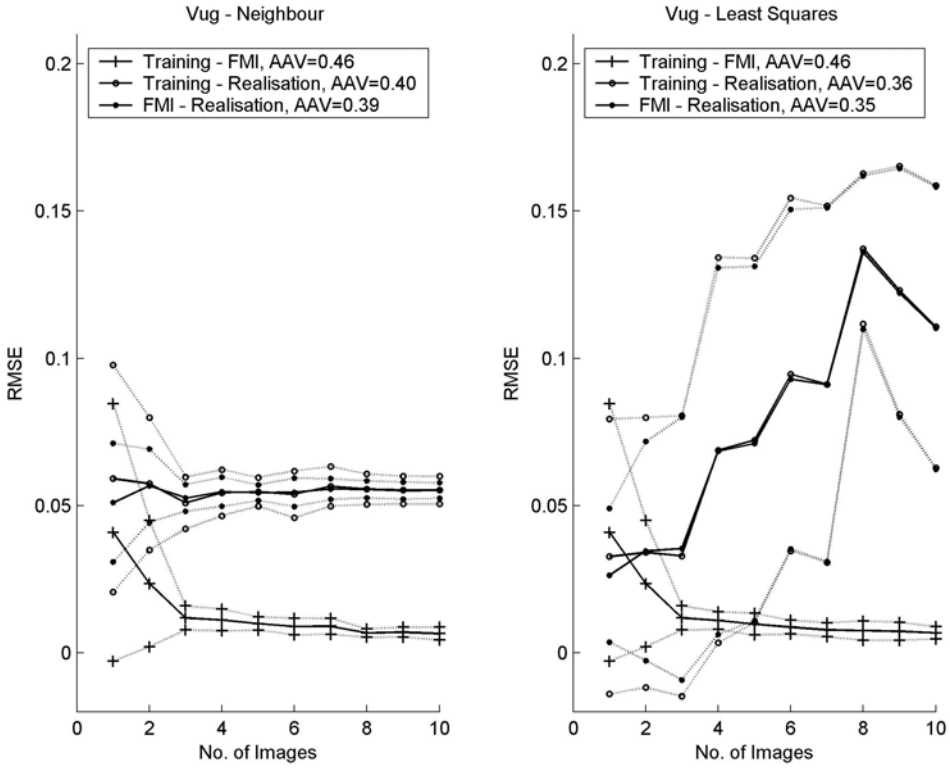

Figure 7.10. The mean RMSE between pairs of transition probabilities calculated from training images, synthetic FMI data, and simulated realisations using Vug features. The results using the Neighbourhood averaging method are shown on the left, and the results using the Least

Squares method on the right. The dotted lines show +/- 1 standard deviation from the mean RMSE. The legends give the AAV value for each comparison.

The comparison of the simulation methods using the vug features (Figure 7.10) again shows significant differences between them. As with the fault feature results, the comparison between the training image and realisation and the FMI and realisation are very similar using the neighbourhood averaging method (Figure 7.10, left). The mean RMSE for both comparisons remains just above 0.05 as the number of images increases. The variation in RMSE values (dotted line) is again reduced by increasing the number of images used. The RMSE value of 0.05 represents an error of 12% compare to the AAV value.

Using the least squares method (Figure 7.10, right), the two comparisons, Training image/Realisation and FMI/Realisation are again very similar. The mean RMSE starts around 0.03 (8% of AAV) using one image and rises to a peak of 0.14 (40% of AAV) using 8 images before dropping slightly, to 0.11 (31% of AAV) using 10 images. As with the fault features the range of RMSE values (dotted line) is much larger than when using the neighbourhood averaging method. One standard deviation starts at 0.04 using one image and remains consistent until 8 images when it drops to 0.02 before increasing again.

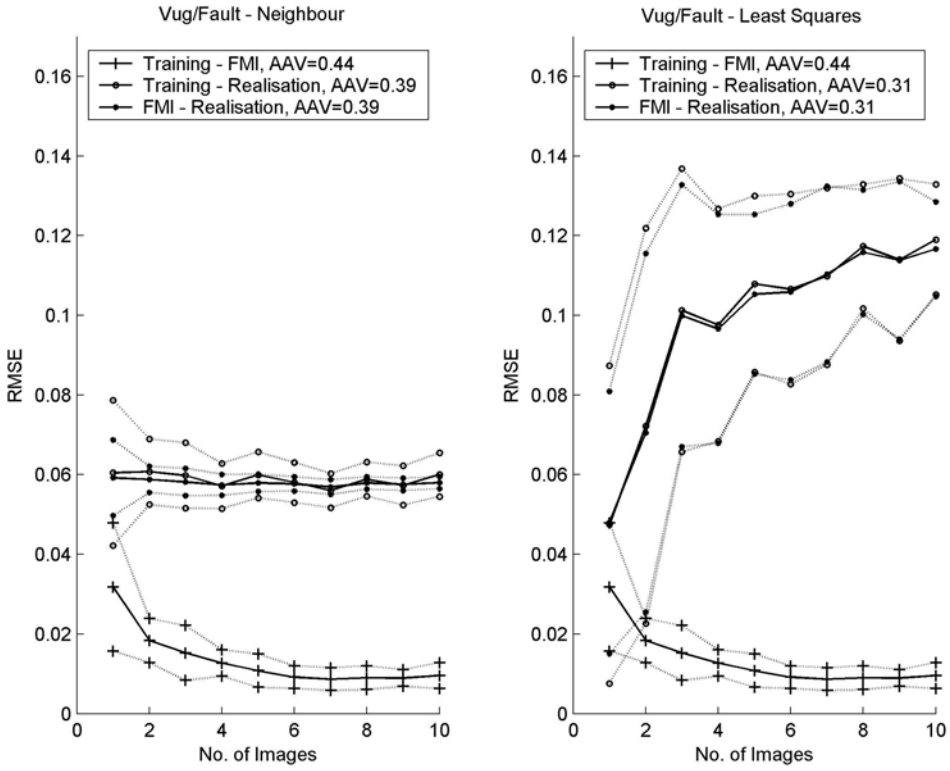

Figure 7.11. The mean RMSE between pairs of transition probabilities calculated from training images, synthetic FMI data, and simulated realisations using a mixture of Fault and Vug features. The results using the Neighbourhood averaging method are shown on the left, and the results using the Least Squares method on the right. The dotted lines show +/- 1 standard deviation from the mean RMSE. The legends give the AAV value for each comparison.

Using a mixture of vugs and faults again produces different results for the two simulation methods. The mean RMSE values for the realisation comparisons, using the neighbourhood averaging method (Figure 7.11, left), are again similar and consistently around 0.06 (15% of AAV). The range of RMSE values is constrained as the number of images is increased.

The mean RMSE values for the realisation comparisons, using the least squares method (Figure 7.11, right), start at 0.05 (16% of AAV) using one image and rise rapidly to 0.1 (32% of AAV) using 3 images then the increase slows reaching 0.12 (39% of AAV) using 10 images. Unlike the individual fault and vug results in Figures 7.9 and 7.10 the range of RMSE values decreases as the number of images

used increases, with one standard deviation starting at 0.03 using one image and dropping to 0.01 using 10 images.

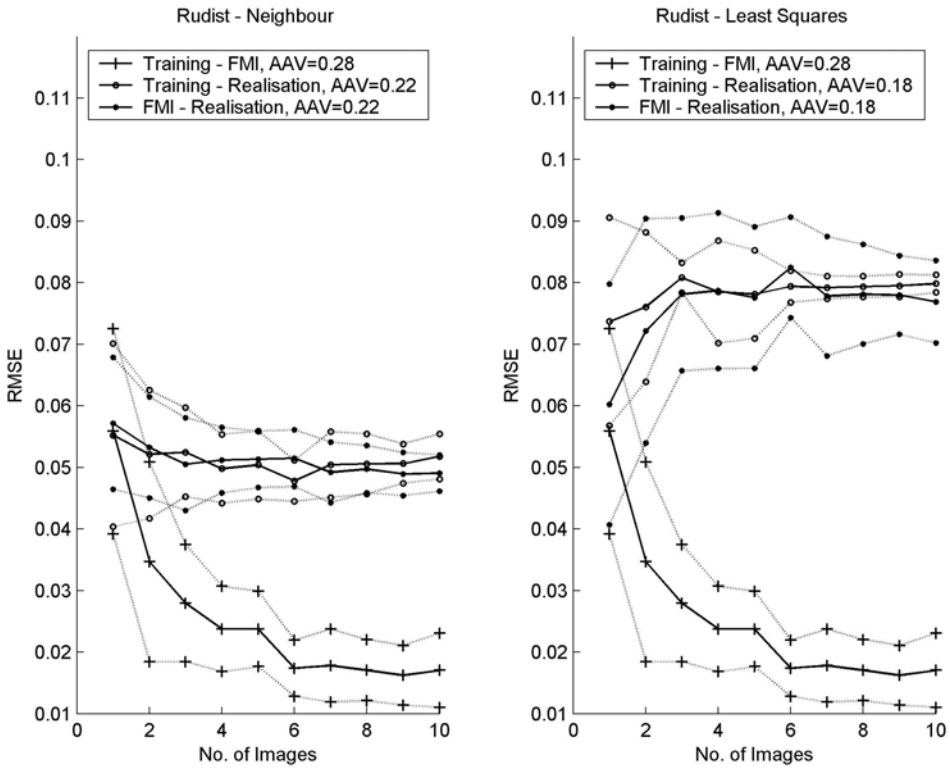

Figure 7.12. The mean RMSE between pairs of transition probabilities calculated from training images, synthetic FMI data, and simulated realisations using Rudist features. The results using the Neighbourhood averaging method are shown on the left, and the results using the Least Squares method on the right. The dotted lines show +/- 1 standard deviation from the mean RMSE. The legends give the AAV value for each comparison.

The comparison using the rudist features shows similar behaviour using the two simulation methods, with both levelling off to a constant value. Using the neighbourhood method (Figure 7.12, left) the mean RMSE starts at 0.056 (25 % of AAV) and falls to 0.051 (23% of AAV) using 10 images. Compared to previous results the training image/realisation and FMI/realisation comparisons are not as similar. The range of RMSE values again drops as the number of images increases.

The mean RMSE values using the least squares method (Figure 7.12, right), start at 0.06 (33% of AAV) and 0.073 (40% of AAV) for the FMI/realisation and training

image/realisation comparisons respectively. These both rise to a value of 0.078 (43% of AAV) using 10 images. As with using the neighbourhood method the two comparisons are not as similar as the results using faults or vugs. The range of RMSE values drops as the number of images increases, with one standard deviation dropping from 0.02 using one image down to 0.005 using 10 images.

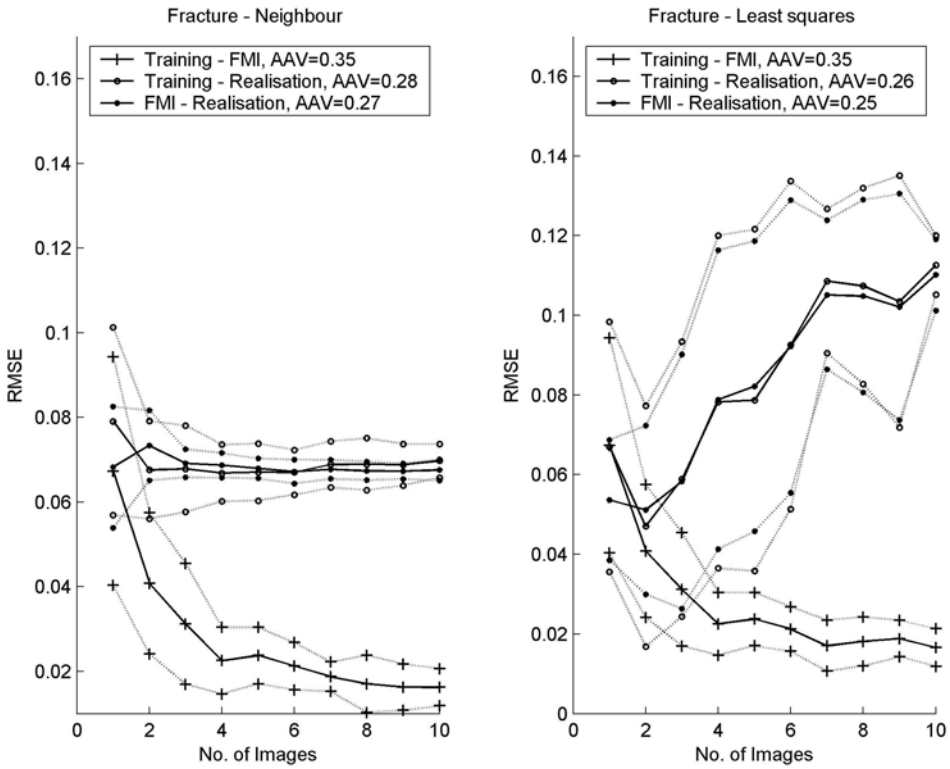

Figure 7.13. The mean RMSE between pairs of transition probabilities calculated from training images, synthetic FMI data, and simulated realisations using Fracture features. The results using the Neighbourhood averaging method are shown on the left, and the results using the Least Squares method on the right. The dotted lines show +/- 1 standard deviation from the mean RMSE. The legends give the AAV value for each comparison.

The results obtained using the fracture features are similar to those obtained using the fault features (Figure 7.9). This is to be expected as the fractures are ovals with a constant orientation like the faults. The neighbourhood results (Figure 7.13, left) are consistently around 0.07 (25% of AAV) compared with 0.065 (20% of AAV) using the faults. The standard deviation in the RMSE values drops rapidly as the number of images increases, dropping from 0.02 down to 0.004.

The mean RMSE results using the least square method (Figure 7.13, right) start around 0.06 (24% of AAV) and rise to 0.115 (46% of AAV) using 10 images. The range of RMSE values decreases as the number of images increase, with one standard deviation dropping from 0.03 using one image to 0.01 using 10 images.

7.8 Discussion

The comparison between the neighbourhood averaging and least squares simulations show significant differences between the methods for all the features tested. The simplest simulation was the neighbourhood averaging method. For all five types of features, its mean RMSE value rapidly levels off and the remains constant as the number of images increases. The variation in RMSE values steadily decreases as the number of images increases. The scale of the RMSE values change depending on the feature type, ranging form 12% of AAV for vug features up to 25% for rudists and fracture features.

The least squares method is more complex but also more mathematically rigorous since it accounts for variance in each transition probability. Across all the features its mean RMSE values tend to start at similar values to those from the neighbourhood method, but then they rise as the number of slices increases. The range of RMSE values is normally larger than for similar neighbourhood comparisons. The range also falls off far less rapidly as the number of images increases. The scale of the RMSE values is significantly larger than the neighbourhood RMSE values, ranging form 31-46% of AAV. The exception is for fault features when the two methods result in the same scale of error, 20%.

The results show that the neighbourhood averaging approach will produce realisations with transition probabilities with a consistent mean difference from those used in there calculation as the number of training images increases. The variation between realisations is decreased as the number of training images increases. Using the least squares method, the realisations best match the training image statistics when a small number of training images are used. These results can be better than

similar results using the neighbourhood averaging method. However there is a lack of consistency (large variation) between realisation results, a problem that is only slightly reduced by increasing the number of training images.

The relative scale of the RMSE values is an area of concern. The comparison with the absolute average values suggests that the probabilities obtained from the simulation results are considerably different to those from the original images. However the comparison with the AAV values is only a guide to the scale of the RMSE values as both are single value summaries of 16 different probabilities.

7.8.1 Averaging Transition probabilities

The differences observed between the two simulation methods maybe an artefact caused by averaging in the experiment used to compare them. In the experiment (Figure 7.8) increasing numbers of training images were created, from which synthetic FMI was extracted and then transition probabilities calculated. These transition probabilities were then used to calculate a number of realisations equal to the number of training images. For the multiple images, transition probabilities were averaged by summing the number of times each transition event was observed in each image.

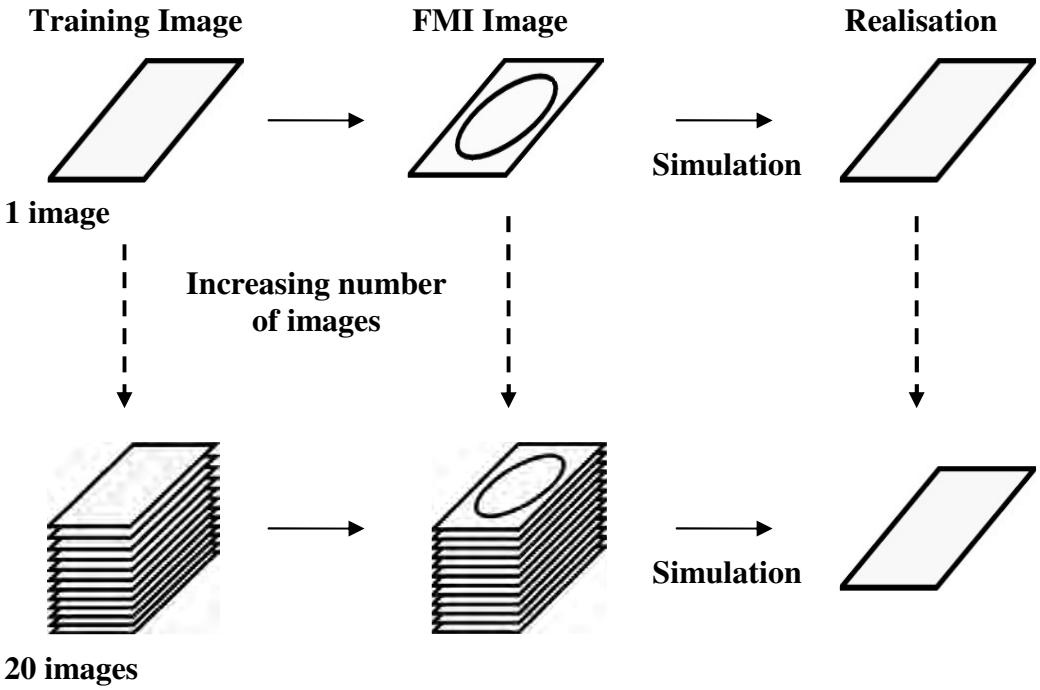

Figure 7.14. Outline of the experiment used to test if the differences observed in the RMSE results are due to the simulation method or the averaging of statistics over a number of slices. An increasing number of slices are used to calculate the transition probabilities but only one realisation is created.

To test if the averaging of the statistics, or the difference in simulation method, was responsible for the differences observed a modified experiment was carried out (Figure 7.14). As before, an increasing number of training images is used to calculated transition probabilities to use in the simulation. These are averaged as before but then used to calculate only a single realisation. Any differences in the comparisons with the realisation will then be attributable to differences in the simulation method and not the post-simulation averaging process. The experiment was carried out using the vug features as these showed a particularly strong difference between the two simulation methods. The maximum number of training images was also increased to check if the rise, observed in Figure 10 (right) using the least squares method, levelled off.

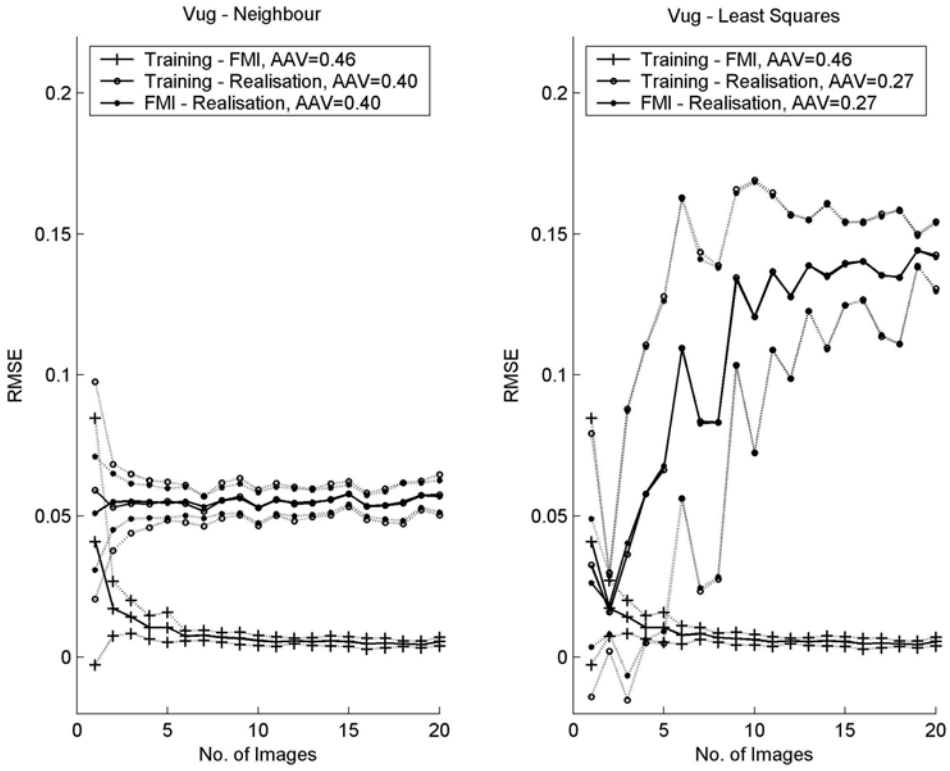

Figure 7.15. The mean RMSE between pairs of transition probabilities calculated from training images, synthetic FMI data, and a single simulated realisation using Vug features. The results using the Neighbourhood averaging method are shown on the left, and the results using the Least Squares method on the right. The dotted lines show +/- 1 standard deviation from the mean RMSE. The legends give the AAV value for each comparison.

The results of the experiment (Figure 7.15) show strong differences still exist between the two simulation methods. As in the multiple realisation experiment (Figure 7.10) the mean RMSE using the neighbourhood averaging method remains consistently around 0.055 (14% of AAV) as the numbers of images increase. The range in RMSE values also drops as the number of images used increases. The mean RMSE values, obtained using the least squares method, are also similar to those from the multiple realisation experiment. They start lower than the neighbourhood values at 0.03 (13% of AAV) but quickly rise before levelling off at 0.13 (48% of AAV) using 20 images.

These results show that the differences observed using the two simulation methods are due to differences in the simulation methods, and are not an artefact introduced by averaging the transition probabilities over a number of images.

7.8.2 Transition probabilities

The results in Figures 7.9-7.13 show that the behaviour of the two simulation methods changes as the number of training images used increases. Therefore the change in the transition probabilities used to create the simulations was investigated.

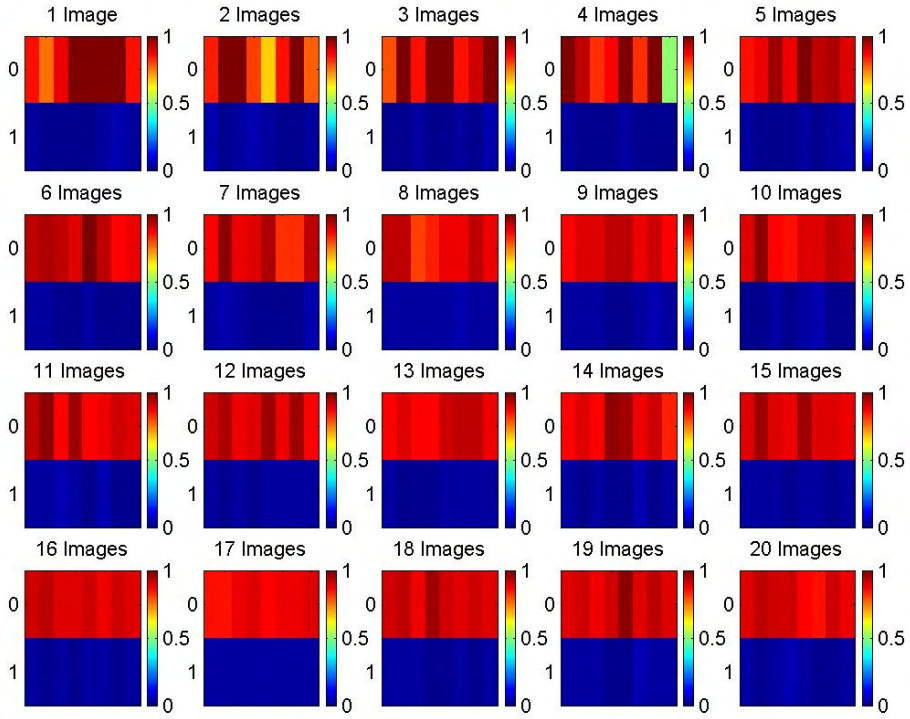

Figure 7.16. An example of the transition probabilities used to create the simulation, illustrating how they change as the number of training images increase. The probabilities shown are for the cell of interest containing a 0. The horizontal axis indicates the position of the transition and the vertical axis indicates the state of the central cell. The colour scheme indicates the size of the transition probabilities.

An example of the change in the transition probabilities used in each simulation is shown in Figure 7.16, using vug features. These are the probabilities calculated from the synthetic FMI data extracted from each training image. The probabilities shown are for the probability of a 0 being in the cell of interest. The horizontal axis

indicates the orientation of the transition, t_i , for i =1 to 8, and the vertical axis gives the state of the central cell, *c*, as either 0 or 1 (see Figure 7.3).

Figure 7.16 shows that when comparing transition probabilities using a small number of training images (e.g. looking along the top row of 5 plots) there are large differences in the probabilities given that the centre cell contains a 0. As the number of training images increases this variability decreases and the probabilities for all the transitions have similar values. The probabilities for the centre cell containing a 1 show little change as the number of training images increase. This is because 1 is the background and dominant cell state in all of the training images.

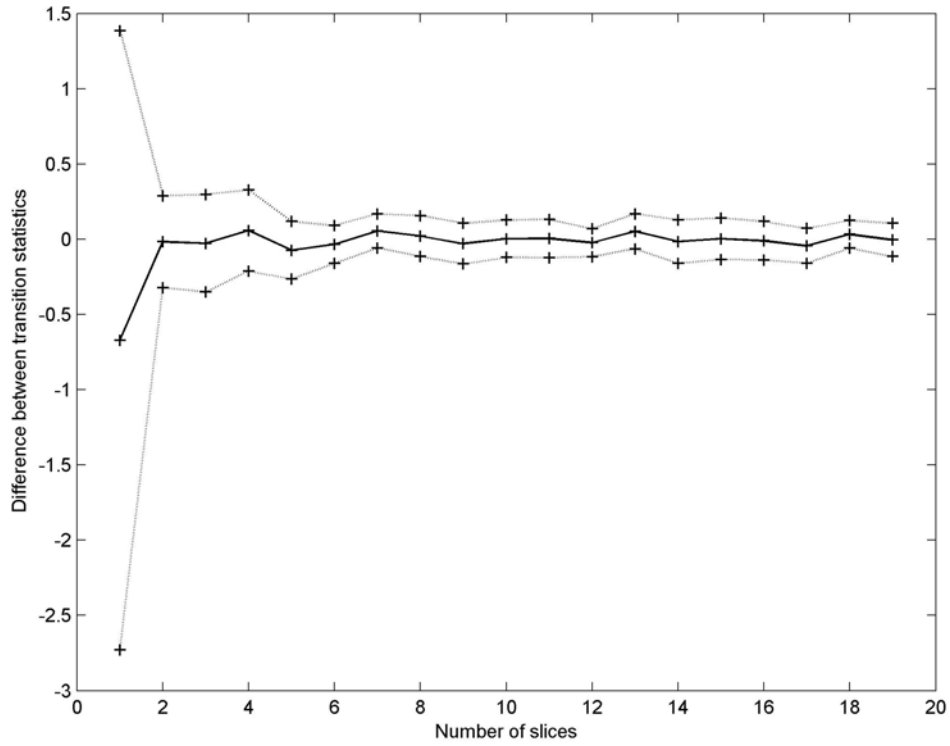

Figure 7.17. The mean difference (solid line) between successive sets of transition probabilities as the number of training images increases. The variation in the difference is shown by +/- 1 one standard deviation (dotted line).

Figure 7.16 shows the results for a single experiment for each increase in the number of training images. By repeating the experiment at each step the mean difference in the transition probabilities can be calculated (Figure 7.17): the mean difference was

calculated by subtracting the transition probabilities for *n*+1 training images from those using *n* training images. The results confirm that the transition probabilities are very variable using a limited number of training images but quickly becomes more consistent as the number increases.

The change in transition probabilities can be used to explain the differences observed between the two simulation methods. The neighbourhood method calculates combined probabilities by taking the mean value of the relevant transition probabilities. The simulation is then performed using those cells with the most neighbouring cells containing data. The least squares method combines the probabilities using least squares but then ranks the cells to be simulated according to the strength of the probabilities. This in turn leads to different simulation behaviour as shown in Figure 7.18.

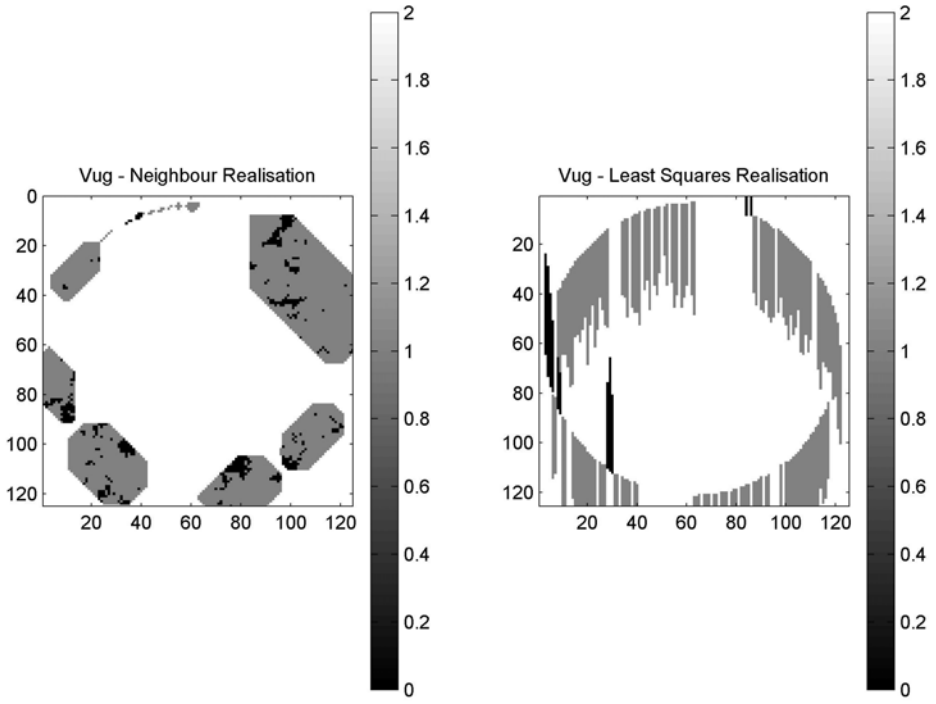

Figure 7.18. Example of how the simulation methods fill in the 2-D area. The simulation uses transition probabilities calculated using 5 training images with vug features. The simulation was run for 4000 cells. The white cells have not been simulated.

Figure 7.18 shows that the neighbourhood averaging method (left) grows steadily out from the given FMI data, with no preferred orientations. The lack of growth on the top section of data is a statistical artefact. There are a number of cells with the same number of neighbours, one of which is picked at random. For this section, in this realisation the simulation has not selected cells in the region as often as in other regions purely by chance. The simulation created using the least squares method (right), however, shows a strong preference for growth in vertical directions. This indicates a strong probability (near 0 or 1) in the transition probabilities in the vertical directions. There is little or no horizontal growth, and little or no variation in the vertical direction.

The neighbourhood averaging simulation seems to follow an intuitively natural growth pattern as it propagates into the space by enlarging the simulation around the existing data. Conversely the least squares method is unnatural as it strictly follows the directions with strong probabilities, often with reference to only a single data cell.

The consistent RMSE results obtained using the neighbourhood averaging simulation method, observed in Figures 7.9-7.13, can be explained by the ranking system it uses. By always selecting the cell with the most neighbouring data points, the combined probabilities used tend towards some average value. The drop in the variation of RMSE values can also be explained by the ranking: as the transition probabilities become more stable the combined statistics will also become more stable.

The behaviour observed using the least squares method can also be explained by the ranking method it utilises. It simulates the cells with the strongest (closest to 0 or 1) combined probabilities. As averaging tends to weaken the combined probability the simulation tends to follow strong probabilities based on a single data cell. This creates the single lines of simulated data, seen in Figure 7.18, that grow into the simulation space. Using a single training image the transition probabilities are quite variable. The least squares method then simulates a limited number of strong probabilities but with a large degree of variability in the results. As the transition probabilities become more similar the method still selects the strongest probability even though this may only be slightly stronger then the rest. This creates a preference for certain directions, which is not contained in the original statistics. This causes the rise in RMSE values with increasing numbers of training images seen in Figures 7.9-7.13.

7.8.3 Actual Simulated Images

The work so far has compared the two methods on their ability to replicate statistics. Perhaps of more concern to the end user is the ability of each method to reproduce realistic and interpretable features.

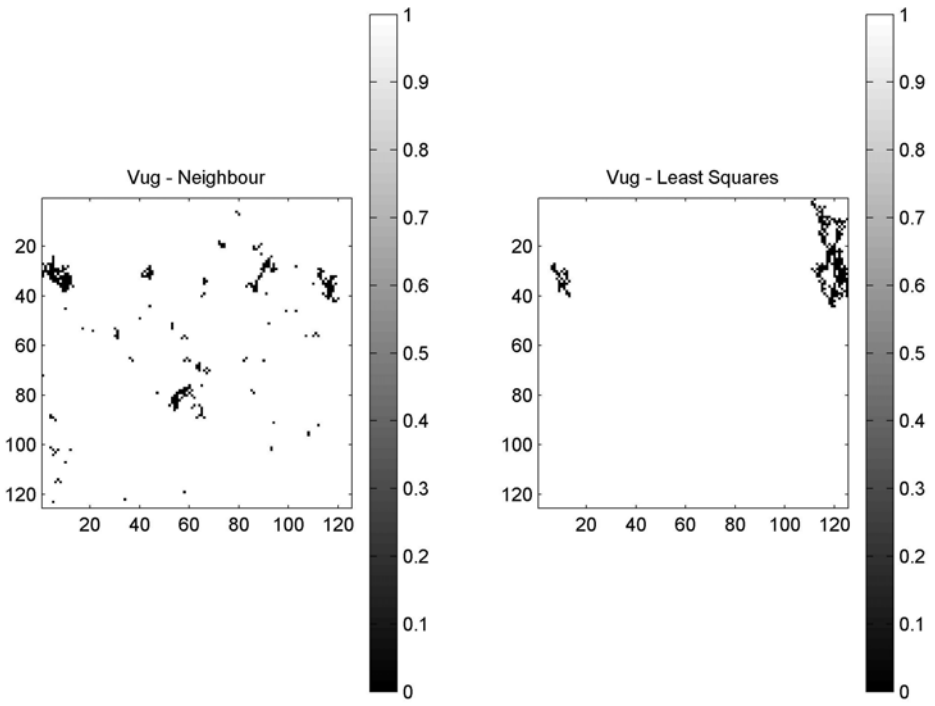

Figure 7.19. An example of the realisations created using both methods. The transition probabilities were calculated using a single training image with vug features.

Figure 7.19 shows an example of the realisations calculated by each simulation method using transition probabilities calculated from a single training image of vug features. The vug features are simple circles. Neither of the two methods has been able to create obvious circular features, though they do show a strong degree of clustering. The neighbourhood realisation (left) contains the greatest range in size and number of clusters, while the least squares realisation has only two clusters.

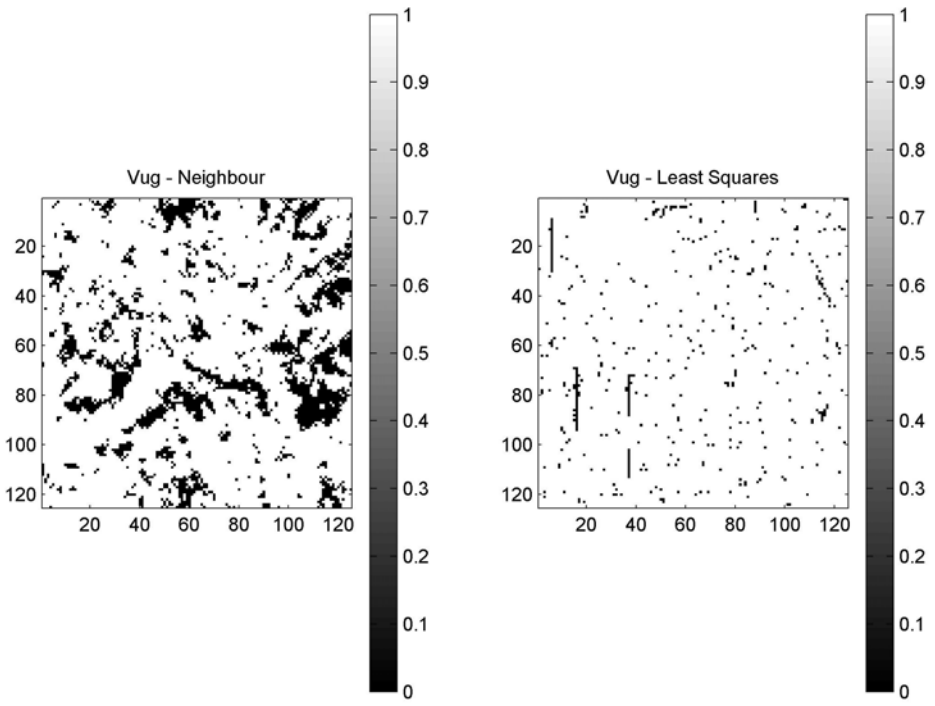

Figure 7.20. An example of the realisations created using both methods. The transition probabilities were calculated using ten training images with vug features.

Figure 7.20 shows the realisations created using transition probabilities calculated from ten training images containing vug features. Again neither shows the perfect circles of the original training images. However the neighbourhood realisation (left) show strong clustering into curved features. As with the realisation created using a single training image there is a degree of noise, in the form of small clusters within the image. The least squares realisation (right) contains very little clustering and all the features created are in the form of vertical lines.

7.8.4 Further Work

The results of the experiments carried out show that the simple neighbourhood averaging method is the best method for the simulation of 2-D planes from FMI data. However it would seem that the problem with the more mathematically rigorous, least squares method lies in the ranking system used. Therefore an interesting experiment would be to create a new simulation method which uses the least squares

method to combine the statistics but then the ranking system used is weighted by the number of neighbouring data cells.

The goal of the simulation method should be the creation of 3-D volumes from FMI data. A crude method would be to create a stack of 2-D slices, but this would lack continuity between the slices. Therefore a truly 3-D approach should be the goal. The method of capturing transition probabilities described in this chapter could easily be extended to 3-D by expanding the template in Figure 7.3. It would become a cube, which would measure the 27 possible two point transitions between the nearest neighbours. These could then be combined, as for the 2-D case, to create the missing multi-point transitions. Potential problems would lie in determining the amount of FMI data required to capture stable transition probabilities and then in validating the realisations produced.

7.9 Conclusion

A method has been proposed for the capture of nearest neighbour, two point transition probabilities from 2-D slices of FMI data, using a 3 by 3 template. Two methods were then described for the combination of these two point probabilities to estimate the unavailable multi point probabilities, and their subsequent simulation. One method involves taking the mean of the individual two point transition probabilities. The simulation is then performed by successively simulating the cell surrounded by the largest number of cells containing data. The second method combines the two point probabilities using a least squares method weighted by the variance of the probability estimates. For this method the cells were ranked according to the strength of the combined probability. The strength of the probability is defined as how close it lies to 0 or 1.

A set of synthetic features were used to compare the two simulation methods. The results show that the neighbourhood simulation method produces realisations with transition probabilities that are stable compared to the training image used in its creation. The least squares method produces realisations with transition probabilities that become increasingly different as the number of training images used in its

creation is increased. The different behaviour in the two simulation methods can be attributed to the different ranking methods they use. Visual inspection of the different realisations shows that the neighbourhood averaging method produces the most realistic simulations. The next step would be to extend the method to 3-D to enable a volume of FMI scale material to be simulated.

Chapter 8 - Discussion

To successfully exploit hydrocarbon reservoirs we require an understanding of the porosity distribution within the reservoir because this controls the storage and flow of fluids. In reservoirs within carbonate formations the porosity distribution is complex due to the heterogeneity of carbonate rocks. Carbonate heterogeneity spans a wide range of length scales and is a product of the biological origins of the formations and their susceptibility to diagenetic change. To understand the distribution of porosity within such formations requires the integration of data gathered using a range of different techniques across the range of length scales at which heterogeneity is observed.

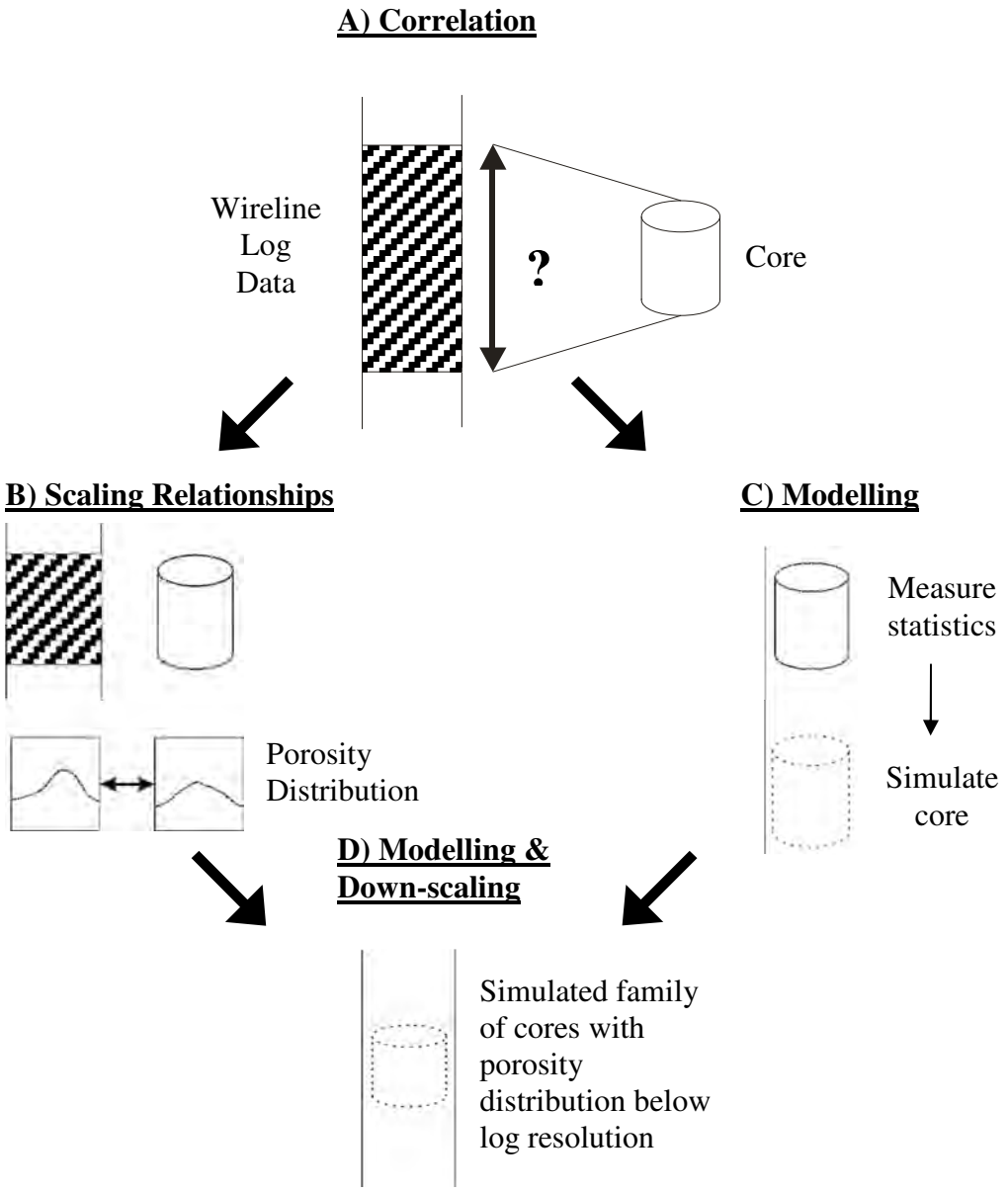

Figure 8.1. Outline of the proposed methodology for the integration of porosity information across a range of scales, from individual pores observed in core samples up to wireline log measurements. A) Core and wireline data sets require to be accurately correlated. Correlation then allows B) the development of porosity scaling relationships and C) the development of modelling techniques. These can then be combined to D) simulate core sections and populate them with down-scaled porosity information.

In this thesis a methodology has been proposed to tackle part of the integration problem: the integration of porosity information from wireline logs with information

from extracted core samples (Figure 8.1). A number of the key problems in the methodology were identified and then investigated; the correlation of data sets, the development of scaling relationships and the creation of virtual core models from wireline logs.

8.1 Correlation

8.1.1 The Correlation Problem

The first step in the data integration process is the accurate positioning, or correlation, of data sets relative to one another. When integrating core and wireline log data the task of correlating the data sets is complicated by differences in when and how they are measured. Core samples are extracted as part of the drilling process, while wireline log measurements are made after drilling has been completed. This results in two different depth measurements which are measured at different times and susceptible to different degrees of uncertainty (e.g. due to the stretching of cables or the sticking of cables). The conventional method for correlating the two data types involves identifying prominent features, such as bed boundaries in both data sets and then interpolating between them. In regions of the borehole without such features this approach can lead to an uncertainty in the correlation in the order of several feet. When integrating wireline data with a much higher resolution, such as FMI data with a resolution of 0.1", then a more accurate correlation is required, particularly if scaling relationships are to be developed between the two data sets.

8.2.1 Statistical Correlation

In this thesis I have proposed and demonstrated a new statistical method to tackle the correlation problem (Chapter 4 & 5). The method correlates data sets based on their statistical properties. Statistics were calculated for a core sample and for overlapping core-length windows of the wireline log data. The core statistic was then compared with that measured in each core length window. The use of individual statistics alone is insufficient to provide a unique correlation, but by combining the results from several statistics in a likelihood function the uncertainty in the correlation can be greatly reduced. Indeed, the method outlined in Chapter 4 enables the uncertainty

in correlation between FMI and CT data to be reduced from 2ft (609mm), using geological marker horizons alone, to 0.72" (18mm) using my new method. While this is not yet at the same resolution as of the FMI data, that is 0.1" (2.54mm), it is a notable improvement on the conventional method.

8.1.3 Limitations

The major limitation on using this method for correlation is that if two regions have the same porosity distribution then discrimination between them is not possible in which case other prior information must be used to resolve the ambiguity. However, if the regions have different distributions, then the correlation maybe further constrained by adding additional statistics to the likelihood function. The addition of further statistics has to be treated carefully as they may result in spurious correlations. The choice of statistics used should therefore always be made using the entropy function, as shown in Chapter 4, to ensure strong correlations are made.

The proposed correlation technique relies on both data sets measuring the same physical property. In Chapters 4 and 5 the FMI and CT data sets used were both converted to spatially variable porosity estimates. In the examples used this was relatively straight forward as the formation from which the data was measured could be considered to be mono-mineralic and composed purely of low-Mg calcite (calcium carbonate). Therefore any differences in the measurements observed could be attributed to changes in porosity alone (the small quantities of pyrite observed in the CT scans (Figures 4.3 and 5.1) were taken as volumetrically insignificant). In different formations, composed of a range of minerals, the conversion to a common property would be more problematic. In particular, the conversion of CT scans would be particularly difficult as they provide a measure of X-ray attenuation for a given volume of material. X-ray attenuation values depend on density, which is a function of both the chemical composition of the material and the degree of porosity in the measurement volume. The two effects would combine and it would be impossible to separate out the porosity component without additional information. A possible solution might be to flood the core sample with a tracer substance with an X-ray attenuation coefficient greatly different from that of the minerals present in the

core. The tracer would reside only in the pore space and be distinguishable from surrounding rock. However, the tracer substance could not be guaranteed to reach all of the porosity particularly if it is particularly small (e.g. microporosity) or isolated from the main pore network.

8.1.4 Applications of the method

In Chapters 4 and 5 a range of statistics were calculated for use in the correlation method. However, the skewness and kurtosis results resolved no correlations between the data sets. This was attributed to the large sampling errors associated with these statistics. Therefore the mean, variance and range statistics were used as they produce good correlations and are simple to calculate. However the method is not restricted to the use of these statistics. Any statistic which can be calculated for both data sets can be used to provide a correlation. To ensure the strength of correlations obtained the chosen statistics should be compared using the entropy process (Chapter 4).

The correlation technique is also not restricted to core and well log data. As the method produces a correlation based on statistical properties it can be applied to any two data sets which measure the same physical property or can be converted to the same measurement type. The method can therefore be applied in a range of contexts wherever data sets are required to be accurately correlated. Possible applications include the provision of correlations at other length scales for the integration of carbonate data, to aid correlations between boreholes or for the identification of features as part of image processing.

8.2 Up-Scaling

8.2.1 The Scaling Problem

Once accurate correlation has been achieved, the next step is to develop scaling relationships between the porosity distributions measured at different length scales. Such scaling relationships would allow data measured at a particular length scale to be converted into measurements which would have been obtained at a different

length scale. These relationships therefore allow data from different measurement techniques with different resolutions to be integrated and compared.

Traditionally scaling relationships have been calculated in the up-scaling direction. That is, if properties are known at one scale, they can be calculated at larger length scales by up-scaling. However, in the methodology outlined in Figure 8.1, the scaling relationships would be used to infer information about the porosity distribution below wireline log resolution through the down-scaling of the wireline log measurements. To date there has been very little work which looks at the down-scaling of data. The only widely used method is through variogram scaling laws developed for the mining industry (Matheron, 1963; Clark, 1979; Frykman and Deutsch, 1999). The variogram scaling laws offer a mechanism for up- and down-scaling measurements through the scaling of variogram parameters.

More generally, up-scaling relationships can be used to down-scale, using inverse theory. In all cases, when down-scaling the result will be a family of detailed porosity distributions (usually infinitely many) which are consistent with the observed up-scaled distribution.

8.2.2 Implementation of Variogram Scaling

In this thesis I am interested in the scaling relationships between core measurements, with resolutions of 0.0064" and 0.0049", and wireline log measurements from an FMI tool, with a resolution of 0.1". As variogram scaling laws offer a mechanism for both up- and down-scaling data I created new computer code which would implement the scaling laws. The code was tested on previously published examples (Frykman and Deutsch, 1999).

Before investigating the down-scaling results, the accuracy of variogram scaling was tested. The testing was carried out by up-scaling variogram parameters measured from the original high resolution CT data and comparing them with variogram parameters measured from CT data averaged to the same resolution as FMI data. The results for the range parameter showed the up-scaled and averaged values to

have similar values, . However, the results for the sill parameter were not in good agreement showing considerable differences between the up-scaled and averaged values, beyond the level of uncertainty. To test if the averaging method applied to the CT was responsible for the mismatch a different method was applied, using a kernel of uniform opposed to Gaussian weights. However, the results showed the two methods produced data with similar variogram parameters.

As the up-scaled range had been shown to be similar to the averaged range it was then compared with the range calculated from core-length windows of FMI data. The up-scaled CT range value was of the same magnitude as the FMI range values but they produced different correlation results from those identified using the statistical correlation technique developed in Chapter 4.

These results show that the variogram scaling technique has failed to up-scale the carbonate data. Given that the code used to implement the technique has been tested successfully and different methods for averaging the CT data produced similar results, then the failure is assumed to be due to some inherent feature of the data. The most likely case is that the data does not conform to the limited statistical model underlying variogram scaling.

8.2.3 Limitations of Variogram Up-Scaling

The use of variogram analysis assumes that the data used is at least second order stationary (mean and variance are the same throughout the data set). On inspection, carbonate data, due to its heterogeneous nature, is not stationary. Therefore, the use of variogram analysis is not valid for carbonate data.

Note that this finding does not call into question the use of the range parameter in the correlation technique (Chapter 4) as it is calculated using the same technique from similarly scaled data. This ensures that even if the use of variograms is unsuitable, then the range values obtained should be comparable between FMI and CT data sets for the same piece of rock.

A possible solution to the problem of non-stationary carbonate data would be to sub-divide the data into regions in which the data is stationary. Variogram analysis could then be carried out within these regions, and those variograms could be scaled using the variogram scaling laws. The sub-division of the data would complicate any method for linking core and wireline data as the different stationary regions would need to be identified in both data sets. Also, if the stationary regions are too small then there will be insufficient data to constrain the calculated variogram making it difficult to estimate variogram parameters.

8.2.4 Other Up-Scaling Methods

The lack of stationarity in the carbonate data lead to the failure to implement the variogram based scaling laws. The lack of stationarity in carbonate data will also affect the application of other scaling methods such as those based on multiple-point statistics or Markov chains. These methods require stationary training images from which to measure the relevant statistics or transitions. Therefore, other scaling methods must be considered if we are to perform the integration of carbonate data from different scales.

8.2.4.1 Up-Scaling Carbonate Porosity Measurements

Porosity is a bulk property of a rock sample: the percentage volume of the sample filled by pore space. In simple monomineralic examples, such as used in this project, the up-scaling could be achieved by taking the arithmetic mean value of a block of measurements. In a more complex sample, with a range of mineral components, it would be difficult to obtain 3D porosity measurements from CT scans due to the difference in X-ray attenuation. If porosity measurements were available then again arithmetic means could be used to provide up-scaled measurements. However, the ultimate goal of this work was to derive down-scaling as well up-scaling relationships. This was why variogram scaling was initially chosen as it provided a mechanism for tackling both aspects of the problem. The use of the arithmetic mean would provide very little information with which to constraint down-scaled measurements.

Another approach that could be considered in future would be to calculate porosity distributions for the data sets at different scales. The statistics of these distributions could then be compared and studied for the presence of scaling behaviour. This would require data which samples the same porosity distribution, but at a range of scales. This could be achieved by taking a succession of increasingly smaller sub-samples from a single core sample and then CT scanning them at increasingly higher resolutions.

8.2.4.2 Up-Scaling Carbonate Permeability Measurements

Another approach could be that instead of focusing on porosity another parameter such as permeability could be scaled. Permeability is not a bulk volume property like porosity and so is therefore more complex to up-scale. There is a range of permeability up-scaling methods which vary from power averaging to the solution of the fluid flow equation at each location (see section 2.4.2.). None of these methods require stationary data and so could be applied to carbonate data. The methodology of Liu (2002) would be particularly relevant when using carbonate data. Their method divides the sample up into regions separated by boundaries with large permeability changes. A separate up-scaling relationship is then calculated for each region. This allows the major fluid flow barriers to be retained in the up-scaled data.

Though there has been a range of work on up-scaling permeability there has been very little on its down-scaling. None of the methods discussed in Chapter 2.4.2. provide mechanisms for creating or constraining down-scaled measurements. This therefore remains an area in which there is still much research to be carried out.

8.3 Modelling

8.3.1 The Modelling Problem

The length of physical core samples recovered from any borehole is limited due to the expense of its recovery. The expense is incurred because to extract a core sample requires the replacement of the conventional drill bit with a core cutting bit. This requires the extraction of the drill string, several thousand feet in length, from the borehole costing time and therefore money. Compared to core samples, wireline log

data is very cheap to obtain as the entire borehole can be covered in a single pass as the tool is pulled through the borehole. This means that there are large amounts of low resolution wireline log data compared to the high resolution core samples. To aid our understanding of formations it would be useful if core scale information could be inferred from wireline log data in the regions of the borehole without core samples.

Work carried out so far has used borehole image logs to identify specific facies and features (Williams and Pirmez, 1999; Russel et al., 2002; Hughes et al., 2003). However borehole image logs can only provide a 2-D image. If the aim is to investigate porosity and fluid flow this requires 3-D information which we could obtain through the creation of 3-D models simulating statistically likely 3-D cores from only borehole image log information.

8.3.2 Modelling from FMI

The accurate correlation between core and wireline log allows the development of a new modelling technique to aid our understanding of porosity distribution. The aim of the technique is to measure spatial statistics from wireline log data and then use these statistics to create a section of 'virtual' core. This 'virtual' core section is a 3-D volume representing the core section which would have been extracted from that section of the borehole. The 'virtual' core section can then be populated with appropriate porosity down-scaled from the wireline log data.

To achieve the simulation two different modelling techniques were developed and are described in Chapter 7. The methods take two-point, spatial statistics measured from a single slice of FMI data and combine them to infer the multiple-point statistics which are not actually observed. One technique averages the two-point statistics from surrounding data while the other combines them using least squares, weighted by variance. The multi-point point statistics are then used to simulate a 2-D slice at FMI resolution. The techniques were compared using synthetic data examples of simple geological features (e.g. faults, vugs etc). The best results were obtained using the method which averaged the two-point statistics.

The techniques developed in this thesis build on the approach of Wu et al (2004). In their work they use 2-D training images to capture transition statistics and then use them to create separate 2-D simulations. However, the techniques developed in this thesis measure two-point transition statistics from a 1-D ring of FMI data and then combine these to estimate the unseen multiple-point transitions. Also the techniques in this thesis create simulations which include the original data, because they use this as a starting point. This results in simulations which can be exactly integrated with measured data.

8.3.3 Limitations

8.3.3.1 Binary Data

The modelling techniques have been developed using binary data. This is created by dividing the data into two states, pore and solid. In real data this division is not straightforward due to measurements that are made from rock volumes including both pore and rock. This creates a continuum of values between the end members which represent pure pore and solid values. The appropriate threshold for the segmentation of the data from within the continuum is not clear. A similar problem exists in the field of digital image analysis and methods developed to tackle this could provide a solution (Mardia and Hainsworth, 1988; Oh and Lindquist, 1999).

The use of binary data by the simulation techniques limits the complexity of data that can be captured and then simulated. One solution would be to increase the number of states into which the data is segmented. This would allow different rock types to be separated, or regions with different distributions of sub-resolution porosity to be distinguished. However any increase in the number of states used would lead to a large increase in the number of transition probabilities to be determined. As the transition probabilities are determined by counting the occurrences of data events within a training image, this would also increase the amount of training data required to ensure the statistics were stable. Increasing the size of the training image risks averaging over regions with different structures but even with a large training image not all of the transitions required maybe observed.

8.3.3.2 2-D Simulation

The modelling techniques described in Chapter 7 create 2-D slices of data, but to understand fluid flow within complex heterogeneous pore networks as found in carbonates requires information in 3-D. To achieve this, the 2-D slices could be stacked on top of each other. These would, however, lack any continuity between the slices. A better approach would be to extend the modelling techniques to simulate a true 3-D volume. The extension would involve using a 3×3×3 cube, instead of a 3×3 square. This would capture the two-point transitions, in 3-D, from a given length of FMI. As before these transitions would be combined to infer the multi-point transitions which cannot be directly measured. As with an increase in the number of states, an expansion to 3-D would lead to a large increase in the number of statistics to be determined.

8.3.3.3 Synthetic Features

The modelling techniques have been demonstrated on very simple synthetic features (Figure 7.6). The results have shown that the techniques have only shown some success in replicating these features. Therefore the application of these techniques to real data would be restricted to regions with very simple features, such as fractures. We have shown that capturing the more complex curvelinear features found in carbonate formations is as yet beyond the power of the techniques developed.

8.3.4 Modelling Applications

To date the analysis of borehole image logs has been restricted to 2-D analysis, positioning data in terms of its vertical position and position around the borehole wall. However, the borehole wall is curved, so the images contain 2-D information about the plane perpendicular to the borehole axis as well as 1-D information in the vertical plane. Therefore, in theory the images can be analysed to provide 3-D information. In this thesis I have shown that the 2-D information in the plane perpendicular to the borehole axis can be measured and then used to create simulations of that plane. Though restricted to examples with relatively simple features the work has been successful in demonstrating that information gathered in 1-D can be used to create simulations in 2-D.

The modelling techniques developed in this thesis could be applied to the problem of creating 3-D simulations from 2-D thin sections, as has been attempted by Wu et al (2006). The work carried out to date measures transition probabilities on orthogonal thin-sections and then creates a 3-D simulation not constrained to real data. The key ideas that could be taken from this thesis include the concept of using real data (e.g. from thin sections or borehole image logs) as the starting point of the simulation. This constrains the simulation to transitions which are actually observed in the data and allows the direct integration of the simulation with the original data. Another idea which could be included is the idea that the order in which cells are simulated is determined by how well the cells transition probabilities are known. This would also stop poorly constrained probabilities skewing the simulation.

8.4 Other Issues Tackled

8.4.1 Variogram Fitting

If the use of variogram scaling was applicable to the data sets, it would still be sensitive to the difficult and somewhat subjective task of fitting a variogram model. Variograms calculated from real data are subject to noise which creates a rough curve. Typically these are fitted with a smooth model which has key parameters which capture the main features: nugget, range and sill. The fitting of these models is generally done by eye but this was impractical in this situation with over 80,000 variograms to be fitted. The are a number of automated variogram fitting algorithms (Zhang et al., 1995; Jian et al., 1996) but these are designed for situations in which the short length lags are better constrained than the longer length lags. When calculating variograms using borehole FMI data the opposite is true and a new method was required. Therefore a new method for fitting variogram models was developed during this thesis (Section 4.4.). The method smoothes the variogram and takes an average of the longer lag values to be the sill. The range is then taken as the first lag at which the variogram reaches the sill value. This approach can produce some erratic changes of values in the more complex variograms and so the method also estimates robust upper and lower bounds on the estimated values.

The method I have developed has a number of areas in which it could be improved. It currently does not fit a nugget value. This was a decision taken because in the vast majority of the variograms visually inspected the nugget parameter would have been negligible. However, to make the method more generally applicable it should provide an estimate of the nugget. Another area for improvement would be in the identification of nested variograms. The more complex variogram shapes can be best modelled through the interaction of several superimposed variogram models. This has not been tackled so far by any of the automated fitting methods but is a prominent feature in variograms calculated from real data.

8.5 Future Work

There are some areas of the proposed methodology outlined in Figure 8.1 which still require investigation. One area is the expansion of the method to larger scales, allowing the integration of seismic data. This could be achieved using effective medium theory (Chapman et al., 2002) which links measured seismic data to physical rock properties. Linking these rock properties to those measured by wireline log data would enable the methodology to provide petrophysical data from individual pores at the micron scale to the kilometre wide reservoir scale.

Another area of future work is to perform fluid flow simulations on the 3-D virtual core simulations. This could be carried out using the established Lattice-Boltzmann methods as in Wu et al (2006). As each simulation represents a single realisation that honours the transition probabilities, fluid flow results from a large number of simulations would be required to estimate the range of fluid flow properties. If the simulations are to be used in fluid flow simulations then this would have impact on how the initial wireline data is segmented, with the further requirement of distinguishing between regions with different porosity and permeability measurements.

Chapter 9 - Conclusions

The main aims of this thesis were:

1. Develop a method for the accurate correlation between core and log data.
2. Use variogram scaling laws to relate variograms calculated from core data to those from borehole log data.
3. Develop a method for simulating a 3-D volume from 2-D log measurements.
4. Integrate aims 2 and 3 to create simulations of 3-D rock at small (core) scale from data at log scale.

The conclusions of this thesis are:

1. A novel method was developed using a cascade of statistics to correlate core and wireline log data. This new method uses a range of statistics, calculated in both data sets. The results for each individual statistic are compared using a likelihood function. The likelihood functions are then combined to produce an accurate correlation. The order in which the statistics are combined is determined using the entropy of the likelihood functions. It was found that the new method improved the accuracy of the core and wireline log correlation, bringing it to within 0.72", compared to 2ft using the existing method.

2. The standard variogram scaling laws were applied to variograms calculated from CT data. The up-scaled variograms were then compared with variograms calculated from averaged CT data. The comparison revealed a mismatch in the sill values between the two sets of variograms. The mismatch was still observed when different averaging methods were used. The mismatch has therefore been attributed to the non-stationary nature of the data. The observation that carbonate data is non-stationary is important as it rules out the use of variogram analysis, or any method using training images, to analyse carbonate data.

3. The basis of a modelling method was developed showing that a 1-D ring of data can be used to capture sufficient spatial statistics to simulate a 2-D plane. Two methods were developed using a 1-D ring of binary FMI data. Both methods use the

ring of data to build up a set of transition probabilities for the two point transitions between adjacent cells. The methods then simulate a 2-D plane using a ring of FMI data as a starting point. The methods use different methods to combine the transition probabilities and determine the order in which the cells are simulated. One method takes an average of the transition probabilities and simulates the cells with the most neighbouring cells containing data. The other method combines them using a least squares approach and then the cells are simulated according to the strength of the combined transition probability. The methods were applied to a range of different synthetic data. The testing revealed that the simpler neighbourhood averaging method produced the best results. This work has the potential to be extended to enable the 3-D simulations required to be calculated from 2-D borehole data.

4. This aim was not achieved during the course of this thesis. However, the work carried out has provided a basis for future work in which 3-D core simulations could be created and populated with sown-scaled porosity information from borehole image logs.

Chapter 10 - References

Alexander, J., 1993, A discussion on the use of analogues for reservoir geology, *in* Ashton, M., ed., Advances in Reservoir Geology, Volume 69: London, Geological Society Special Publications, p. 175-194.

Algeo, T.J., and Wilkinson, B.H., 1988, Periodicity of Phanerozoic Sedimentary Cycles and the Role of Milankovitch Orbital Modulation: Journal of Geology, v. 88, p. 313-322.

Alsharhan, A.S., 1987, Geology and Reservoir Characteristics of Carbonate Buildup in Giant Bu Hasa Oil Field, Abu Dhabi, United Arab Emirates: The American Association of Petroleum Geologists Bulletin, v. 71, p. 1304-1318.

Anselmetti, F.S., Luthi, S., and Eberli, G.P., 1998, Quantitative Characterization of Carbonate Pore Systems by Digital Image Analysis.: The American Association of Petroleum Geologists Bulletin, v. 82, p. 1815-1836.

Armstrong, M., 1998, Basic Linear Geostatistics, Springer, 153 p.

Arns, C.H., Bauget, F., Limaye, A., Sakellariou, A., Senden, T.J., Sheppard, A.P., Sok, R.M., Pinczewski, W.V., Bakke, S., Berge, L.I., Oren, P.E., and Knackstedt, M.A., 2005a, Pore scale characterisation of carbonates using micro X-ray CT: Society of Petroleum Engineers Journal.

—, 2005b, Pore-Scale Characterization of Carbonates Using X-Ray Microtomography: SPE Journal, v. 10, p. 475-484.

Arns, C.H., Knackstedt, M.A., Pinczerwski, W.V., and Garboczi, E.J., 2002, Computation of Linear Elastic Properties from Microtomographic Images: Methodology and Agreement Between Theory and Experiment: Geophysics, v. 67, p. 1396-1405.

Arns, C.H., Knackstedt, M.A., Pinczewski, W.V., and Lindquist, W.B., 2001, Accurate Estimation of Transport Properties from Microtomographic Images: Geophysical Research Letters, v. 28, p. 3361-3364.

Arns, J., Arns, C.H., Sheppard, A.P., Sok, R.M., Knackstedt, M.A., and Pinczerwski, W.V., 2003, Relative Permeability from Tomographic Images: Effect of Correlated Heterogeneity: Journal of Petroleum Science and Engineering, v. 39, p. 247-259.

Bathurst, R.G.C., 1975, Carbonate Sediments and their Diagenesis: Amsterdam, Elsevier, 658 p.

Berger, J.O., 1980, Statistical Decision Theory: New York, Springer-Verlag, 425 p.

Bice, D., 1988, Synthetic stratigraphy of carbonate platform and basin systems: Geology, v. 16, p. 703-706.

Bitzer, K., and Salas, R., 2002, SIMSAFADIM: three-dimensional simulation of stratigraphic architecture and facies distribution modeling of carbonate sediments: Computers and Geoscience, v. 28, p. 1177-1192.

Blunt, M.J., Jackson, M.D., Piri, M., and Valatne, P., 2002, Detailed physics, predictive capabilities and macroscopic consequences for pore-network models of multiphase flow: Advances in Water Resources, v. 25, p. 1069-1089.

Borgomano, J., Masse, J.-P., and Al-Maskiry, S., 2002, The Lower Aptian Shuaiba Carbonate Outcrops in Jebel Akhdar, Northern Oman: Impact on static Modeling for Shuaiba Petroleum Reservoirs: AAPG Bulletin, v. 86, p. 1513-1529.

Bosence, D., and Waltham, D., 1990, Computer modeling the internal architecture of carbonate platforms: Geology, v. 18, p. 26-30.

Bosscher, H., and Schlager, W., 1992, Computer simulation of reef growth: Sedimentology, v. 39, p. 503-512.

Boyles, J.M., Scot, A.J., and Rine, J.M., 1986, A logging form for graphic descriptions of core and outcrop: Journal of Sedimentary Research, v. 56, p. 567-568.

Bryant, I., Carr, D., Cirilli, P., Drinkwater, N., McCormick, D., Tilke, P., and Thurmond, J., 2000, Use of 3D digital analogues as templates in reservoir modelling: Petroleum Geoscience, v. 6, p. 195-201.

Buchem, F.S.P.v., Pittet, B., Hillgartner, H., Grotsch, J., Mansouri, A.I.A., Billling, I.M., Droste, H.H.J., Oterdoom, W.H., and Steenwinkel, M.v., 2002, High-resolution Sequence Stratigraphic Architecture of Barremian/Aptian Carbonate Systems in Northern Oman and the United Arab Emirates (Kharaib and Shu'aiba Formations): GeoArabia, v. 7, p. 461-500.

Budd, D.A., 1989, Micro-rhombic calcite and microporosity in limestones: a geochemical study of the Lower Cretaceous Thamama Group, U.A.E.: Sedimentary Geology, v. 63, p. 293-311.

Bulmer, M.G., 1979, Principles of Statistics, Dover, 250 p.

Burgess, P., 2001, Modeling carbonate sequence development without relative sea-level oscillations: Geology, v. 29, p. 1127-1130.

Caers, J., 2002, Geostatistical history matching under training-image based geological model constraints: SPE 77429, p. 16.

Caers, J., and Zhang, T., 2004, Multiple-point geostatistics: a quantitative vehicle for integrating geologic analogs into multiple reservoir models, *in* Grammer, M.G., Harris, P.M., and Eberlli, G.P., eds., Integration of outcrop and modern analogs in reservoir modelling, Volume 80, AAPG Memoir, p. 394.

Carle, S.F., and Fogg, G.E., 1997, Modelling Spatial Variability with One and Multidimensional Continous-LAg Markov Chains: Mathematical Geology, v. 29, p. 891-918.

Chapman, M., Zatsepin, S.V., and Crampin, S., 2002, Derivation of a Microstructural Poroelastic Model: Geophysical Journal International, v. 151, p. 427-451.

Chen, S.Y., Wang, Z., Shan, X., and Doolen, G.D., 1992, Lattice Boltzmann Computational Fluid Dynamics in Three Dimensions: Journal of Statistical Physics, v. 68, p. 379-400.

Choquette, P.W., and James, N.P., 1986, Diagenesis in Limestones - 3 The deep burial environment: Geoscience Canada, v. 14, p. 3-35.

Choquette, P.W., and Pray, L.C., 1970, Geological Nomenclature and Classification of Porosity in Sedimentary Carbonates: The American Association of Petroleum Geologists Bulletin, v. 54, p. 207-250.

Clark, I., 1979, Practical Geostatistics, Applied Science Publishers Ltd, 129 p.

Curran, P.J., and Atkinson, P.M., 1998, Geostatistics and remote sensing: Progress in Physical Geography, v. 22, p. 61-78.

Curry, T.S., Dowdey, J.E., and Murry, R.C., 1990, Christensen's Physics of Diagnostic Radiology: London, Lea and Febiger, 522 p.

Davis, G.H., and Reynolds, S.J., 1996, Structural Geology of Rocks and Regions, John Wiley and Sons, 776 p.

Davis, J.C., 2002, Statistics and Data Analysis in Geology, John Wiley & Sons, 638 p.

Delhomme, J.P., Bedford, J., Colley, N.M., and Kennedy, M.C., 1996, Permeability and Porosity Upscaling in the Near-Wellbore Domain: The Contribution of Borehole Electrical Images: SPE 36822, p. 89-101.

Doveton, J.H., 1971, An Application of Markov Chain Analysis to the Ayrshire Coal Measures Succession: Scottish Journal of Geology, v. 7, p. 11-27.

—, 1994, Geological Log Analysis using Computer Methods, American Association of Petroleum Geologists.

Duliu, O.G., 1999, Computer axial tomography in geosciences: an overview: Earth Science Reviews, v. 48, p. 265-281.

Dunham, R.J., 1962, Classification of Carbonate Rocks According to Depositional Texture, *in* Ham, W.E., ed., Classification of Carbonate Rocks, Volume 1, Memoirs of American Association of Petroleum Geologists, p. 108-121.

Elfeki, A., and Dekking, M., 2001, A Markov Chain Model for Subsurface Characterization: Theory and Applications: Mathematical Geology, v. 33, p. 569-589.

Emery, D., 1996a, Carbonate Systems, *in* Emery, D., and Myers, K.J., eds., Sequence Stratigraphy: Oxford, Blackwell Science Ltd, p. 297.

—, 1996b, Historical Perspectives, *in* Emery, D., and Myers, K.J., eds., Sequence Stratigraphy: Oxford, Blackwell Science Ltd, p. 3-7.

Evans, A.M., 1993, Ore Geology and Industrial Minerals: Oxford, Blackwell Scientific Publications, 389 p.

Fang, J.H., Chen, H.C., Shultz, A.W., and Mahmoud, W., 1992, Computer-Aided Well Log Correlation: AAPG Bulletin, v. 76, p. 307-317.

Farmer, C.L., 1992, Numerical Rocks, *in* King, P.R., ed., The Mathematics of Oil Recovery, Oxford University Press, p. 437-447.

Fisz, M., 1963, Probability Theory and Mathematical Statistics, John Wiley & Sons, 677 p.

Folk, R.L., 1959, Practical petrographic classification of Limestones: Bulletin of American Association of Petroleum Geologists, v. 43, p. 1-38.

Frykman, P., and Deutsch, C.V., 1999, Geostatistical Scaling Laws Applied to Core and Log Data: SPE 56822, p. 12.

Geman, S., and Geman, D., 1984, Stochastic Relaxation, Gibbs Distributions, and the Baysian Restoration of Images: IEEE Transactions on Pattern Analysis and Machine Intelligence, v. PAMI - 6, p. 721-741.

Gingerich, P.D., 1969, Markov analysis of cyclic alluvial sediments: Journal of Sedimentary Petrology, v. 39, p. 330-332.

Glynn, P.W., and d'Croz, L., 1989, Experimental evidence for high temeprature stress as the cause of El Nino coincident coral mortality: Coral Reefs, v. 8, p. 181-191.

Goggin, D.J., Eisenberg, R.A., Grant, C.W., and Harris, P.M., 1993, Stratigraphic controls on permeability and fluid flow patterns in ramp carbonates: An outcrop study of the San Andres formation, New Mexico, USA, *in* Eschard, R., and Doligez, B., eds., Subsurface reservoir characterization from outcrop observations: Paris, Editions Technip, p. 65-95.

Goldhammer, R.K., 1997, Compaction and Decompaction Algorithms for Sedimentary Carbonates: Journal of Sedimentary Research, v. 67, p. 26-35.

Hearst, J.R., 2000, Well Logging for Physical Properties: a handbook for geophysicists, geologists and engineers: Chichester, Wiley, p. 483.

Hill, J., Tetzlaff, D., Curtis, A., and Wood, R., 2008, Modelling shallow marine carbonate depositional systems: Computers & Geosciences, v. submitted.

Hirono, T., Takahashi, M., and Nakashima, S., 2003, Direct Imaging of fluid flow in fault-related rocks by X-ray CT, *in* Mees, F., Swennen, R., van Geet, M., and Jacobs, P., eds., Applicatiions of X-ray Computed Tomography in the Geosciences, Volume 215: London, Geological Society, p. 107-115.

Hoel, P.G., 1962, Introduction to mathematical statistics, Wiley, 427 p.

Hohn, M.E., and Neal, D.W., 1986, Geostatistical Analysis of Gas Potential in Devonian Shales of West Virginia: Computers & Geosciences, v. 12, p. 611-617.

Hughes, G.W., Siddiqui, S., and Sadler, R.K., 2003, Shu'aiba rudist taphonomy using computerised tomography and image logs, Shaybah field, Saudi Arabia: GeoArabia, v. 8, p. 585-596.

Hussner, H., and Roessler, J., 1996, Modelling of reef growth in a 3-dimensional space, *in* Reitner, J., Neuweiler, F., and Gunkel, F., eds., Global and Regional Controls on Biogenic Sedimentation, Volume 2, Gottinger Arb. Geol. Spec, p. 397-404.

James, N.P., 1984, Introduction to Carbonate Facies Models, *in* Walker, R.G., ed., Facies Models, Geoscience Canada, p. 105-107.

James, N.P., and Choquette, P.W., 1983, Diagenesis 6. Limestones - the seafloor diagenetic environment: Geoscience Canada, v. 10, p. 162-179.

—, 1984, Diagenesis 9. Limestones - the meteoric diagenetic environment: Geoscience Canada, v. 11, p. 161-194.

James, N.P., and Kendall, A.C., 1992, Introduction to Carbonate and Evaporite Facies Models, *in* Walker, R.G., and James, N.P., eds., Facies Models: Response to Sea Level Change, Geoscience Canada, p. 265-275.

Jian, X., Olea, R.A., and Yu, Y., 1996, Semivariogram modeling by weighted least squares: Computers & Geosciences, v. 22, p. 387-397.

Journal, A.G., and Huijbregts, C.J., 2003, Mining Geostatistics, The Blackburn Press, 600 p.

Journel, A.G., Deutsch, C.V., and Desbarats, A.J., 1986, Power averaging for block effective permeability: SPE 15128.

Journel, A.G., and Huijbregts, C.J., 2003, Mining Geostatistics, The Blackburn Press, 600 p.

Kendall, C.G.S.C., and Schlager, W., 1981, Carbonates and Relative Changes in Sea Level: Marine Geology, v. 44, p. 181-212.

Ketcham, R.A., and Carlson, W.D., 2001, Acquisition, optimization and interpretation of X-ray computed tomographic imagery: applications to the geosciences: Computers & Geosciences, v. 27, p. 381-400.

King, P.R., 1989, The use of renormalisation for calculating effective permeability: Transport in Porous Media, v. 4, p. 37-58.

Kinsman, D.J.J., 1964, Reef Coral Tolerance of High Temperatures and Salinities: Nature, v. 202, p. 1280-1282.

Kitandis, P.K., 1997, Introduction to Geostatistics: Applications in Hydrogeology, Cambridge University Press, 249 p.

Knackstedt, M.A., Arns, C.H., Limaye, A., Sakellariou, A., Senden, T.J., Sheppard, A.P., Sok, R.M., Pinczerwski, W.V., and Bunn, G.F., 2004, Digital Core Laboratory: Properties of reservoir core derived from 3D images: SPE 87009, p. 14.

Konert, G., Afifi, A.M., Al-Hajri, S.A., and Droste, H., 2001, Paleozoic Stratigraphy and Hydrocarbon Habitat of the Arabian Plate: GeoArabia, v. 6, p. 407=441.

Leeder, M., 1999, Sedimentology and Sedimentary Basins: Oxford, Blackwell Science Ltd, 592 p.

Li, W., Zhang, C., Burt, J.E., Zhu, A.X., and Feyen, J., 2004, Two-dimensional Markov chain simulation of soil type spatial distribution: Soil Society of America Journal, v. 68, p. 1479-1490.

Lindquist, W.B., Venkatarangan, A., Dunsmuir, J., and Wong, T., 2000, Pore and Throat Size Distributions Measured from Synchrotron X-ray Tomographic Images of Fontainebleau Sandstones: Journal of Geophysical Research, v. 105, p. 21509-21527.

Liu, K., Paterson, L., Wong, P.M., and Qi, D., 2002, A Sedimentalogical Approach to Upscaling: Transport in Porous Media, v. 46, p. 285-310.

Lofts, J.C., and Bristow, J.F., 1998, Aspects of core-log integration: an approach using high resolution images, *in* Harvey, P.K., and Lovell, M.A., eds., Core-Log Integration, Volume 136: London, Geological Society, p. 273-283.

Longman, M.W., 1980, Carbonate Diagenetic Textures from Nearsurface Diagenetic Environments: AAPG Bulletin, v. 64, p. 461-487.

Lonoy, A., 2006, Making Sense of Carbonate Pore Systems: AAPG Bulletin, v. 90, p. 1381-1405.

Lucia, F.J., 1983, Petrophysical Parameters Estimated from Visual Descriptions of Carbonate Rocks: A Field Classification of Carbonate Pore Space.: Journal of Petroleum Technology, v. 216, p. 221-224.

—, 1995, Rock-Fabric/Petrophysical Classification of Carbonate Pore Space for Reservoir Characterization.: AAPG Bulletin, v. 79, p. 1275-1300.

—, 1999, Carbonate Reservoir Characterization, Springer, 226 p.

Mann, C.J., and Dowell, T.P.L., 1978, Quantitaive lithostratigraphic correlation of subsurface sequences: Computers & Geosciences, v. 4, p. 295-306.

Mardia, K.V., and Hainsworth, T.J., 1988, A Spatial Thresholding Method for Image Segmentation: IEEE Transactions on Pattern Analysis and Machine Intelligence, v. 10, p. 919-927.

Marsily, G., 1986, Quantitative Hydrology: San Diego, Academic Press.

Matheron, G., 1963, Principles of Geostatistics: Economic Geology, v. 58, p. 1246-1266.

MathWorks, T., 2002, Matlab, Mathworks.

Maupin, M.P., and Barber, N.L., 2005, Estimated Withdrawals from Principal Aquifers in the United States, 2000: U.S. Geological Survey Circular, v. 1279, p. 46.

McCaffrey, K.J.W., Jones, R.R., Holdsworth, R.E., Wilson, R.W., Clegg, P., Imber, J., Holliman, N., and Trinks, I., 2005, Unlocking the spatial dimension: digital technologies and the future of geoscience fieldwork: Journal of the Geological Society, v. 162, p. 927-938.

Mees, F., Swennen, R., Geet, M.V., and Jacobs, P., 2003, Applications of X-ray Computed Tomography in the Geosciences, Geological Society, p. 243.

Moshier, S.O., 1989, Development of microporosity in a micritic limestone reservoir, Lower Cretaceous, Middle East: Sedimentary Geology, v. 63, p. 217-240.

Mowers, T., and Budd, D.A., 1996, Quantification of Porosity and Permeability Reduscton Due to Calcite Cementation Using Computer-Assisted Petrographic Image Analysis Techniques: AAPG Bulletin, v. 80, p. 309-322.

Oh, W., and Lindquist, W.B., 1999, Image Thresholding by Indicator Kriging: IEEE Transactions on Pattern Analysis and Machine Intelligence, v. 21, p. 590-602.

Okabe, H., and Blunt, M.J., 2004, Prediction of Permeability for Porous Media Reconstructed using Multiple-point Statistics: Physical Review E, v. 70.

—, 2005, Pore space reconstruction using multiple-point statistics: Journal of Petroleum Science and Engineering, v. 46, p. 121-137.

Olea, R.A., 2004, CORRELATOR 5.2-a program for intractive lithostratigraphic correlation of wireline logs: Computers & Geosciences, v. 30, p. 561-567.

Philippe, B., Saad, Y., and Stewart, W.J., 1992, Numerical Methods in Markov Chain Modelling: Operations Research, v. 40, p. 1156-1179.

Pickup, G.E., and Hern, C.Y., 2002, The development of appropriate upscaling procedures: Transport in Porous Media, v. 46, p. 119-138.

Pickup, G.E., Ringrose, P.S., Jensen, J.L., and Scorbie, K.S., 1994, Permeability Tensors for Sedimentary Structures: Mathematical Geology, v. 26, p. 227-250.

Pittet, B., Buchem, F.S.v., Hillgartner, H., Razin, P., Grotsch, J., and Droste, H., 2002, Ecological succession, palaeenvironmental change, and depositional sequences of Barremian-Aptian shallow-water carbonates in northern Oman: Sedimentology, v. 49, p. 555-581.

Pomar, L., and Ward, W.C., 1999, Reservoir-Scale Heterogeneity in Depositional Packages and Diagenetic Paterns on a Reef-Rimmed Platform, Upper Miocene, Mallorca, Spain: AAPG Bulletin, v. 83, p. 1759-1773.

Posamentier, H.W., and Allen, G.P., 1999, Siliciclastic Sequence Stratigraphy: Concepts and Applications, SEPM, 210 p.

Prensky, S.E., 1999, Advances in borehole imaging technology and applications, *in* Lovell, M., Williamson, G., and Harvey, P., eds., Borehole Imaging: applications and case histories, Volume 159: London, Geological Society, p. 1-43.

Price, D., Curtis, A., and Wood, R., 2008, Statistical Correlation Between Geophysical Logs and Extracted Core: Geophysics, v. 73, p. 97-106.

Purdy, E.G., 1963, Recent calcium carbonate facies of the Great Bahama Bank. 2. Sedimentary facies: Journal of Geology, v. 71, p. 472-497.

Purser, B.H., 1973, The Persian Gulf. Holocene carbonate sedimentation and diagenesis in a shallow epicontinental sea: New York, Springer-Verlag, p. 471.

Qian, W., and Titterington, D.M., 1991, Multidimensional Markov Chain Models for Image Textures: Journal of the Royal Statistical Society, v. 53, p. 661-674.

Ragland, D.A., 2002, Trends in cementation exponents (m) for carbonate pore systems: Petrophysics, v. 43, p. 434-446.

Ramakrishnan, T.S., Rabaute, A., Fordham, E., Ramamoorthy, R., Herron, H., Matteson, A., Raghuraman, B., Mahdi, A., Akbar, M., and Kuchuk, F., 1998, A Petrophysical and Petrological Study of Carbonate Cores from the Thamama Formation: SPE 49502.

Renard, P., and Marsily, G., 1997, Calculating Equivalent Permeability: a review: Advances in Water Resources, v. 20, p. 253-278.

Rider, M.H., 2002, The Geological Interpretation of Well Logs, Rider-French, 280 p.

Rudman, A.J., and Lankston, R.W., 1973, Stratigraphic correlation of well logs by computer techniques: AAPG Bulletin, v. 57, p. 577-588.

Russel, S.D., Akbar, M., Vissapragda, B., and Walkden, G.M., 2002, Rock types and permeability prediction from dipmeter and images logs: Shuaiba reservoir (Aptian), Abu Dhabi: AAPG Bulletin, v. 86, p. 1709-1732.

Safinya, K.A., Lan, P.l., Villegas, M., and Cheung, P.S., 1991, Improved Formation Imaging with Extended Microelectrical Arrays: SPE 22726, p. 653-664.

Sandberg, P.A., 1975, New interpretations of Great Salt Lake ooids and of ancient nonskeletal carbonate mineralogy: Sedimentology, v. 22, p. 497-537.

—, 1983, An oscillating trend in Phanerozoic non-skeletal carbonate mineralogy: Nature, v. 305, p. 19-22.

Scathro, D.M., Strobel, J.S., Kendall, C.S.C., Wendte, J.C., Biswas, G., Bedzdek, J., and Cannon, R., 1989, Judy Creek: A case study for a two dimensional sediment deposition simulation, *in* Crevello, P.D., Wilson, J.L., Sarg, J.F., and Read, J.F., eds., Controls on Carbonate Platform and Basin Development, Volume 44, SEPM Special Publication, p. 63-76.

Schneidermann, N., and Harris, P.M., 1985, Carbonate Cements, Volume 36: Tulsa, SEPM, p. 379.

Scholle, P.A., and Halley, R.B., 1985, Burial Diagenesis: Out of Sight, Out of Mind, *in* Schneidermann, N., and Harris, P.M., eds., Carbonate Cements, Volume 36: Tulsa, SEPM, p. 303-328.

Scoffin, T.P., 1987, An Introduction to Carbonate Sediments and Rocks: Glasgow, Blackie, 274 p.

Sellers, E., Vervoort, A., and Van Cleynenbreugel, J., 2003, Three-dimensional visualisation of fractures in rock test samples, simulating deep level mining excavations, using X-ray computed tomography, *in* Mees, F., Swennen, R., van Geet, M., and Jacobs, P., eds., Applicatiions of X-ray Computed Tomography in the Geosciences, Volume 215: London, Geological Society, p. 69-80.

Shannon, C.E., 1948, A mathematical theory of communication: Bell System Technical Journal, v. 27, p. 379-423.

Shinn, E.A., 1969, Submarine Lithification of Holocene Carbonate Sediments in the Persian Gulf: Sedimentology, v. 12, p. 109-144.

Shinn, E.A., and Robbin, D.M., 1983, Mechanical and Chemical Compaction in Fine-Grained Shallow-Water Limestones: Journal of Sedimentary Research, v. 53, p. 595-618.

Smith, T.F., and Waterman, M.S., 1980, New stratigraphic correlation techniques: Journal of Geology, v. 88, p. 451-457.

Sneider, R., and Trampert, J., 1999, Inverse Problems in Geophysics, *in* Wirgin, A., ed., Wavefield Inversion: New York, Springer Verlag.

Spencer, R.J., 1989, Computer models of carbonate platform cycles driven by susidence and eustasy: Geology, v. 17, p. 165-168.

Squires, D.F., 1962, Corals at the Mouth of the Rewa River, Viti Levu, Fiji: Nature, v. 195, p. 361-362.

Stanley, S.M., and Hardie, L.A., 1998, Secular oscillations in the carbonate mineralogy of reef-building and sediment producing organisms driven by tectonically forced shifts in seawater chemistry: Palaeogeography, Palaeoclimatology, Palaeoecology, v. 144, p. 3-19.

Strebelle, S., 2002, Conditional Simulation of Complex Geological Structures Using Multiple-Point Statistics: Mathematical Geology, v. 34, p. 1-21.

Strebelle, S., Payrazyan, K., and Caers, J., 2002, Modelling of a deepwater turbidite reservoir conditional to seismic data using multiple-point geostatistics: SPE 77425, p. 10.

Tarantola, A., 1994, Inverse Problem Theory, Elsevier, 613 p.

Tetzlaff, D., and Harbaugh, J.W.l., 1989, Simulating Clastic Sedimentation: New York, Van Nostrand Reinhold, 202 p.

Tilke, P.G., Allen, D., and Gyllensten, A., 2006, Quantitative Analysis of Porosity Heterogeneity: Application of Geostatistics to Borehole Images: Mathematical Geology, v. 38, p. 155-174.

Timur, A., and Toksoz, M.N., 1985, Downhole Geophysical Logging: Annual Review of Earth and Planetary Sciences, v. 13, p. 315-344.

Tucker, M.E., and Wright, V.P., 1990, Carbinate Sedimentology: Oxford, Blackwell Scientific, 482 p.

Vandersteen, K., Busselen, B., Van Den Abeele, K., and Carmeliet, J., 2003, Quantitative characterization of fracture apertures using microfocus computed tomography, *in* Mees, F., Swennen, R., van Geet, M., and Jacobs, P., eds., Applicatiions of X-ray Computed Tomography in the Geosciences, Volume 215: London, Geological Society, p. 61-68.

Vistelius, A.B., 1949, On the question of the Maechanism of the Formation of Strata: Dolk. Akad. Nauk. SSSR, v. 65, p. 191-194.

Wackernagel, H., 1998, Multivariate Geostatistics, Springer, 291 p.

Waltham, D., 1992, Mathematical modelling of sedimentary basin processes: Marine and Petroleum Geology, v. 9, p. 265-273.

Wang, F.P., Jiachun, D., and Kerans, C., 1998, Modelling dolimitized carbonate-ramp reservoirs: A case study of the Semiole San Andres unit - Part !!, Seismic modelling, reservoir geostatistics, and reservoir simulation: Geophysics, v. 63, p. 1876-1884.

Wang, L., 1996, Modeling Complex Reservoir Geometries with Multiple-Point Statistics: Mathematical Geology, v. 28, p. 895-907.

Warrlich, G.M.D., Waltham, D., and Bosence, D., 2002, Quantifying the sequence startigraphy and drowning mechanisms of atolls using a new 3-D forward modelling program (CARBONATE 3D): Basin Research, v. 14, p. 379-400.

Waterman, M.S., and Raymond, R., 1987, The Match Game: New Stratigraphic Correlation Algorithms: Mathematical Geology, v. 19, p. 109-127.

Weissmann, G.S., Carle, S.F., and Fogg, G.E., 1999, Three-dimensional Hydrofacies Modelling based on Soil Surveys and Transition Probability Geostatistics: Water Resources Research, v. 35, p. 1761-1770.

Wen, X.H., and Gomez-Hernandez, J.J., 1996, Upscaling hydraulic conductivities in heterogenous media: An overview: Journal of Hydrology, v. 183.

Wetherill, G.B., 1982, Elementary Statistical Methods, Chapman and Hall, 356 p.

Wijns, C., Boschetti, F., and Moresi, L., 2003, Inverse Modelling in Geology by Interactive Evolutionary Computation: Journal of Structural Geology, v. 25, p. 1615-1621.

Williams, T., and Pirmez, C., 1999, FMS Images from carbonates of the Bahama Bank Slope, ODP Leg 166: Lithological identification and cyclo-stratigraphy, *in* Lovell, M., Williamson, G., and Harvey, P., eds., Borehole Imaging: Applications and Case Histories, Volume 159: London, Geological Society, p. 227-238.

Wilson, J.L., 1974, Characteristics of Carbonate Platform Margins: AAPG Bulletin, v. 58, p. 810-824.

—, 1975, Carbonate Facies in Geological History: New York, Springer-Verlag, 471 p.

Worden, R.H., and Burley, S.D., 2003, Sandstone Diagenesis: The evolution of sand to stone., *in* Burley, S.D., and Worden, R.H., eds., Sandstone Diagenesis: Recent and ancient, Blackwell Publishing Ltd, p. 3-43.

Wright, V.P., and Tucker, M.E., 1991, Calcretes: Oxford, Blackwell Scientific.

Wu, K., Nunan, N., Crawford, J.W., Young, I.M., and Ritz, K., 2004, An Efficient Markov Chain Model for the Simulation of Heterogenous Soil Structure.

Wu, K., Van Dijke, M.I.J., Couples, G.D., Jiang, Z., Ma, J., Sorbie, K.S., Crawford, J., Young, I., and Zhang, X., 2006, 3D Stochastic Modelling of Heterogenous Porous Media - Applications to Reservoir Rocks: Transport in Porous Media, v. 65, p. 443-467.

Yao, T., and Journal, A.G., 2000, Integrating seismic attribute maps and well logs for porosity modeling in a west Texas carbonate reservoir: addressing the scale and precision problem: Journal of Petroleum Science and Engineering, v. 28, p. 65-79.

Zhang, X.F., Eijkeren, J.C.H.V., and Heemink, A.W., 1995, Short Note on the Weighted Least-Squares Method for Fitting a Semivariogram Model: Computers & Geosciences, v. 21, p. 605-608.